

STATUS OF THESIS

Title of thesis

DETECTION OF GRANULATION TISSUE FOR HEALING
ASSESSMENT OF CHRONIC ULCERS

I LEENA ARSHAD MOHAMMED AHMED

hereby allow my thesis to be placed at the Information Resource Center (IRC) of Universiti Teknologi PETRONAS (UTP) with the following conditions:

1. The thesis becomes the property of UTP
2. The IRC of UTP may make copies of the thesis for academic purposes only.
3. This thesis is classified as

☐ Confidential

☒ Non-confidential

If this thesis is confidential, please state the reason:

The contents of the thesis will remain confidential for _____ years.

Remarks on disclosure:

Endorsed by

Signature of Author

Permanent address: Al-Salafi Unit,
Alaidaroos Street, House No. 23/17,
Crater-Aden, Republic of Yemen

Date: _____

Signature of Supervisor

Name of Supervisor
Prof. Ir. Dr. Ahmad Fadzil
Mohamad Hani

Date: _____

UNIVERSITI TEKNOLOGI PETRONAS

DISSERTATION TITLE: DETECTION OF GRANULATION TISSUE FOR
HEALING ASSESSMENT OF CHRONIC ULCERS

by

LEENA ARSHAD MOHAMMED AHMED

The undersigned certify that they have read, and recommend to the Postgraduate Studies Programme for acceptance this thesis for the fulfilment of the requirements for the degree stated.

Signature:

Main Supervisor:

Prof. Ir. Dr. Ahmad Fadzil Mohamad Hani

Signature:

Co-Supervisor:

Assoc. Prof. Dr. Aamir Saeed Malik

Signature:

Head of Department:

Dr. Rosdiazli bin Ibrahim

Date:

DETECTION OF GRANULATION TISSUE FOR HEALING ASSESSMENT OF
CHRONIC ULCERS

by

LEENA ARSHAD MOHAMMED AHMED

A Thesis

Submitted to the Postgraduate Studies Programme

as a Requirement for the Degree of

MASTER OF SCIENCE

ELECTRICAL AND ELECTRONICS DEPARTMENT

UNIVERSITI TEKNOLOGI PETRONAS

BANDAR SERI ISKANDAR,

PERAK

JANUARY 2013

DECLARATION OF THESIS

Title of thesis

DETECTION OF GRANULATION TISSUE FOR HEALING
ASSESSMENT OF CHRONIC ULCERS

I LEENA ARSHAD MOHAMMED AHMED

hereby declare that the thesis is based on my original work except for quotations and citations which have been duly acknowledged. I also declare that it has not been previously or concurrently submitted for any other degree at UTP or other institutions.

Witnessed by

Signature of Author

Signature of Supervisor

Permanent address: Al-Salafi Unit,
Alaidaroos Street, House No. 23/17,
Crater-Aden, Republic of Yemen

Name of Supervisor
Prof. Ir. Dr. Ahmad Fadzil
Mohamad Hani

Date: _____

Date: _____

DEDICATION

With the deepest love and gratitude, I dedicate this work to my late father and my beloved mother, for their unconditional and endless love and support

ACKNOWLEDGEMENTS

First and foremost, I thank ALLAH almighty for all the grants and blessings he has bestowed on me and for giving me the strength to carry on and complete this research.

I would like to extend my deepest gratitude to my supervisor Prof. Ir. Dr. Ahmad Fadzil M. Hani. His undivided attention to my daily progress, his consistent guidance and support kept me going towards completing my research. I also thank my co-supervisor Dr Aamir Saeed Malik for his guidance and valuable input to the research.

I would like to sincerely thank my colleague Hermawan Nugroho for the valuable discussions that contributed to the development of this research. I also extend my gratitude to Mr Esa Prakasa, Mr Hanung Nugroho and Miss Nejood Eltigani for their support and valuable input whenever I needed it.

My sincere gratitude to Dr Adawiyah Jamil, Dr Felix Yap Boon Bin and staff at Hospital Kuala Lumpur for their effort and assistance in providing the data and the valuable medical knowledge needed for this study.

I would like to thank Universiti Teknologi Petronas and Centre of Graduate Studies for giving me the opportunity to pursue my Masters degree. I sincerely thank respected lecturers and lab technicians who provided me with the equipment and technical support whenever required.

My most gratitude is extended to Sameha Alshakhsi, Atieh Ranjbar, Hamada Alabsi, Abdullah Almuhairi, Gehan Alsalat, Mojdeh Rastgoo, Ambreen Shafeeq, Sima S. Alian and Tajrul Shaheer, whose friendships will always be valuable to me, for their consistent and sincere support. Last but certainly not the least; I would like to thank my beloved mother, family members and friends for their love, trust and endless support that always steered me to aim higher in my life.

ABSTRACT

Wounds that fail to heal within an expected period develop into ulcers that cause severe pain and expose patients to limb amputation. Ulcer appearance changes gradually as ulcer tissues evolve throughout the healing process. Dermatologists assess the progression of ulcer healing based on visual inspection of ulcer tissues, which is inconsistent and subjective. The ability to measure objectively early stages of ulcer healing is important to improve clinical decisions and enhance the effectiveness of the treatment. Ulcer healing is indicated by the growth of granulation tissue that contains pigment haemoglobin that causes the red colour of the tissue. An approach based on utilising haemoglobin content as an image marker to detect regions of granulation tissue on ulcers surface using colour images of chronic ulcers is investigated in this study. The approach is utilised to develop a system that is able to detect regions of granulation tissue on ulcers surface using colour images of chronic ulcers. The system first employs data transformation using independent component analysis to extract grey-level images that show the distribution of haemoglobin on ulcer surface reflecting identified regions of granulation tissue. Clustering-based segmentation using fuzzy c-means techniques is then applied to segment the identified regions of granulation tissue on extracted haemoglobin images. Ulcer tissues reference images are developed to investigate the performance of the developed system. Results indicate the system's ability to detect clearly granulation tissue regions in ulcer images corrupted with white noise corresponding to Signal-to-Noise Ratio (SNR) levels of more than 12dB with more than 96.0% sensitivity, 99.6% specificity and 99.5% accuracy. The performance degrades gradually for images with SNR levels of less than 12dB due to increased effect of noise. The system is applied on real ulcer images and output is compared with dermatologists' assessment. A high correlation value of 0.961 is obtained which indicates a strong similarity between system detection and dermatologists' assessment of granulation tissue. Furthermore,

the system is able to identify granulation tissue regions that cannot be discerned visually at early stages of ulcer healing. It is hoped that this work contributes to the development of a new objective and non-invasive scheme to assess the healing progression of chronic ulcers in a more precise and reliable way.

ABSTRAK

Luka-luka yang gagal untuk sembuh dalam tempoh masa yang dijangka akan berkembang menjadi ulser yang menyebabkan kesakitan yang teruk dan mendedahkan pesakit untuk pembedahan anggota. Penampilan ulser berubah secara beransur-ansur kerana tisu ulser berkembang sepanjang proses penyembuhan. Ahli dermatologi menilai perkembangan penyembuhan ulser berdasarkan pemeriksaan visual tisu ulser yang tidak konsisten dan subjektif. Keupayaan untuk mengukur secara objektif peringkat penyembuhan ulser adalah penting untuk meningkatkan keputusan klinikal dan meningkatkan keberkesanan rawatan. Penyembuhan ulser ditunjukkan oleh pertumbuhan tisu granulasi yang mengandungi pigmen hemoglobin yang menyebabkan warna tisu menjadi merah tisu. Satu pendekatan berdasarkan penggunaan kandungan hemoglobin sebagai petanda imej untuk mengesan kawasan-kawasan tisu granulasi pada permukaan ulser berdasarkan imej warna ulser kronik disiasat dalam kajian ini. Pendekatan ini digunakan untuk membangunkan satu sistem yang dapat mengesan tisu granulasi pada permukaan ulser berdasarkan imej warna ulser kronik. Sistem ini akan menggunakan transformasi data berdasarkan analisis komponen bebas untuk mengekstrak tahap kelabu imej yang menunjukkan taburan hemoglobin pada permukaan ulser. Segmentasi berasaskan kelompok menggunakan teknik '*fuzzy c-means*' dan diaplikasikan di kawasan yang dikenal pasti tisu granulasi dalam imej-imej hemoglobin yang diekstrak. Imej tisu ulser rujukan dibangunkan untuk menyiasat prestasi sistem. Keputusan menunjukkan keupayaan sistem dengan jelas dapat mengesan kawasan-kawasan tisu granulasi dalam imej ulser yang rosak dengan hingar putih sepadan dengan 'Signal-to-Noise Ratio' (SNR) tahap lebih daripada 12dB dengan lebih daripada sensitiviti sebanyak 96.0%, spesifikasi sebanyak 99.6% dan ketepatan sebanyak 99.5%. Prestasi semakin menurun untuk imej tahap SNR kurang daripada 12dB disebabkan oleh kesan peningkatan hingar. Sistem yang digunakan pada imej-imej ulser yang sebenar dan keputusannya dibanding dengan penilaian ahli dermatologi. Satu nilai korelasi yang tinggi, iaitu 0.961 diperolehi. Ini menunjukkan persamaan yang kuat antara sistem pengesanan ini dan penilaian ahli dermatologi. Tambahan pula, sistem ini mampu mengenal pasti kawasan tisu granulasi yang tidak boleh di lihat secara visual pada peringkat

awal penyembuhan ulser. Dengan penilaian ini, diharapkan bahawa kajian ini dapat menyumbang kepada pembangunan objektif yang baru dan memperkenalkan pemeriksaan ulser yang tidak invasif yang dapat menilai perkembangan penyembuhan ulser kronik dengan cara yang lebih tepat dan boleh dipercayai.

In compliance with the terms of the Copyright Act 1987 and the IP Policy of the university, the copyright of this thesis has been reassigned by the author to the legal entity of the university,

Institute of Technology PETRONAS Sdn Bhd.

Due acknowledgement shall always be made of the use of any material contained in, or derived from, this thesis.

© Leena Arshad Mohammed Ahmed, 2012

Institute of Technology PETRONAS Sdn Bhd

All rights reserved.

TABLE OF CONTENT

ABSTRACT.....	vii
ABSTRAK.....	ix
LIST OF FIGURES.....	xvi
LIST OF TABLES	xxi
LIST OF ABBREVIATIONS	xxii
CHAPTER 1 INTRODUCTION	1
1.1 Background of Study.....	1
1.2 The Role of Digital Imaging.....	3
1.3 Problem Statement	4
1.4 Research Hypothesis and Implemented Approach	6
1.5 Research Objective.....	8
1.6 Scope of Work	9
1.7 An Overview of the Thesis Structure.....	9
CHAPTER 2 WOUND CARE AND ANALYSIS	11
2.1 Introduction.....	11
2.2 Chronic Wounds and Ulcers	12
2.3 Prevalence and Economic Impact of Chronic Wounds.....	12
2.4 Wound Healing Process.....	13
2.4.1 Haemostasis	14
2.4.2 Inflammation.....	14
2.4.3 Proliferation	14
2.4.4 Maturation.....	15
2.5 Chronic Leg Ulcers	15
2.5.1 Vascular Ulcers	16
2.5.2 Pressure Ulcers.....	17
2.5.3 Diabetic Ulcers.....	18
2.6 Ulcer Care and Management	19
2.7 Chronic Ulcers Assessment and Documentation.....	19
2.7.1 Ulcer Assessment Parameters	20
2.7.2 Physical Appearance of the Ulcer Surface	21

2.8 Ulcer Tissues Assessment in Clinical Practice.....	24
2.9 Ulcer Tissue Assessment using Digital Imaging.....	26
2.9.1 Information from a Single Colour Channel.....	27
2.9.2 RGB Histogram Distributions	31
2.9.3 Colour and Texture Descriptors	33
2.10 Ulcer Colour and Ulcer Healing	36
2.11 Summary	38
CHAPTER 3 DIGITAL IMAGING AND DATA ANALYSIS TECHNIQUES.....	40
3.1 Introduction	40
3.2 Colour Vision and Formation of Digital Colour Images	40
3.2.1 The Perception of Colours.....	41
3.2.2 Digital Camera and RGB Colour Images.....	43
3.2.3 RGB Colour Model Representation.....	44
3.2.4 Colour Constancy and Colour Shift Correction	45
3.3 Principal Component Analysis	47
3.3.1 Eigenvalues and Eigenvectors	48
3.3.2 Covariance Matrix	48
3.3.3 Standardized Linear Combination	49
3.3.4 Estimation of Principle Components	50
3.4 Independent Component Analysis.....	51
3.4.1 Linear Mixing Model.....	51
3.4.2 Definition of Independence	53
3.5 FastICA	54
3.5.1 Whitening	54
3.5.2 Basic Principle of ICA Estimation in FastICA.....	55
3.5.3 Measures of Non-Gaussianity	56
3.5.4 Approximation of Negentropy	57
3.5.5 Fixed Point Algorithm	57
3.5.6 Estimation of Independent Components	58
3.6 Machine Learning and Clustering-Based Classification.....	59
3.6.1 Clustering	59
3.6.2 Fuzzy C-means Clustering	60

3.7 Threshold-Based Segmentation	62
3.7.1 Otsu's Thresholding Method	62
3.8 Summary.....	65
CHAPTER 4 GRANULATION TISSUE DETECTION SYSTEM FOR CHRONIC	
ULCERS.....	68
4.1 Introduction.....	68
4.2 Flow Chart of Granulation Tissue Detection System.....	68
4.3 Data Collection and Acquisition of Ulcer Images	69
4.3.1 Data Acquisition Settings	70
4.3.2 Data Acquisition Procedure	72
4.4 Pre-processing and Ulcer Dataset Preparation.....	74
4.4.1 Correcting Colour Shifts.....	74
4.4.2 Selecting Regions of Interest (ROIs).....	76
4.5 Data Transformation to Determine Granulation Tissue Regions.....	77
4.5.1 Creating Observation Input Dataset	78
4.5.2 Pre-Processing of Input Dataset.....	79
4.5.3 Detection of Haemoglobin Distribution	80
4.5.4 Post-Processing of Extracted Haemoglobin Images	82
4.6 Clustering-Based Segmentation of Granulation Tissue Regions.....	84
4.6.1 Granulation Region Reference Image	85
4.6.2 Classifying and Segmenting Granulation Tissue Regions.....	87
4.6.3 Selection of Number of Clusters	88
4.7 Ulcer Healing Assessment and Monitoring.....	90
4.7.1 Ulcer Boundary Reference Image.....	91
4.7.2 Granulation Region Area Measurement	94
4.8 Summary.....	96
CHAPTER 5 RESULTS AND ANALYSIS	
5.1 Introduction.....	98
5.2 Performance Analysis of Granulation Tissue Detection Algorithms.....	98
5.2.1 Ulcer Tissue Sample Images.....	99
5.2.2 Ulcer Tissue Image.....	104
5.2.3 Detection of Granulation Tissue Patches.....	106

5.2.4 White Gaussian Noise Models	108
5.2.5 System Performance Measures.....	110
5.2.6 Discussion and Analysis	114
5.3 Detection of Granulation in Ulcer Images	120
5.3.1 Optimum Number of Clusters for Clustering-Based Segmentation.	121
5.3.2 Correlation and Overlap Analysis	124
5.4 Summary	139
CHAPTER 6 CONCLUSION.....	142
6.1 Introduction	142
6.2 An Overall Summary	142
6.3 Contribution and Future Work	146
REFERENCES.....	148
LIST OF PUBLICATIONS	155

LIST OF FIGURES

Figure 1.1: Chronic leg ulcers acquired at Hospital Kuala Lumpur	2
Figure 1.2: Typical healing stages of an ulcer [10]	5
Figure 1.3: Absorption spectra of oxy-haemoglobin and deoxy-haemoglobin [22].....	7
Figure 2.1: Schematic illustration of a deep wound [1]	12
Figure 2.2: Wound healing phases	14
Figure 2.3: Most common locations of leg ulcers [7]	16
Figure 2.4: A chronic venous ulcer [1]	17
Figure 2.5: A chronic arterial ulcer [39]	17
Figure 2.6: A chronic pressure ulcer [42].....	18
Figure 2.7: A chronic diabetic ulcer [1]	18
Figure 2.8: A leg ulcer covered with black necrotic tissue [1].....	21
Figure 2.9: A leg ulcer covered with yellow slough [1].....	22
Figure 2.10: An ulcer covered with granulation tissue [51].....	22
Figure 2.11: An ulcer covered with pink epithelial tissue [47]	23
Figure 2.12: Typical healing stages of an ulcer [10].....	23
Figure 2.13: An ulcer with approximately 25% black, 35% yellow and 40% red [47]	25
Figure 2.14: Wound healing continuum [12]	25
Figure 2.15: Time course of colour index (Icolor) in percentages of green on 16 wound sites [14].....	28
Figure 2.16: FUJI colour scale held near wound [15].....	29
Figure 2.17: Schematic illustration of the CBR approach for tissue classification [18]	32
Figure 2.18: Segmentation results of the three unsupervised techniques used in ESCALE [21].....	35
Figure 2.19: Reflectance Spectrum of the Visible Light.....	37
Figure 2.20: Absorption spectra of oxy-haemoglobin and deoxy-haemoglobin [22]..	37
Figure 3.1: Spectral responsiveness of L, M and S cones [55]	41

Figure 3.2: A schematic diagram of the electromagnetic spectrum indicating the visible light spectrum extending from 400nm-700nm	42
Figure 3.3: Perception of colour.....	42
Figure 3.4: The Bayer filter pattern on the CCD profile	44
Figure 3.5: The RGB colour cube	44
Figure 3.6: Red, Green and Blue grey-level images of a digital colour image.....	45
Figure 3.7: Effects of varying illumination on the perceived colours of objects.....	47
Figure 3.8: Basic model of Independent Component Analysis (ICA) [68].....	53
Figure 3.9: Illustration of cluster centres trajectories in fuzzy c-means clustering applied in a two-dimensional data [76]	62
Figure 3.10: Segmentation using Otsu's thresholding method.....	65
Figure 4.1: Flow chart of granulation tissue detection system	69
Figure 4.2: Digital Single Lens Reflector Camera (Nikon D300) and AF-S DX Nikon 16-85mm f/3.5-5.6G ED VR Lens	70
Figure 4.3: Wound dressing room where most of the images are acquired.....	71
Figure 4.4: Nikon SB-900 flashlight with diffuser dome	71
Figure 4.5: Reference stickers placed near ulcers for colour and size reference	72
Figure 4.6: Flow chart of data acquisition procedure.....	74
Figure 4.7: Flow chart of the colour correction procedure	75
Figure 4.8: Ulcer image corrected using developed colour shifts correction algorithm	76
Figure 4.9: Selection of regions of interest (ROIs) from colour corrected ulcer image	77
Figure 4.10: Flow chart of the developed algorithm to determine regions of haemoglobin distribution from colour ulcer images	78
Figure 4.11: Create observation input dataset from colour ulcer image	79
Figure 4.12: Extracted independent sources from observed colour ulcer image	81
Figure 4.13: Extracted Image Due to Pigment Haemoglobin.....	82
Figure 4.14: Removal of impulse noise from extracted haemoglobin images.....	84
Figure 4.15: Granulation assessment reference image obtained from manual tracing of granulation tissue.....	86
Figure 4.16: Classification of regions in extracted haemoglobin image	87

Figure 4.17: Segmentation of clustered granulation tissue in classified image.....	88
Figure 4.18: Computing the difference between the granulation regions detected using the developed algorithm and the granulation region traced by dermatologists.....	89
Figure 4.19: Skin laceration situated near the ulcer that is wrongly detected as granulation tissue	92
Figure 4.20: Ulcer boundary reference image obtained from manual tracing of the ulcer's boundary.....	93
Figure 4.21: Removing regions outside the ulcer boundary wrongly detected as granulation tissue	93
Figure 4.22: Segmentation of reference patch for area measurements.....	95
Figure 5.1: A schematic diagram illustrating a box plot with detected outliers.....	100
Figure 5.2: Distributions of Red, Green and Blue channels pixels of granulation tissue	102
Figure 5.3: Distributions of Red, Green and Blue channels pixels of slough tissue .	102
Figure 5.4: Distributions of Red, Green and Blue channels pixels of necrotic tissue	102
Figure 5.5: Distributions of Red, Green and Blue channels pixels of skin tissue	102
Figure 5.6: Image patches of size 200x200 pixels of skin, granulation, slough and necrotic tissues.....	104
Figure 5.7: Ulcer tissue image	105
Figure 5.8: Granulation tissue reference binary image	106
Figure 5.9: Extracted haemoglobin image from ulcer tissue image	106
Figure 5.10: Otsu's thresholding based segmentation of haemoglobin image extracted from ulcer tissue image	107
Figure 5.11: Developed ulcer tissue reference image with SNR of 10dB	110
Figure 5.12: Number of granulation pixels detected as non-granulation for all ulcer tissue reference images.....	111
Figure 5.13: Number of non-granulation pixels detected as granulation for all ulcer tissue reference images.....	112
Figure 5.14: Sensitivity, specificity and accuracy of granulation detection system for all ulcer tissue reference images	114
Figure 5.15: Detection of granulation patches in image with SNR of 20 dB.....	114
Figure 5.16: Detection of granulation patches in image with SNR of 17dB.....	115

Figure 5.17: Detection of granulation patches in image with SNR of 16dB	115
Figure 5.18: Detection of granulation patches in image with SNR of 15dB	116
Figure 5.19: Detection of granulation patches in image with SNR of 14dB	116
Figure 5.20: Detection of granulation patches in image with SNR of 12dB	117
Figure 5.21: Detection of granulation patches in image with SNR of 10dB	117
Figure 5.22: Detection of granulation patches in image with SNR of 8dB	118
Figure 5.23: Detection of granulation patches in image with SNR of 6dB	119
Figure 5.24: Detection of granulation patches in image with SNR of 4dB	119
Figure 5.25: A plot of the segmentation difference error obtained from applying the clustering based segmentation on one ulcer image iteratively for k=2 till k=10	121
Figure 5.26: A plot of the segmentation difference error obtained from applying the clustering based segmentation on one ulcer image iteratively for k=2 till k=10	122
Figure 5.27: Minimum segmentation difference error and optimum number of clusters obtained for each ulcer image	122
Figure 5.28: Frequency of optimum cluster number	123
Figure 5.29: Scatter plot of detected granulation tissue using the developed granulation detection system versus the amount of granulation tissue traced by the dermatologists	124
Figure 5.30: Schematic diagram of the overlap between detected and assessed granulation tissue regions (case one).....	126
Figure 5.31: Percentage overlaps between detected and traced granulation tissue...	126
Figure 5.32: Example of granulation tissue detection (case one)	128
Figure 5.33: Schematic diagram of the overlap between detected and assessed granulation tissue regions (case two).....	129
Figure 5.34: Percentage overlaps between detected and traced granulation tissue...	130
Figure 5.35: Example of granulation tissue detection (case two)	131
Figure 5.36: Schematic diagram of the overlap between detected and assessed granulation tissue regions (case three-1)	132
Figure 5.37: Percentage overlaps between detected and traced granulation tissue...	133
Figure 5.38: Example of granulation tissue detection (case three-1)	135
Figure 5.39: Schematic diagram of the overlap between detected and assessed granulation tissue regions (case three-2)	136

Figure 5.40: Percentage overlaps between detected and traced granulation tissue ...	137
Figure 5.41: Example of granulation tissue detection (case three-2).....	138

LIST OF TABLES

Table 5.1: Ulcer tissue sample images and total number of pixels selected.....	101
Table 5.2: Signal to Noise Ratio (SNR) values of ulcer tissue reference images.....	109
Table 5.3 Percentage overlaps between detected and traced granulation tissue.....	127
Table 5.4 Percentage overlaps between detected and traced granulation tissue.....	130
Table 5.5 Percentage overlaps between detected and traced granulation tissue.....	134
Table 5.6 Percentage overlaps between detected and traced granulation tissue.....	137

LIST OF ABBREVIATIONS

2D	2-Dimentional
3D	3-Dimentional
BSS	Blind Source Seperation
CBR	Case-Based Reasoning
CCD	Charge-Coupled Device
CSC	Colour Structure Code
DSLR	Digital Single-Lens Reflector
E-TTL	Evaluative-Through The Lens
FN	False Negative
FP	False Positive
ESCALE	EScarre Analyse Lisibilite' Evaluation
ICA	Independent Component Analysis
IQR	Inter-Quartile Range
KNN	K-Nearest Nieghbor
NMRR	National Medical Research Registry
PCA	Principle Component Analysis
PDF	Probability Density Function
RGB	Red, Green and Blue
RMS	Root Mean Square
ROI	Regions of Interests
SNR	Signal-to-Noise Ratio
SVM	Support Vector Machine
TC	Topical Corticosteroids
TN	True Negative
TP	True Positive
WHC	Wound Healing Continuum

CHAPTER 1

INTRODUCTION

1.1 Background of Study

When the skin is injured due to a certain trauma, it goes through a series of overlapping procedures to repair the damaged tissues. Chronic wounds or ulcers occur when the injured tissues do not follow a normal course of healing within an expected period of time due to untreated underlying aetiologies or improper wound management [1]. Non-healing ulcers could remain for years causing pain and discomfort to patients and expose them to the risk of infection and limb amputation. It is reported that 66% of patients who went through limb amputation in Malaysia between 2003-2005 were suffering from diabetic foot complications [2].

According to recent studies, more than 3.0% of the adult population has the potential to develop chronic wounds during their lifetime with a significantly increased prevalence in the elderly [3]. In Malaysia, the prevalence of chronic foot ulcers in patient with diabetes between 1999 - 2008 was reported as 9.9% with an annual prevalence of 1% [4]. Chronic ulcers introduce not only a major problem in dermatology but an economic dilemma especially in western countries. The annual cost associated with the treatment and care of ulcers was estimated to be around \$5 billion to \$10 billion in the United States and around £400 million in the United Kingdom [3], [5]. The average cost of treating diabetic ulcers was estimated to be more than RM 600 per day in Malaysia in the year of 2006 [6]. The prevalence of chronic wounds may increase significantly due to the increase in the population's age or underlying aetiologies such as diabetes and venous and arterial insufficiencies.

Leg ulcers are common types of chronic wounds that are found on the lower extremity below the knee and mostly affect people above the age of 60. There are three main types of leg ulcers according to the aetiologies that cause them: vascular (venous and arterial), diabetic (neuropathic) and pressure ulcers. Most leg ulcers are either vascular or diabetic and affects 1% of the adult population and 3.6% of people older than 65 years [7]. Figure 1.1 shows examples of two chronic leg ulcers acquired at Hospital Kuala Lumpur, Malaysia.



Figure 1.1: Chronic leg ulcers acquired at Hospital Kuala Lumpur

An accurate and thorough assessment of the ulcer is important to provide baseline information on the ulcer severity status and to determine the appropriate course of treatment [8], [9]. This reflects on the effectiveness of ulcer care and management in terms of time and cost of treatment. There are several ulcer assessment parameters that need to be thoroughly analyzed by clinicians to determine the severity status of the ulcer such as the physical appearance of the ulcer, the condition of the surrounding skin, the odour and pain associated with the ulcer as well the amount and characteristics of the exudates on the ulcer surface. The patients' medical history of previous ulcers and their corresponding treatments are also needed to acquire a full analysis of the ulcer condition.

The physical appearance of the ulcer in particular plays a significant role in determining the ulcer's severity status and monitoring its healing progression. There are four main types of tissues that are present on the ulcer surface: necrotic tissue, slough, granulation tissue, and epithelial tissue. Depending on the severity of the ulcer, it may initially appear covered with a mixture of black necrotic tissue and yellow slough. These tissues contain dead skin cells and cellular debris that result from bacterial infection and white blood cell activities. These tissues are unhealthy

and need to be debrided to promote healing. As ulcers heal, healthy red granulation tissue starts to grow from the base of the ulcer gradually replacing the black necrosis and yellow slough. Granulation tissue consists of a collagen-based extracellular matrix combined with newly formed blood capillaries. The growth of granulation tissue indicates that the ulcer is healing and the patient is positively responding to the treatment. At later stages of ulcer healing, pink epithelial tissue starts to grow from the edges of the ulcer slowly covering the granulation tissue and eventually closing the ulcer.

It is evident from the discussion above that the physical appearance of the ulcer surface provides valuable information on the severity and healing status of the ulcer. Hence, it must be thoroughly examined and assessed. The colour of the ulcer surface changes gradually from black to yellow to red as the ulcer's tissues evolve throughout the healing process. At any one time during the course of the treatment, all four types of tissues may be present on the ulcer surface. Recognizing and measuring the amount of each tissue, particularly granulation tissue, is a well-known and approved method of ulcer assessment and understanding of healing progression.

1.2 The Role of Digital Imaging

In medicine, the use of digital photography has been employed to provide pictorial representations of chronic wounds and their physical appearance. In most dermatology and wound care clinics, ulcer photographs are normally utilised as documented records that are made accessible to the medical personnel for an easy reference to patients' medical histories. Furthermore, colour images of chronic ulcers are acquired at successive visits to provide chromatic data that help clinicians determine the severity and healing progression throughout the course of treatment [10].

The accuracy of the information contained in these images depends greatly on the performance of the device used to acquire the images and the surrounding environment conditions. Hence, the correct standardization of these parameters is essential to obtain a uniform record of the same patient over the period of the

treatment [11]. Digital single-lens reflex (DSLR) cameras offer many advantages over the compact digital cameras represented mainly in their unique viewing system in which a mirror reflects light from the lens through a separate optical viewer. When acquiring images, the mirror flips out of the way allowing light to fall onto the sensor. DSLR cameras are used to provide accurate and high-resolution colour images that can be acquired within a few seconds.

The use of digital imaging in medicine enables data to be easily acquired in remote locations and transmitted to the main reference where clinicians can perform ulcer analysis and assessment [11]. This forms the basis of telemedicine, which ensures providing quality healthcare regardless of the geographical location of the medical personnel.

1.3 Problem Statement

In most wound care clinics, the use of non-invasive assessment methods is preferred to avoid any contact with the ulcer, which may cause pain or discomfort to the patients and expose the ulcer to the risk of infection. Most of the assessment methods implemented currently depend on a visual inspection of the ulcer appearance and the tissue types on the ulcer's surface [11]. Several schemes are utilized to evaluate the ulcer severity and healing progression based on the colours of the tissues such as the red/yellow/black scheme and the Wound Healing Continuum (WHC) [10], [12]. Using these schemes, the ulcer's surface tissues are described as estimated percentages of red, yellow, and black colours that refer to granulation, slough and necrotic tissues, respectively.

Although these schemes are widely used in clinical settings to provide a somewhat quantitative evaluation of ulcer tissues, they are based on the human vision and inspection. The human vision inspection is highly subjective and suffers from huge inter and intra-rater variability and hence not sufficient to perform an accurate assessment. Inaccurate assessment of the ulcer's severity status leads to improper clinical decisions regarding treatment and may prolong the healing duration or worsen the ulcer condition in some cases. There is a need for an objective and quantitative

method that provides accurate and reproducible assessment of ulcer condition and healing progression.

Chronic ulcers heal slowly and detecting small changes on the ulcer's surface visually is difficult. The ulcer's surface appearance changes gradually throughout the treatment course as depicted in Figure 1.2 [10]. Depending on the condition and severity status of the ulcer, it can initially appear covered with a layer of black necrotic tissue (stage 1) or overlying layers of black necrotic tissue and yellow slough (stage 2). As the ulcer heals, red granulation tissue starts to grow from the base of the ulcer gradually replacing the black necrosis and yellow slough, filling the wound cavity and reducing its volume (stage 3). As the ulcer is filled with granulation tissue (stage 4), pink epithelial tissue grows from the ulcer boundaries covering the granulation tissue (stage 5) and eventually closing the ulcer (stage 6).

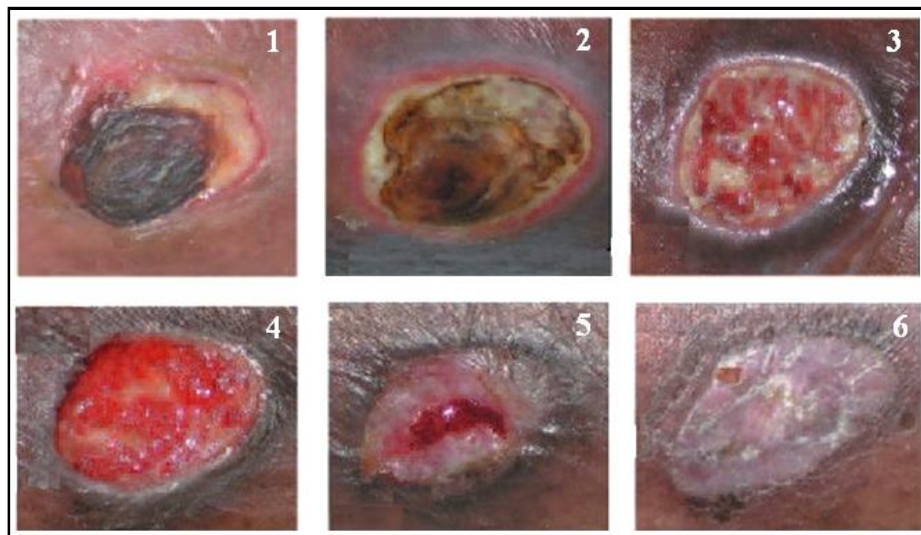


Figure 1.2: Typical healing stages of an ulcer [10]

If the ulcer is responding to the treatment, healing would be promoted by the growth of the granulation tissue on the ulcer's surface provided that there are no underplaying aetiologies that delay healing. On the other hand, if the current treatment is not effective, the granulation tissue will not grow and unhealthy black necrosis and yellow slough will be present on the ulcer's surface as a result of infection. A detailed elaboration on ulcer healing and the physical appearance of chronic ulcers is given in Chapter 2 (sections 2.4 and 2.7.2). Detecting small tissue changes that reflect early stages of healing accurately would enable the clinicians to

determine the efficacy of the current treatment and make appropriate clinical decisions such as the medicine applied, the type of ulcer dressing, and so on. This reflects on the effectiveness of the ulcer care and management in terms of time and cost of treatment.

Colour has been utilised as the key element for analysis in colour image processing in the field of wound assessment for most of the work that has been developed so far. Earlier developed methods in the area of wound tissue classification and segmentation are based on analyzing colour information in a single colour channel in digital images using conventional colour models such as RGB and HIS [13-16]. Ulcer tissues normally appear mixed with each other on the ulcer surface and hence the use of only one colour channel is not adequate to classify each type of tissue fully. Studies showed that pixel clusters in RGB space for a given type of ulcer tissues formed an irregular shaped 3D cloud that distinguished the three types of necrotic, slough and granulation tissues and hence colour pixels are considered in all colour channels in the image to be able to classify different ulcer tissues [17-19]. Segmentation-based classification of wound tissues utilising colour and texture attribute was also proposed [20], [21]. The method utilises unsupervised segmentation to segment colour wound images into different regions. It then extracts both colour and texture descriptors from coloured images for automatic classification and labelling of these regions.

The major drawback of the colour content interpretation in the image is that it is always impaired because of the unavoidable differences in the acquisition conditions present when acquiring the images such as the type of camera used, the illumination in the room, and the type of flashlight used. These varying conditions alter the colour quality and scales in images which leads to inaccurate results which poses the main shortcoming of the analysis based on colour features and attributes.

1.4 Research Hypothesis and Implemented Approach

The colours of ulcer's tissues are produced due to the human vision perception of the light reflected from ulcer's surface. Most of the light penetrates into the ulcer and

skin tissues and follows a complex path where it interacts with different interior structures and pigments and gets reflected back from the ulcer [22]. These interactions (mainly absorption and scattering) are responsible of changing the spectral composition of light which reflects the optical properties of the ulcer tissue structures and pigments. The reflected light is captured by the human eye producing colour vision and can be registered with cameras producing colour digital images. Hence, an understanding of the colour image formation would reveal diagnostically important facts about the internal structure and composition of the skin ulcers and the underlying causes of the changes during ulcer healing [23]. Detecting these causes can provide a better analysis of wound tissues.

The first indication of ulcer healing is the growth of the healthy red granulation tissue on the ulcer's surface. Granulation tissue appears red in colour when viewed under the visible light due to the pigment haemoglobin present in the newly-formed blood capillaries within the tissue [24]. This is explained by the fact that the haemoglobin pigment (both oxy-haemoglobin and deoxy-haemoglobin) gives off a reflection of the light in the range of 600nm and above as shown in Figure 1.3 which corresponds to the red colour component in the visible light spectrum [22]. A detailed explanation of the formation of the ulcer's surface colours, particularly the granulation tissue, is given in Chapter 2 (section 2.10).

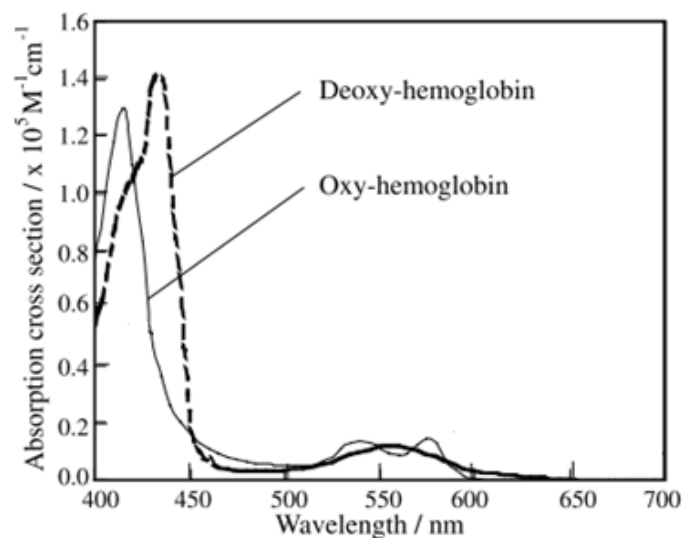


Figure 1.3: Absorption spectra of oxy-haemoglobin and deoxy-haemoglobin [22]

Studies show that haemoglobin contains certain optical characteristics that can be detected in colour images and used to show their content within human skin [25], [26]. Therefore, this study focuses on utilising the optical characteristics of the pigment haemoglobin and determining its content within and below the visible surface of ulcers. It is hypothesised that identified regions of haemoglobin distribution can be utilised as image markers to detect regions of granulation tissue indicating the ulcer healing progression. The approach is to apply data transformation utilising independent component analysis to extract source grey-level images that show the distribution of pigment haemoglobin. Extracted haemoglobin images show regions of haemoglobin distribution that reflect regions of granulation tissue on ulcer surface. This approach is fundamentally unique in a way that it does not focus on colour image features and attributes directly from the colour images like previous works in this field; instead it draws an understanding of tissue histology utilizing a physics-based interpretation of the image colour.

1.5 Research Objective

Since the first indication of ulcer healing is the growth of granulation tissue, this research focuses on identifying regions of granulation tissue from colour images of chronic ulcers. Identifying and quantifying the amount of detected granulation tissue gives an indication of the healing progression which reflects on the efficacy of the ulcer management and treatment.

The objective of this research work is to develop an image analysis system that identifies and detects regions of granulation tissue on the ulcer's surface based on the content of pigment haemoglobin. The developed system would be able to detect regions of granulation tissue that are mixed with other tissues on the ulcer surface and cannot be discerned visually. This is very significant in detecting early stages of ulcer healing especially in ulcers where granulation tissue is spreading slowly over the ulcer surface and cannot be detected using simple visual inspection.

1.6 Scope of Work

The study is conducted using colour images of chronic leg ulcers of different types; vascular (venous and arterial), pressure, and diabetic ulcers; that contain a mixture of tissues acquired at Hospital Kuala Lumpur, Malaysia. This is very crucial to this study as it ensures working on ulcers images taken under actual acquisition conditions. The target population for this study is adult patients above eighteen years with chronic leg ulcers who are attending the ulcer clinics at the Department of Dermatology and Outpatient Department at Hospital Kuala Lumpur during the study period. This research work is a collaborative study between Universiti Teknologi Petronas (UTP) and Hospital Kuala Lumpur. It has been approved by the Ethics Committee of Ministry of Health, Malaysia, and registered with the National Medical Research Registry; (NMRR, Malaysia) under study code NMRR-11-50-8340.

It is hoped that the work presented in this study contributes to computer-aided diagnosis, especially in the field of ulcer assessment. Ultimately, the goal is to develop a new objective and non-invasive scheme to assess the healing progression of chronic ulcers in a more precise and reliable way.

1.7 An Overview of the Thesis Structure

The thesis is structured according to the sequence of the processes involved in the development of the granulation tissue detection system. The thesis is organized as follows:

Chapter 2 discusses ulcer anatomy, ulcer care and management as well as clinical assessment of the healing progression. The chapter also presents an overview of the related research work on wound tissue assessment and analysis using digital imaging.

Chapter 3 explores the concept of colour vision and the formation of digital colour images. It also investigates the mathematical formulation of important statistical data analysis and image processing techniques that are utilized to develop the granulation tissue detection system.

Chapter 4 describes the developed system for detecting granulation tissue regions from colour images of chronic ulcers. The chapter presents a block diagram of the overall granulation tissue detection system development. Each process of the system development is then explained in detail accordingly.

Chapter 5 analyses the application and performance of the developed granulation tissue detection system. First, the performance of the developed granulation tissue detection system is investigated utilising ulcer tissue reference images. Then the application of the developed granulation detection system is explored by utilising the system to detect regions of granulation tissues on real ulcer images.

Chapter 6 summarises the main ideas and findings of this study. The chapter also presents the main contributions of the study and highlights possible avenues for enhancement and future work.

CHAPTER 2

WOUND CARE AND ANALYSIS

2.1 Introduction

In this chapter, a medical background on skin chronic wounds and ulcers is presented. In particular, the chapter elaborates on ulcer anatomy and histological properties, ulcer care and management as well as the clinical assessment of the healing progression. The chapter also presents an overview of the related research work on wound tissue assessment and analysis using digital imaging.

Section 2.2 defines chronic wounds, their prevalence and economical impact on society. Section 2.4 illustrates the wound healing process and the formation of chronic wounds. Chronic leg ulcers, their types and underlying aetiologies are discussed in section 2.5. Ulcer care and management procedures are elaborated in section 2.6. Section 2.7 demonstrates ulcer assessment parameters focusing on ulcer surface tissues as an important assessment parameter. Several clinical and imaging based techniques of chronic wound tissue assessment are discussed in sections 2.8 and 2.9 respectively. Section 2.10 illustrates the importance of detecting the growth of granulation tissue to detect ulcer healing and investigates the optical characteristics of haemoglobin pigment upon which the research hypothesis is formulated. Section 2.11 summarizes the main ideas and findings of this chapter.

2.2 Chronic Wounds and Ulcers

In pathology, a wound refers to any discontinuity of an anatomical structure and function of skin tissues caused by a trauma [1], [27]. Wounds appear as open lesions that involve the epidermis and several layers of the dermis in the skin. Figure 2.1 represents a schematic illustration of a deep wound involving the epidermal layer and parts of the dermal layer of the skin.

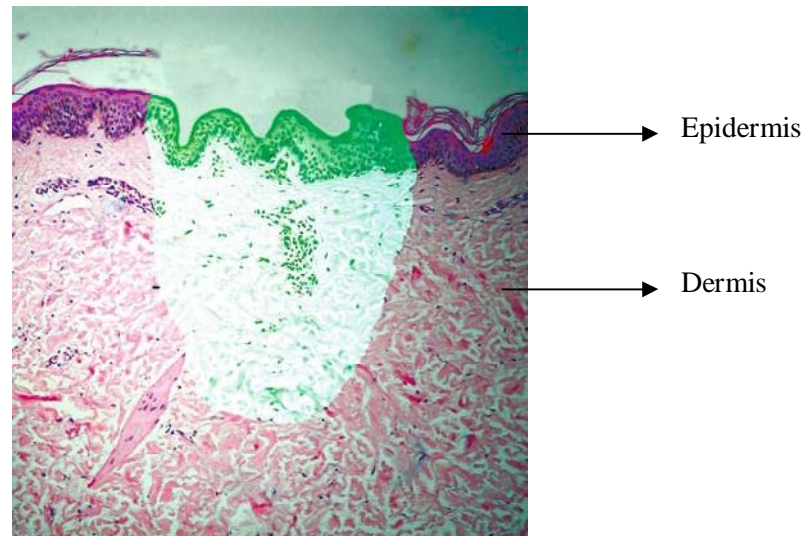


Figure 2.1: Schematic illustration of a deep wound [1]

There are two types of wounds: acute wounds and chronic wounds. Acute wounds heal within three or four weeks from the time of injury, depending on the size and severity of the wound, leaving a minimal scar that fades away with time [28], [29]. Wounds that do not follow the normal healing process within three to four months from the time of the injury are classified as chronic wounds [1], [28]. Such wounds normally fail to heal due to some underplaying aetiologies or improper wound management which impairs the natural process of healing [3], [29]. Ulcers are a common type of chronic wounds.

2.3 Prevalence and Economic Impact of Chronic Wounds

Accurate prevalence estimates on chronic ulcers had not been published until quite recently. Earlier studies that were conducted in Europe established only a few earlier

estimates between 1.48 - 3.0/1000 populations in some of the major areas such as Scotland, Ireland and Sweden [30-33]. However, these estimates were regionally based and were concluded from studies that had been conducted over short periods. Hence, it is not an accurate way to establish the prevalence of chronic wounds in Europe based on these figures. According to Werdin *et al.*, approximately 1.0 - 3.0% of the population have the potential to develop chronic ulcers during the course of their lifetime [3]. In Malaysia, the prevalence of chronic foot ulcers in patient with diabetes between 1999 - 2008 was reported as 9.9% with an annual prevalence of 1% [4]. The prevalence increases significantly due to several factors such as the increase in population age, underlying aetiologies of diabetes, and venous and arterial insufficiency as well as the inclusion of foot ulcers which corresponds to high prevalence figures [3], [34].

Chronic wounds also introduce an economic dilemma when it comes to wound management and care. In the United States, chronic wounds affect 3 to 6 million people and their treatment costs an estimated \$5 billion to \$10 billion each year [3]. The annual ulcer care is estimated to be around £400 million in the United Kingdom [5]. The average cost of treating diabetic ulcers was estimated to be more than RM 600 per day in Malaysia in the year of 2006 [6]. Wound care costs can be greatly reduced if a proper, thorough and objective assessment is conducted to determine the appropriate course of treatment.

2.4 Wound Healing Process

Wound healing is the complex and dynamic process that occurs after skin injury to restore the anatomical structural continuity and function of the skin [27]. Wounds generally heal by growing new tissue from the base of the wound following four main distinct yet overlapping stages: Haemostasis, Inflammation, Proliferation, and Maturation. Figure 2.2 illustrates the four main phases of healing and their estimated durations which vary depending on the wound severity and the course of treatment.

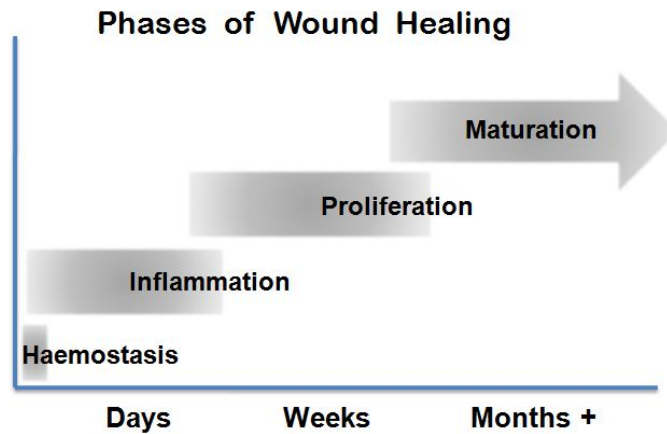


Figure 2.2: Wound healing phases

2.4.1 Haemostasis

This phase occurs within minutes after injury and may remain for a few days in severe wounds [28]. When the skin gets injured, small cell fragments called the platelets form a fibrin plug that stops bleeding and protects the wound from bacterial contamination [27]. During this phase, blood vessels dilate which causes an increase in the blood supply to the wound site. This phase is characterized with redness, heat, pain, and swelling with some loss of sensation in the wounded area.

2.4.2 Inflammation

This phase, which normally lasts 4 or 6 days, aims to clean the wound site and prepare it for wound healing [1]. During this phase, platelets stimulate white blood cells such as neutrophils and macrophages to clean the wound site from bacteria and debris through the process of phagocytosis [1], [15], and [17]. A yellow-green slough tissue is observed at this stage because of phagocytosis and needs to be debrided as part of wound management to ensure healthy healing.

2.4.3 Proliferation

This phase starts at day 4 or 6 and lasts up to two or three weeks in acute wounds [28], [29]. At this phase, connective cells, called fibroblasts, deposit collagen which

is used to build an extracellular matrix which serves as a platform for new cells and blood vessels to be built [1], [27]. Fibroblasts also stimulate endothelial cells to form new blood vessels via a process of angiogenesis. The newly formed blood capillaries branch out and invade the extracellular matrix within the wound site forming the granulation tissue which serves as the foundation for tissue repair [1], [29]. As more collagen gets deposited on the matrix, the elasticity and strength of the new formed granulation tissue increases.

2.4.4 Maturation

This phase lasts from 6 months till two years in acute wounds [28], [29]. At this phase, epithelial cells from the edge of the wound begin to migrate across the wound surface over the granulation tissue forming a pale layer of epithelial tissue which closes the wound [29]. Strength is gradually built up in the tissue as collagen fibres mature and become more stable and organized.

It is very important to understand the phases of wound healing to provide the best care in daily clinical practice. Understanding the role of white blood cells in protecting the wound site and stimulating the growth of blood and fibre cells to form the new granulation tissue encourages the medical personnel to decide on the treatment that best protects the wound and provide a good environment to promote healing of the wound. It is also important to remember that some of these stages may overlap and at any given time, evidences of more than one stage may appear in the wound especially for chronic wounds which do not follow a normal predictable course of healing.

2.5 Chronic Leg Ulcers

Leg ulcers are chronic wounds that occur on the lower limbs and constitute around 98% of all lower limb wounds [34]. There are three main types of leg ulcers according to the aetiologies that cause them: vascular (venous and arterial), diabetic (neuropathic) and pressure ulcers. Most leg ulcers are either vascular or diabetic and

affect about 1% of the adult population and 3.6% of people older than 65 years [7]. Figure 2.3 indicates common locations of several types of chronic leg ulcers.

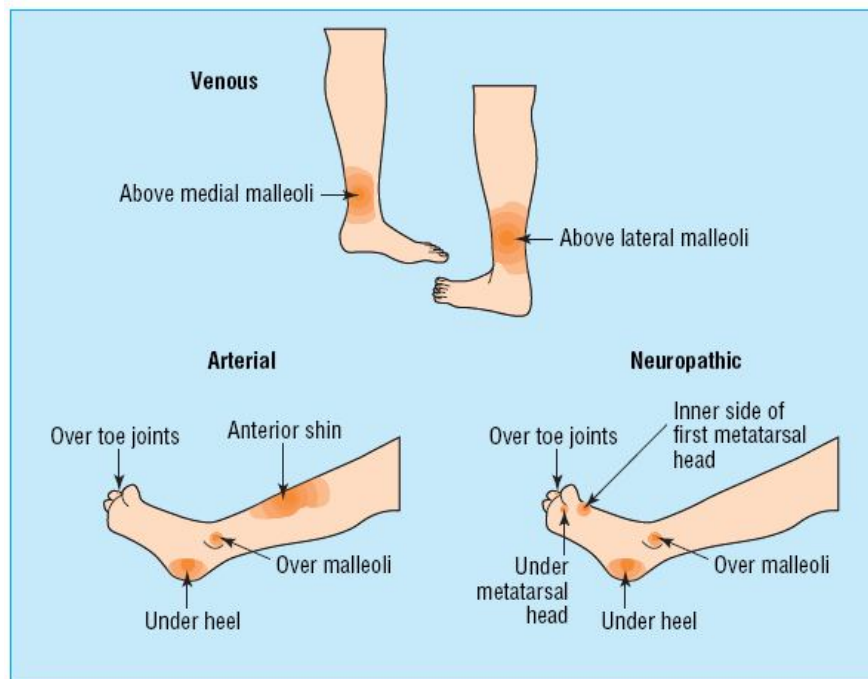


Figure 2.3: Most common locations of leg ulcers [7]

2.5.1 Vascular Ulcers

These ulcers are caused by aetiologies related to blood vessels (veins and arteries) and are divided into two types: venous and arterial ulcers.

Venous Ulcers: Venous ulcers are the most common of leg ulcers and are associated with venous insufficiency which occurs when the veins get damaged and are not able to push the blood back to the heart which results in pooling of the blood around the lower part of the leg [35], [36]. The increased pressure of the blood in the veins obstructs the flow of oxygen and nutrients to the skin cells causing cell death and ulceration [35]. Venous ulcers appear as irregular shaped, partial thickness moist wounds with a well defined boundary surrounded by highly pigmented skin at [7], [37]. Figure 2.4 shows a chronic venous ulcer.



Figure 2.4: A chronic venous ulcer [1]

Arterial Ulcers: Arterial ulcers are associated with arterial perfusion which refers to poor blood circulation and fusion at the lower leg due to large cholesterol and fatty materials deposited in the arteries. The arteries fail to deliver oxygen and nutrients to the cells resulting in tissue breakdown and ulceration [35]. These ulcers appear relatively smaller than venous ulcers with regular, punched out boundary and dry base [7], [38]. Figure 2.5 shows a chronic arterial ulcer.



Figure 2.5: A chronic arterial ulcer [39]

2.5.2 Pressure Ulcers

They are known as pressure sores or bedsores and mainly are caused by excessive unrelieved pressure which causes poor blood circulation and prevents oxygen and nutrients from reaching the cells which causes ischemia and tissue breakdown [40], [41]. Pressure ulcers normally occur at bony areas of the body such as tailbones, hips, buttocks, heels, elbows and shoulders and appear as deep wounds with regular boundary. Figure 2.6 shows a chronic pressure ulcer at the heel.



Figure 2.6: A chronic pressure ulcer [42]

2.5.3 Diabetic Ulcers

Diabetic ulcers often occur at the toes and heels. These ulcers are caused by the combination of arterial leakage and nerve damage (diabetic neuropathy) and they normally start off as calluses or corns at weight bearing areas such as heels and toes. Patients would not be able to feel or notice any pressure or small injuries that get worsened with time and develop into ulcers [35]. Diabetic ulcers usually appear as small deep wounds with smooth edges on the feet, specifically on toes and heels [38]. Figure 2.7 shows a diabetic leg ulcer.



Figure 2.7: A chronic diabetic ulcer [1]

2.6 Ulcer Care and Management

Ulcer care aims to create an optimal healthy environment with minimal exudates to promote ulcer healing [43], [44]. Chronic ulcers do not follow a predictable course of healing and keep on evolving slowly over time. Healing may prolong usually due to underlying aetiologies such as venous insufficiency, arterial perfusion, prolonged pressure and diabetes. These aetiologies cause further wound inflammation and accumulation of debris and foreign materials, which impairs the natural course of healing.

Ulcer management should aim to remove the factors impairing the healing by treating any underlying aetiologies and preparing the ulcer for healing. Hence, it is important that medical personnel attending to the ulcer have sufficient knowledge on the wound anatomy and physiology, and are able to identify factors that impair healing [45]. Misdiagnosis of aetiologies can cause improper clinical decisions and lead to long periods of treatments. Furthermore, the ulcer care plan should include an accurate initial assessment of the ulcer to determine the appropriate treatment as well as continuous monitoring of the healing progression throughout the course of treatment [46]. Ulcer care mainly involves cleaning the ulcer, removing unhealthy tissues and debris, assessment for bacterial infection and selection of the appropriate dressing [47].

2.7 Chronic Ulcers Assessment and Documentation

For efficient ulcer care and management, an initial accurate assessment of the ulcer is important to provide baseline information on the severity status and to determine the appropriate course of treatment [8], [9]. After an appropriate course of treatment is determined, ulcer care should include an ongoing consistent assessment and recordings of the physiological changes of the ulcer at specific intervals throughout the course of the treatment to predict healing and monitor the ulcer for complications and improper management [44], [46]. Ulcer assessment documentation allows information to be easily accessed by clinicians to review, reevaluate and determine

alternative choices of dressing and treatment when required which reflects an overall improvement in ulcer management and care [9], [45].

2.7.1 Ulcer Assessment Parameters

Ulcer assessment is normally recorded using specialised assessment charts that include several assessment parameters. These parameters are the location and size of the ulcer, the patient's medical history, the physical appearance of the ulcer, the condition of the skin surrounding the ulcer, the cause and severity of the pain associated with the ulcer and the nature and amount of the exudates on the ulcer surface [38], [44].

Patient's Medical History: One of the important assessment parameters is to inspect the patient's medical history of previous ulcers and the corresponding treatments provided, the duration of the current ulcer as well as information on any type of vascular or diabetic diseases in the family [47].

Ulcer Appearance: The physical appearance of the ulcer plays a very important role in evaluating the ulcer severity and determining the appropriate course of treatment. Inspection of the ulcer's appearance includes measuring the ulcer's dimensions, such as surface area, depth and volume, and classifying and quantifying the different types of tissues that exist on the ulcer surface.

Skin Surrounding the Ulcer: Assessment should also include an inspection and analysis of the skin surrounding the ulcer, for callus formation, excess moisture oedema or erythematic irritated skin [5], [32], and [33].

Pain: Pain is a common symptom associated with chronic ulcers reflecting the presence of underlying aetiologies or the exposure of nerve endings [48]. The frequency and severity of the pain is normally evaluated using verbal rating scales to determine the appropriate treatment. Incorporating specific leg exercise routines into the course of treatment helps to manage and reduce the pain [49].

Exudates: The amount and type of exudates vary throughout the ulcer healing process. A considerable amount of exudates is noticeable during the inflammatory stage of healing compared to maturation [50]. However, heavy exudates can indicate prolonged inflammation or early signs of an increased bacterial load or infection [44]. Ulcer exudates should be inspected in terms of type, quantity, colour and odour to determine their effect and suggest appropriate treatments, accordingly [47], [50].

2.7.2 Physical Appearance of the Ulcer Surface

The appearance of the ulcer surface provides important information on the healing status of the ulcer. Hence, it must be thoroughly examined and assessed. There are four main types of tissues existing on the ulcer surface: necrotic tissue, slough tissue, granulation tissue, and epithelial tissue.

Necrotic Tissue: Necrotic tissue appears as black or dark brown dehydrated tissue caused by the death of cells on the wounds surface due to bacterial infection, toxin or trauma [47], [48]. The existence of necrotic tissue on the ulcer surface prolongs healing and stimulates bacterial growth. It should be debrided to promote a healthy environment for healing. Figure 2.8 shows a leg ulcer covered fully with black necrotic tissue. After removing the necrotic tissue, the wound bed will contain mostly slough or both slough and granulation tissue depending on the amount of slough existing on the wound surface.



Figure 2.8: A leg ulcer covered with black necrotic tissue [1]

Slough Tissue: Slough tissue appears as a yellow-green or white soft tissue caused by the accumulation of cellular debris on the wound surface resulting from

phagocytises during the ulcer healing process [48]. Slough facilitates the growth of bacteria, prolonging ulcer healing, and should be debrided to promote a healthy environment for healing. Figure 2.9 shows a leg ulcer mostly covered with a yellow-green loose layer of slough. After removing the slough, the ulcer stimulates the growth of granulation tissue given the condition that there are no underlying factors that might impair healing.



Figure 2.9: A leg ulcer covered with yellow slough [1]

Granulation Tissue: Granulation tissue is a red moist tissue with a granular or peddled texture [47]. This tissue is formed during the proliferation stage of the ulcer healing as the combination of a collagen based extracellular matrix with the newly formed blood capillaries [1], [29]. Granulation tissue is red due to the vast content of blood capillaries [24], [48]. Figure 2.10 shows a healing leg ulcer covered with healthy granulation tissue.



Figure 2.10: An ulcer covered with granulation tissue [51]

Epithelial Tissue: Epithelial tissue appears as pink pale tissue on the surface of the ulcer. Epithelial cells start to grow from the edges of the ulcer across the surface

gradually covering the granulation tissue and closing the wound [47], [48]. Epithelial cells can also grow from hair follicles and sweat glands in partial thickness ulcers [50]. Figure 2.11 shows an ulcer fully covered with pale epithelial tissue.



Figure 2.11: An ulcer covered with pink epithelial tissue [47]

In terms of both dimensions and colour, an ulcer's surface appearance changes gradually throughout the treatment course as depicted in Figure 2.12 [10]. Depending on the condition and severity status of the ulcer, it can initially appear covered with a layer of black necrotic tissue (stage 1) or overlying layers of black necrotic tissue and yellow slough (stage 2). As the ulcer heals, red granulation tissue starts to grow from the base of the ulcer gradually replacing the black necrosis and yellow slough, filling the wound cavity and reducing its volume (stage 3). As the ulcer is filled with granulation tissue (stage 4), pink epithelial tissue grows from the ulcer boundaries covering the granulation tissue (stage 5) and eventually closing the ulcer (stage 6).

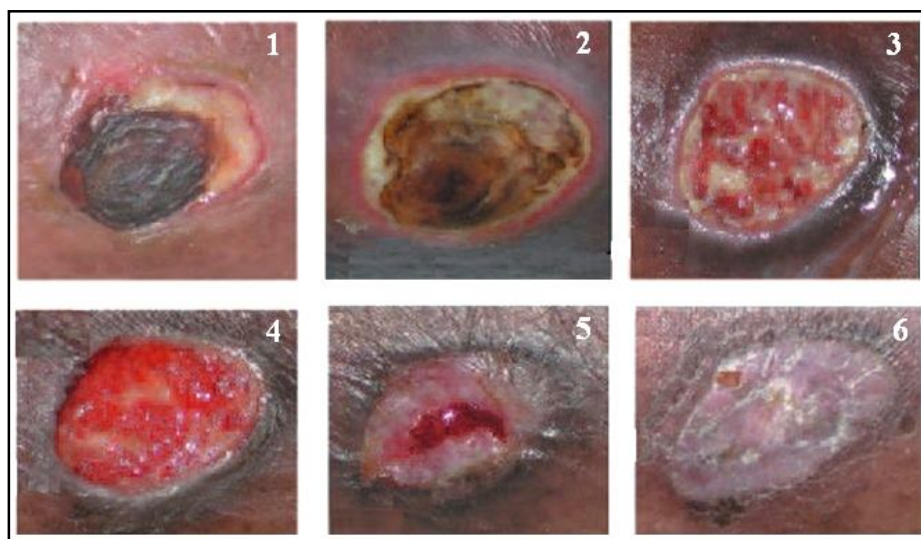


Figure 2.12: Typical healing stages of an ulcer [10]

Since chronic ulcers do not follow a normal course of healing, all four types of tissue could exist at the same time. Detecting and quantifying these tissues is a very important parameter in ulcer assessment. In clinical practice, physicians normally depend on non-invasive methods for ulcer tissue assessment to avoid causing any pain or discomfort to the patients. Most of the methods implemented depend on a visual inspection of the ulcer appearance and analysis of the tissue types and amounts on the ulcer surface [11].

2.8 Ulcer Tissues Assessment in Clinical Practice

As explained earlier, the ulcer surface provides valuable information on healing progression or regression throughout the treatment course. Analyzing and inspecting the type and amount of each tissue on the ulcer surface is very important in ulcer care and management and needs to be documented regularly [47]. In clinical practice, ulcers are normally evaluated based on a simple visual inspection utilizing several schemes based on the colours of the tissues [10], [12].

Some developed schemes have been designed to describe the appearance of the ulcer surface in terms of percentages of each tissue colour such as the red/yellow/black scheme [47]. Using this scheme, ulcers surface tissues are described as estimated percentages of red, yellow, and black colours which refer to granulation, slough and necrosis respectively. Figure 2.13 shows a chronic ulcer that has been assessed utilising this scheme; it is seen to have approximately 25% black necrosis, 35% yellow slough and 40% red granulation. The more the shift towards the red colour is, the better the ulcer is healing. This scheme is widely used in hospitals and clinical settings and is normally recorded on the patient assessment chart.



Figure 2.13: An ulcer with approximately 25% black, 35% yellow and 40% red [47]

Gray *et al.* developed the Wound Healing Continuum (WHC) which identifies the tissue colours on the ulcer surface and associates them to a colour spectrum extending from black till pink with intermediate gradations as shown in Figure 2.14 [12]. In this scheme, the colour spectrum extends from black at the left side of the spectrum through yellow, red and continues until pink at the right side of the spectrum reflecting the gradual change in ulcers colour as it heals. If the ulcer has a mixture of tissues of different colours, the most significant colour is attributed to the ulcer utilizing this scheme.

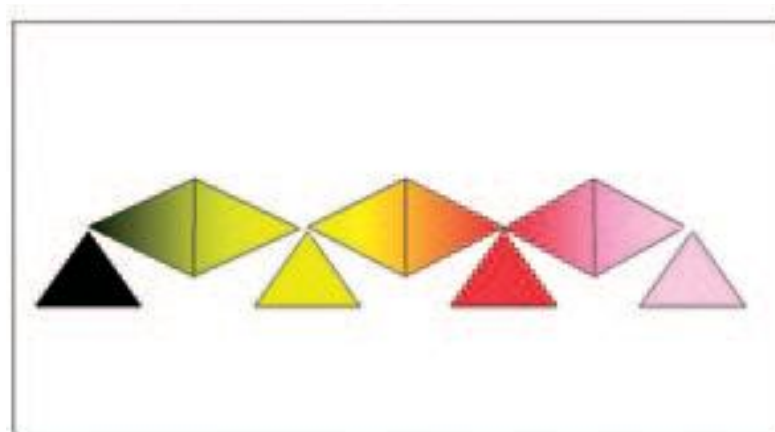


Figure 2.14: Wound healing continuum [12]

Clinicians utilise this scheme to make clinical decisions on ulcer status by identifying the ulcer colour which is furthest to the left and determining the appropriate treatment and ulcer management procedures which promote healing and shift the ulcer colour to the right [12]. For example, if an ulcer is described as yellow/red using this scheme, this refers to an ulcer that contains both slough and

granulation tissues. Hence, ulcer management should aim to remove the yellow slough and create a fully granulating ulcer that should gradually be covered with pink epithelial tissue following the normal course of healing.

These methods are simple and widely used in clinical settings to evaluate the ulcer status and progression towards healing. However, they are based on the human vision perception and thus the inspection of the ulcer is subjective and lacks precision and consistency and hence not sufficient to perform tissue analysis. Moreover, chronic ulcers change slowly over time as they heal and hence recognizing small changes with simple visual inspection is difficult. Therefore, monitoring the healing of chronic ulcers requires objective, precisely quantitative and reproducible assessment parameters.

2.9 Ulcer Tissue Assessment using Digital Imaging

In medicine, colour photographs of chronic wounds provide reliable chromatic data and a pictorial representation of the wound's environment, severity and healing progression throughout the course of the treatment [10]. The accuracy of the colour information contained in these images depends greatly on the camera and illumination used and image resolution of the wound. Hence, the correct standardization of these parameters is essential to obtain a uniform record of the same patient over the entire period of the treatment [11]. The use of digital imaging enables data to be easily acquired in remote locations and transmitted to the main reference where clinicians can perform wound analysis and assessment [11].

Wound imaging requires the colour information for an effective analysis of tissue. Colour plays an important role in assessing and diagnosing the tissue characteristics and healing status as the ulcer tissues changes in appearance and colour as they heal. Thus, imaging techniques based on colour digital images are developed to provide precise, objective and reliable data that aid medical practitioners to evaluate healing status of ulcers.

Callieri *et al.* developed an integrated wound assessment tool that incorporates both 3D measurements of wound dimensions as well as 2D colour assessment of tissues on wound's surface [52]. The segmentation of different tissues was implemented by manually selecting a colour seed in the image and utilising the region growing algorithm to segments regions of different types of tissues based on a pre-defined similarity measure. Although this technique utilises colour images, the classification is based on the user selection of a specific colour seed and hence the classification obtained is subjective and not reproducible.

Imaging techniques have been developed and implemented on colour images of chronic wounds and ulcers to segment and classify the different types of tissues on wounds surfaces as a measure of their healing. Most of the methods developed in this area are based on three main approaches:

- a) Information from a Single Colour Channel
- b) RGB Histogram Distributions
- c) Colour and Texture Descriptors

2.9.1 Information from a Single Colour Channel

Earlier developed methods in the area of wound tissue classification and segmentation are based on analyzing colour information in a single colour channel in digital images using conventional colour models such as RGB and HIS.

Herbin *et al.* developed methods to quantify the colour content and design colour-based healing indices from digitized RGB images of wounds [13], [14]. Digital images of artificial skin blisters induced on the forearms of eight healthy volunteers were acquired during a clinical trial conducted to test the blanching effects (reduce skin redness) of a new topical corticosteroids (TC) drug [14]. The drug was applied on two blister sites for every patient for a period of 12 days. Colour photographs were obtained of each blister site at days 1, 3, 5, 6, 7, 8, 9 and 12. The acquisition and digitization of the colour images were performed using a high quality vidicon camera equipped with a ring flash to provide a homogenous illumination. The digitized colour images were recorded as Red, Green and Blue frames using tri-chromatic

filters. Sixty nine images were acquired and digitized (8 volunteers with two blister sites and 8 days of photography). Colour variables r, g, b H, and S were derived from the main Red, Green and Blue digital images and were used to design the colour index (Icolor) based on the variations between the mean of each variable in the blanching site compared with the mean in the surrounding healthy skin taking into account the variation in the skin colour of the various subjects [14]. The variable “g” was selected for the colour index as it was seen to give accurate results compared to the results of the visual assessment of the observers. Figure 2.15 gives the values (mean and standard deviation) of the developed colour index (Icolor) at days 1,3,5,6,7,8,9 and 12 on the blisters treated with the TC drug. Throughout the healing of these wounds, the value of the healing index increased (as the wound redness decreased) from 24.2% at day 5 to 28.7% on day 12. At day 12, the wound region colour was very close to the normal skin colour, which was estimated to be 31.4%.

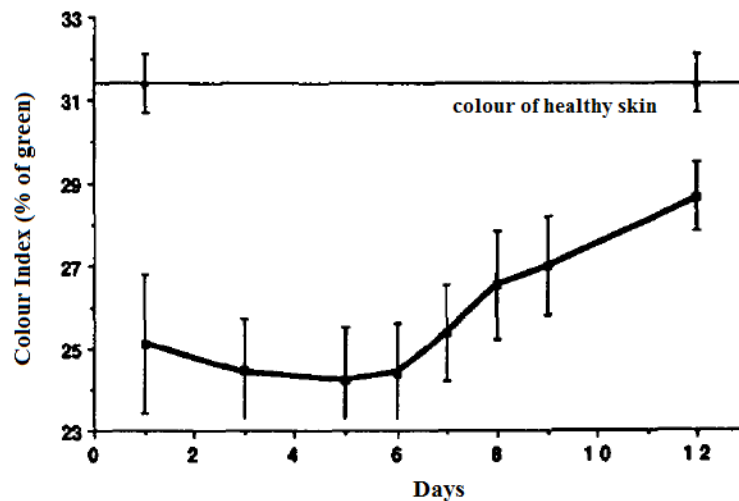


Figure 2.15: Time course of colour index (Icolor) in percentages of green on 16 wound sites [14]

Although the developed colour index produced more accurate and reliable results when compared to the visual assessment, its design was affected by light conditions and the colour of the patient’s skin. The index was developed based on light skinned Caucasians and hence different skin tones would produce different results when analyzing the colour variables. Moreover, this study was conducted on uniformly coloured wounds specially created for this purpose and hence the developed indices are not applicable to analyse real wounds that have a high variety of colours.

Hoppe *et al.* conducted a study to develop and apply a computer system to analyse the colour variability between images taken under clinical conditions with a particular attention given to assessing the amount of slough in leg ulcers [15]. RGB colour images of chronic leg ulcers were acquired from 30 patients using a 3CCD digital video camera provided with a flashlight to provide a uniform and adequate illumination. A colour scale (FUJI colour scale) was included in the image close to the wound as shown in Figure 2.16 as a colour reference to compare the variability of the colour values between different images.



Figure 2.16: FUJI colour scale held near wound [15]

Since the aim of this study is to study the colour variations of wound tissues in digital images acquired in varying lighting conditions, the acquired images were represented and analysed in the HIS colour model instead of the RGB colour model as the later is very sensitive to variation in lighting conditions. Each of the components H, I and S were analysed in red colour patches of 10 wound images acquired with different lighting conditions. It was noted that the H (Hue) component experienced less variations as compared to the-I (intensity) and S (saturation) component (10% over its range) and hence was included in the study. The red hue values were found to be within the range of 120° - 180° and the yellow hue 180° - 240° .

The range of hue values occurring within each wound region was analysed in 10 ulcer images and found to fall within the hue values of 110° - 190° extending over the whole range of red into yellow. Two thresholds were selected based on clinicians' perception of the slough colour which were $T1=180^{\circ}$ and $T2=240^{\circ}$ and were used to

calculate the amount of slough within the wound region in relation to the overall size of the wound in 30 images of leg ulcers. All pixels that fell within these two thresholds were calculated and compared to the visual inspection (% amount) of slough determined by the doctors.

The results obtained showed agreement in 75% of the cases between the clinicians' assessments and the computer analysis. However, the computer assessment was based on analysis of only the hue (H) component which, according to the analysis of the results obtained, also experienced some variation (10 %) and hence was not enough to quantify the colour of the tissue. Generally, the system contributed to a more objective assessment of the colour in the wound images taken under clinical conditions.

A group at the University of Sao Paulo, Brazil developed algorithms to analyse different types of tissues in colour digital images of wounds utilizing one of the colour channels R, G, or B [16]. All images included in this study contained only two types of tissues, granulation and slough and hence only these two tissues were included in the analysis. The group developed some functions based on information obtained from the histogram of the Red Green and Blue channels of each type of tissue accordingly and were used to attribute membership grades (from 0-1) to each pixel referring to each type of tissue, granulation and slough. Each pixel in the original image that belongs to the wound region resulted in two pixels with two membership grades; one was for granulation tissue and the other one was for slough. The values of the membership grades of each pixel, in each channel, for each tissue was summed and normalised. The proportions of each type of tissue for each wound was then plotted to compare with the quantity of tissues observed by the clinicians in the images. This provided a quantitative measuring of the tissues in the leg ulcers.

The developed method addressed a major challenge that slough appeared covering the granulation tissue in most cases and sometimes mixed with it. Hence, it was improper to develop algorithms to separate them into two distinctive clusters. Instead, the method attributed membership grades to each pixel and assigned the pixel to the tissue type with the higher grade. However, this method was not sufficient as it only considered one colour channel and only two types of tissues were analysed.

2.9.2 RGB Histogram Distributions

For better segmentation of tissues, analysing the Red, Green and Blue frames separately is not adequate. Studies have shown that colour pixels should be considered in all three channels to be able to classify different wound tissues [17-19]. This is because wound tissues normally appear mixed with each other on the wound surface and hence the use of only one colour channel is not adequate to classify each type of tissue fully. Mekkes and Westerhof used large classifications tables of wound tissues and found that pixel clusters in RGB space for a given type of tissue formed an irregular shaped 3D cloud that distinguished the three types of necrotic, slough and granulation tissues [19]. Hence, in order to analyse the colour tissues of wounds thoroughly, information from all colour channels is needed.

Berris and Sangwine proposed a 3D RGB colour histogram clustering technique to automatically segment different types of tissues within the wound site in colour digital images of leg ulcers [17]. The images were cropped manually to include only the wound within the image. The proposed method scanned all the pixels within the wound region and computes the RGB coordinates of each pixel creating a 3D RGB histogram. The bins of this histogram corresponded to the Red Green and Blue coordinates computed from the original colour image. The computed 3D RGB histogram formed several colour clusters that corresponded to the different colour tissues on the wound site. After the 3D RGB histogram was computed, it was smoothened, eroded and dilated in order to form clusters that were more distinct. After that, the algorithm scanned the image again and segmented it according to each cluster formed in the 3D RGB histogram. This was done by comparing the RGB coordinates of each pixel in the original image with the RGB coordinates of the bins belonging to a specific cluster. The rest of the unmatched pixels were set to mid grey in the segmented image.

Using this process, several colour images were created, each representing one cluster. Each segmented image successfully separated the granulation tissue and slough from the surrounding skin. However, some pixels were incorrectly assigned to a cluster due to the lack of priory colour information about the different tissue types.

Moreover, the method was designed and tested successfully on only a few wound images and therefore a large data set is required to further enhance the algorithm.

Zheng *et al.* came up with a procedure for binary classification of wound tissues using three 2D Red, Green and Blue histogram distributions of pixels using colour images of venous leg ulcers [18]. The ulcers included in this study were carefully selected to ensure that the wound bed contained a combination of black necrosis, yellow slough, red granulation and pink epithelial tissues.

Several regions of interest (ROIs) were selected from each wound image using region growing. Each ROI represented one type of tissue and hence several ROIs could be required to sample a particular type of tissue within the same image. The R, G and B histograms were calculated from these ROIs for each type of tissue and used as features for classification [18]. These histograms were input to a Case-Based Reasoning (CBR) classifier as shown in Figure 2.17 which uses information from the histogram to classify different types of tissues. To determine the type of tissue of a specific ROI, the extracted Red Green and Blue histogram vectors were compared with the ones that existed in the database of the previously identified and classified cases of tissue types and the most K similar cases were retrieved from the database based on the Euclidean distance measure. The tissue was then classified based on the type of tissue found in the majority of the retrieved cases.

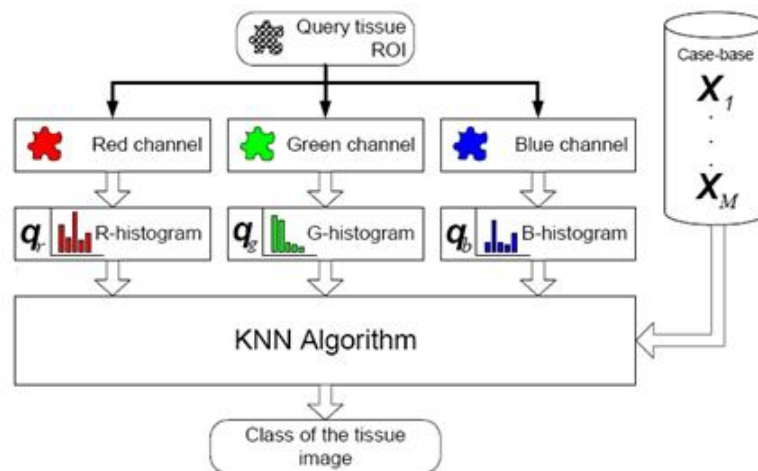


Figure 2.17: Schematic illustration of the CBR approach for tissue classification [18]

When comparing the classification accuracies obtained, it was noticed that using all of the channels for multi-class problems provided the best accuracies. Textural features were also included to improve the results of the classification [53]. Three textural features were selected as being the most significant ones: angular second moment, contrast feature and correlation feature. However, the accuracy of the results obtained from the classification based on textural features was lower than those obtained from the RGB feature based classification due to the small sizes of ROI (10x10 pixels) regions involved in the classification. Increasing the size of ROIs was not applicable in this case as it would have affected the accuracy by the risk of mixing two types of tissues within the same ROI.

2.9.3 Colour and Texture Descriptors

Most recently, as part of the EScarre Analyse Lisibilite' Evaluation (ESCALE) project dedicated to the design of a complete 3D and colour wound assessment tool, a segmentation-based classification of wound tissues was proposed [20], [21]. The ESCALE project aims to develop a complete automatic wound assessment system that incorporates a 3D model for wound dimension measurements as well as a robust colour tissue classification tool. The colour tissue classification tool utilizes the segmentation driven classification approach using Support Vector Machine (SVM) classifier [21].

A database that consists of several hundreds of digital colour images (3 Mpixels, 24 bits) of chronic wounds was obtained. To provide adequate reproducible lighting to compensate for different lighting conditions, a flashlight was used. Specifically, a ring flashlight with Evaluative-Through the Lens (E-TTL) control was used to avoid shadows and specular reflections. A small colour scale (Machbeth colour checker pattern) was placed near the wound when acquiring the images to correct for colour shifts. Acquisition and colour shift correction was performed in the RGB colour model. Since this model is highly sensitive to light conditions and corresponding colour shifts, it was necessary to provide reproducible ambient light and correct for colour shifts using the colour scale.

After acquiring the images database, the images were shown to a group of clinicians for labelling of tissues within the wound site as ground truth. Each clinician was provided with a pen tablet and a graphical user interface which allowed the clinician to sketch a contour around a specific tissue region and fill it with a specific colour according to the tissue colour code (red-granulation, yellow-slough, black-necrotic). The clinicians had no knowledge on the patients' medical history or wound treatment to ensure no external factors would affect the labelling. The ground truth was obtained using manual tracings rather than simple visual inspection because tests showed that tissue proportions using manual tracing exceeded visual inspection by more than 20% in most cases and hence visual inspection was discarded in this study. Two tracings, one month apart, were assessed by four clinicians to measure labelling stability and the difference between clinicians. Inter and intra observer variability was observed in this study especially for slough as it is difficult to trace, and it often appears mixed with granulation tissue in this study. The clinicians' tracings were merged to create a single ground truth labelling for each wound in order to evaluate the algorithm performance.

For better results, only the regions similarly labelled by six clinicians out of eight were considered. A database of a total 905 labelled regions was obtained: 302 granulation tissues, 243 slough tissues, 73 necrotic tissues and 287 healthy tissues.

First, the algorithm utilizes three selected unsupervised methods, J-SEG, Mean Shift and Colour Structure Code (CSC), were utilised to segment the wound images into different regions. The regions were labelled according to the tissue type mostly found across the segmented region and compared with the ground truth. Results showed that the segmentation results were more similar to the ground truth than the clinicians' tracings. This indicated that segmentation is an important step prior to classification. The J-SEG algorithm provided the best results to separate the regions with homogeneous colour and texture parameters [20] and was used in this study. Figure 2.18 shows the results of the unsupervised segmentation in this study.

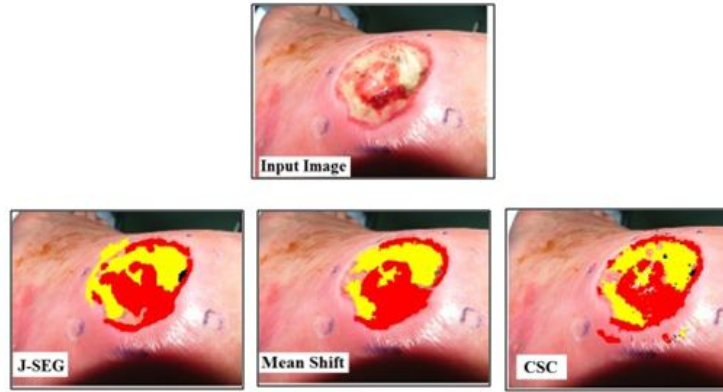


Figure 2.18: Segmentation results of the three unsupervised techniques used in ESCALE [21]

After that, an SVM classifier was utilised to obtain a supervised learning of the three types of tissues from the developed database of the tissue regions traced by the clinicians. The database tissue samples were divided into 40% (362 regions) for training and 60% (543 regions) for testing. Both colour and texture based descriptors (20 descriptors) are used to label each type of tissue during the learning phase. Then, the same descriptors were extracted from the segmented regions and were input to the SVM based classifier for automatic classification and labelling of these regions during the testing phase. The automatic segmentation driven classification was compared with the expert ground truth. The best results were obtained for the granulation tissue (75%) while moderate results were obtained for slough (60%) for the reason described above. Degraded results were obtained for the necrotic tissue as not enough samples of this tissue were included in the database. Results could be further improved with the addition of more samples in the database.

Colour has been utilized as the key element for analysis in colour image processing in the field of wound assessment for most of the work that has been developed so far. However, the interpretation of the colour content in the image has always been impaired because of the unavoidable differences in the acquisition conditions present when acquiring the images such as the type of camera used, the illumination in the room, and the type of flashlight used. These varying conditions alter the colour quality and scales in images which leads to inaccurate results which poses the main shortcoming of the analysis based on colour features and attributes.

Furthermore, colour-based analysis of ulcer tissues poses a major challenge when analysing regions of mixed tissues, especially regions where granulation tissue is mixed with slough tissue and cannot be identified accurately.

2.10 Ulcer Colour and Ulcer Healing

Human skin is a highly heterogeneous medium with a multi-layered structure. Various types of light-absorbing chemical compounds called chromophores or pigments such as melanin, haemoglobin, bilirubin and b-carotene exist in this media with melanin and haemoglobin being dominantly contained in the epidermal and dermal layer, respectively [54]. Melanin is produced by cells called melanocytes in the epidermis layer of the skin. Haemoglobin is present within the red blood cells in the blood vessels found in the dermis. Two other pigments are found in the dermis, bilirubin and b-carotene, which give the skin its yellowish or olive tone.

When light is focused on the skin, around 4-7% of it is reflected back due to the change in the refractive index between air and skin. The remaining 96-93% of the light gets transmitted into the skin following a complex path where it interacts with the different structures and chromophores and gets remitted back from the skin [22]. These interactions (mainly absorption and scattering) are responsible for changing the spectral composition of the light that represents the optical properties of the skin structures and chromophores. The remitted light is captured by the human eye producing colour vision and can be registered with the camera producing colour digital images. Hence, an understanding of the colour image formation would reveal diagnostically important facts about the internal structure and composition of the skin ulcers [23].

One of the major changes during ulcer healing is the colour of the tissues. Ulcers change colour gradually from black to yellow to red as they heal as explained in section 2.7.2. Colour is the perceptual sensations of light appearing upon the retina in the visible region of the spectrum, which extends from violet at about 380 nm to red at about 750 nm as shown in Figure 2.19. Different colour modules reveal different

reflectance ranges within the visible spectrum. The red colour exists at the wavelengths between 620-740 nm in visible spectrum.

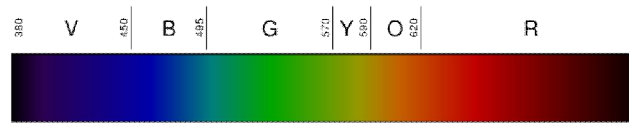


Figure 2.19: Reflectance Spectrum of the Visible Light

From the wound healing process explained in section 2.4 and the wound tissue analysis given in section 2.7.2, it is evident that the first indication of ulcer healing is the growth of the healthy red granulation tissue. Granulation tissue contains small blood capillaries (small arteries and veins) mixed with the collagen based extracellular matrix. One of the main skin chromophores, pigment haemoglobin exists in the red blood the cells in the blood vessels. It binds with oxygen and carries it from the lungs to the cells through the arteries. It also binds with carbon dioxide and carries it back to the lungs through the veins. The absorption spectra of oxy-haemoglobin (haemoglobin bounded with oxygen) and deoxy-haemoglobin (haemoglobin not bounded with oxygen) are shown in Figure 2.20 [22]. The figure shows that both oxy- and deoxy-haemoglobin exhibits the maximum absorption at the short and middle wavelength ranges of the visible spectrum (around 420-430 nm) while both of them exhibit reflection (total absorption) at wavelengths above 600nm.

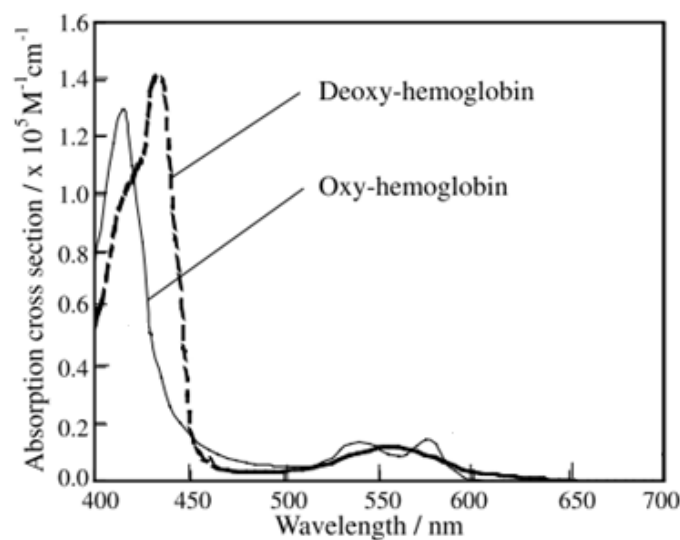


Figure 2.20: Absorption spectra of oxy-haemoglobin and deoxy-haemoglobin [22]

The granulation tissue that contains the haemoglobin pigment is seen as red when viewed under visible light; this is explained by the fact that the haemoglobin pigment (whether deoxy-haemoglobin or oxy-haemoglobin) gives off a reflection at 600nm and higher [24]. The optical characters of pigment haemoglobin can be studied and recognized in colour images and used to show their content within the human skin [25], [26]. Hence, this study focuses on analysing the optical characteristics of pigment haemoglobin and determining its content on ulcers surface in colour images of chronic ulcers. Due to the fact that the haemoglobin pigment causes the red colour of granulation tissue, it is hypothesized that images due to haemoglobin could be extracted from colour images of chronic ulcers. Images caused by the haemoglobin are particularly significant because areas of the haemoglobin distribution on the ulcer surface are clearly shown; this leads to the indication of the areas with granulation tissue. Identifying and quantifying the amount of granulation tissue on ulcer surface gives an indication of the healing progression and effectiveness of treatment.

2.11 Summary

Ulcers are chronic wounds that fail to heal within a specified period of time due to underlying aetiologies or improper wound care and management [1]. They cause severe pain and discomfort to the patients and put them at the risk of limb amputation. Leg ulcers often occur at the lower limb and account for 98% of all lower limb wounds [34]. According to the aetiologies that cause them, ulcers are divided into three main types: vascular ulcers (venous ulcers and arterial ulcers), pressure ulcers and diabetic ulcers. The prevalence increases with increasing age and underlying aetiologies.

Ulcer care and management aims to illuminate any underlying factors that may impair healing and provide a healthy wound environment that promotes healing. It focuses on cleaning the ulcer from any damaged tissues and cellular debris, treating any bacterial infections and selecting the appropriate dressings. Ulcer care and management should include an ongoing evaluation of the physiological changes of the ulcer throughout the course of the treatment to monitor the ulcer for complications.

One of the most prominent changes during ulcer healing is the colour of the tissues on the ulcer surface [10]. Ulcers can initially appear covered with layers of unhealthy black necrosis and yellow slough. As ulcers heal, healthy red granulation tissue starts to grow from the ulcer base gradually replacing the unhealthy tissue and filling the ulcer cavity. Identifying and classifying different tissues on ulcer surface is very crucial for ulcer healing assessment. In clinical practice, the ulcer surface is evaluated based on a simple visual inspection which is subjective and lacks precision and consistency. The monitoring of ulcers requires an objective, precisely quantitative and reproducible assessment. The digital image analysis has been employed to detect and classify ulcer tissues to provide an accurate objective assessment of wound healing. Most of the work developed in the field of wound assessment via digital imaging utilised colour as the main component for analysis. However, colour-based analysis is always compromised by the unavoidable differences in the acquisition conditions that affect the colour quality and leads to inaccurate results. Furthermore, colour-based analysis of ulcer tissues poses a major challenge when analysing regions of mixed tissues, especially regions where granulation tissue is mixed with slough tissue and cannot be identified accurately.

Colour vision is the result of light interaction with colour objects. Light reflected from the ulcer carries valuable information on the internal structure and properties of the ulcer's surface. Hence, an understanding of the colour image formation would reveal diagnostically important facts about the internal structure and composition of the skin ulcers. Ulcer healing is indicated by the growth of the granulation tissue which appears red in colour due to the pigment haemoglobin content in the newly built blood capillaries [24]. Therefore, it is hypothesized that images due to haemoglobin could be extracted from colour images of chronic ulcers. These images represent regions of haemoglobin distribution on the ulcer surface, which in turn reflects regions of granulation tissue on ulcers surface as an indication of healing progression. This approach is fundamentally unique in a way that it does not focus on colour image features or attributes directly like previous works in this field, instead it draws an understanding of the tissue histology utilising physics-based interpretation of image colours.

CHAPTER 3

DIGITAL IMAGING AND DATA ANALYSIS TECHNIQUES

3.1 Introduction

This chapter explores the concept of colour vision and the formation of digital colour images. It also investigates some of the important image processing and data analysis techniques that are utilised in this research work. Section 3.2 explains human perception of colours and acquisition of digital colour images using digital cameras. It also elaborates the concept of colour consistency and colour shift correction. Sections 3.3, 3.4 and 3.5 explore important statistical data analysis techniques which are principal component analysis, independent component analysis and fastICA respectively. An unsupervised machine learning and data classification technique namely fuzzy c-means clustering is presented in section 3.6. Thresholding-based segmentation employing Otsu's thresholding technique is elaborated in section 3.7. Finally, a summary of the chapter is given in section 3.8.

3.2 Colour Vision and Formation of Digital Colour Images

Colour vision is the ability to distinguish objects based on the wavelength of the light reflected, emitted or transmitted from/through them. The human visual system has the ability to perceive a variety of colours depending on the optical properties of the objects and the light reflected upon them.

3.2.1 The Perception of Colours

Colour perception is a complex process whereby the brain responds to the stimuli that are produced when the incoming light reacts with the cone cells in the retina. There are three main types of cone cells that are sensitive to three different spectra spaced through the visible spectrum [55]. They are labelled according to the order of the wavelengths of their spectral sensitivities peaks, short (S), medium (M) and long (L) as shown in Figure 3.1. These cells interact with the incoming light and send output signals to the visual cortex of the brain which processes these signals and perceives a wide range of colours.

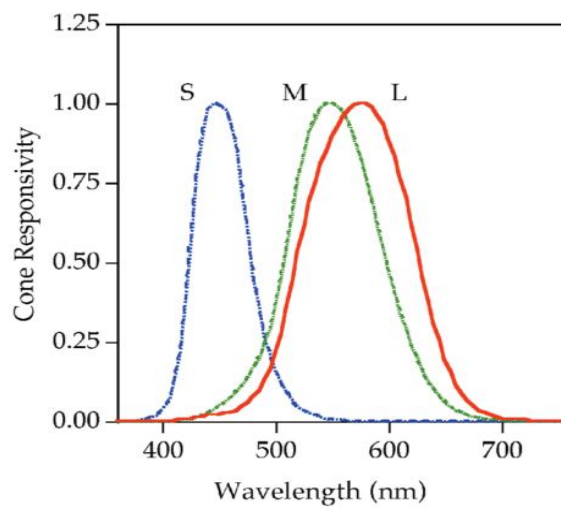


Figure 3.1: Spectral responsiveness of L, M and S cones [55]

White light (flashlight used in photography) represents a mixture of all the wavelengths in the visible range of the electromagnetic spectrum between approximately 400nm-700nm. If white light is allowed to pass through a prism, it will spread out and appear to consist of six main colours; violet, blue, green, yellow, orange and red as shown in Figure 3.2.

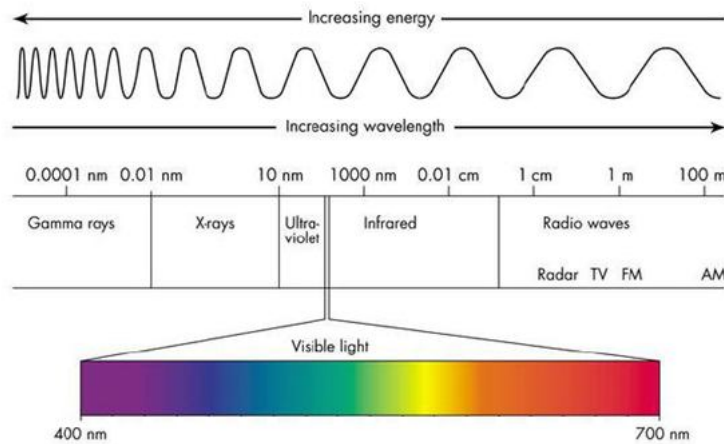


Figure 3.2: A schematic diagram of the electromagnetic spectrum indicating the visible light spectrum extending from 400nm-700nm

A plot of the relative energy of light at each wavelength creates a power distribution curve quantifying the spectral characteristics of the light source. White light has a uniform light emission throughout the visible spectrum. Hence, an object viewed under white light will be viewed with its real colour.

The colour perceived is the result of the interaction of three main components; light source, object and the observer as shown in Figure 3.3. When light is shed upon a red object for example, it reflects back with a modified spectrum. The reflected light incorporates the optical properties of both the light source and the object having wavelengths in the red colour range of the visible spectrum (red light). The reflected light then enters the retina in the eye where it interacts with the cone cells, which send signals to the visual cortex of the brain that interprets the colour of the object as red.

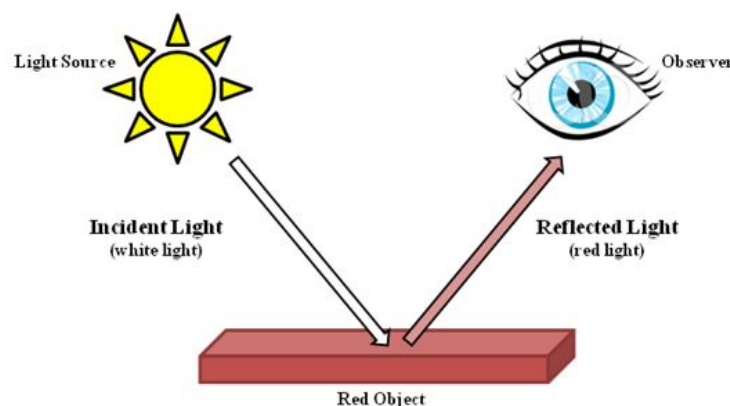


Figure 3.3: Perception of colour

3.2.2 Digital Camera and RGB Colour Images

A digital camera is a device that is used to acquire either video or still photographs by recording images through an electromagnetic sensor. Digital single-lens reflex (DSLRs) digital cameras have a unique viewing system in which a mirror reflects lights from the lens through a separate optical viewer. When acquiring images, the mirror flips out of the way allowing light to fall onto the sensor.

Most digital cameras use a Charge-Coupled Device (CCD) as a sensor device to acquire the image. A CCD is an integrated circuit which contains an array of coupled, light sensitive capacitors [56]. In a CCD, the electrical field at different parts of the surface is controlled by an array electrode called the gates. The surface of the CCD is further broken down into smaller regions called pixels, or picture elements. CCD has better quantum efficiency than photographic film and generally responds to 70%-90% of the incident light [56].

When incoming light meets with the CCD, electric charges are generated due to the photoelectric effect. These charges are collected in the electrodes (gates). Each electrode then transfers its electric charge to one or other of its neighbours under the control of an external circuit. Finally, the individual charge packets are converted to an output voltage and digitally encoded to create a digital image [56].

A digital colour camera usually uses a Bayer mask over the CCD to generate a digital colour image. Bayer mask is a colour filter array with Red, Green and Blue (RGB) colour filters arranged on a square grid of CCD sensor [57]. The mask pattern is 50% green, 25% red and 25% blue as shown in Figure 3.4. There are twice as many green elements as red or blue in order to mimic the human vision that is more sensitive to the green colour (luminance-sensitive element) than red and blue (chromatic-sensitive elements). The sensor elements sample values sensed by this filter on the CCD then gets interpolated to create colour image pixels.

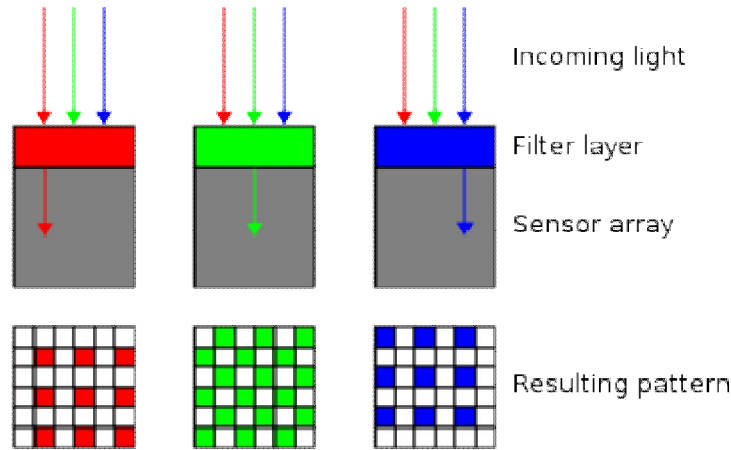


Figure 3.4: The Bayer filter pattern on the CCD profile

3.2.3 RGB Colour Model Representation

As it has been explained in the previous section, most digital cameras utilise the spectral distribution of the primary colours Red, Green and Blue to produce RGB colour images. The RGB colour model is a device-dependent additive colour model in which red, green and blue are added together to produce a broad variety of colours or what is called an RGB colour cube shown in Figure 3.5. The three primary colours red, green and blue (RGB) can be treated as a 3D colour space that contains all the possible colours to mix from the RGB.

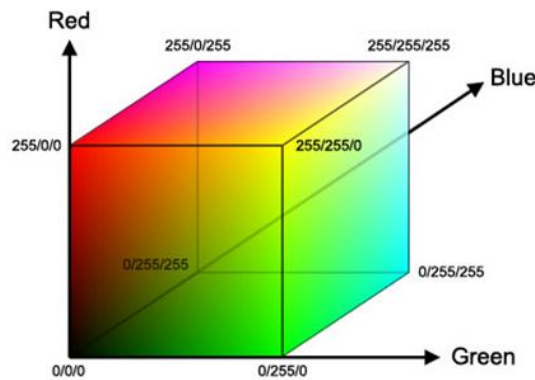


Figure 3.5: The RGB colour cube

RGB colour model is ideal for sensation, representation and displaying of colour images in electronic systems because it corresponds to human visual system colour

model. In the RGB colour space, zero intensity of each primary colour produces black while full intensity of each gives white. The quality of this white light depends on the nature of the primary light sources. If they are properly balanced, the result is a neutral white.

An RGB digital colour image is formed from a concatenation of the three spectral bands Red, Green and Blue. They represent three separate grey-level images that can be extracted from the RGB colour image as shown in Figure 3.6.

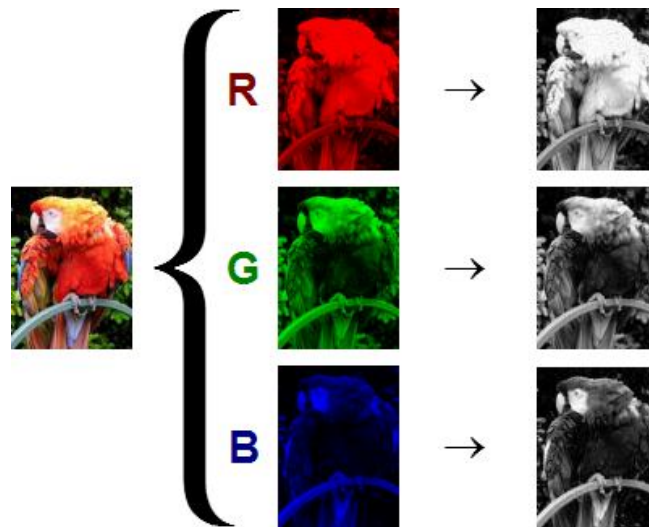


Figure 3.6: Red, Green and Blue grey-level images of a digital colour image

3.2.4 Colour Constancy and Colour Shift Correction

Human visual system has the ability to perceive the correct colour of the surrounding objects even under different illumination. This phenomenon is known as "colour constancy". Digital cameras and other devices on the other hand do not have this ability and normally produce images with incorrect colours of objects when photographed under different illuminations.

The output from the digital camera is affected by the spectrum of the incident light and the object's surface reflectance. If the intensity value of one pixel is taken at location (x,y) in the image, its value is obtained as:

$$f_c(x, y) = \int E(\lambda)S(x, y, \lambda)C_c(\lambda) \quad (3.1)$$

where $c = [R, G, B]$, $C_c(\lambda)$ is the spectral sensitivity of the camera's sensor, $E(\lambda)$ is the spectrum of the incident illumination, and $S(x, y, \lambda)$ is the spectral reflectance of the surface [58]. The spectrum of the incident illumination depends on the type of the light source used in the acquisition. Assuming white light is used, the spectrum of white illumination is evenly distributed across all wavelengths and colours can be rendered correctly under this illumination. If the spectrum of the incident white illumination is altered due to varying ambient light conditions, the perceived colour of the object will not be realistic.

Colour imaging is employed in many applications such as object identification and medical diagnosis of skin lesions in which accurate colour rendition is critical. Hence, it is important to correct any colour shifts in the acquired colour images before processing. Colour correction, often referred to as "white balance", is an image processing technique whereby unrealistic colour casts caused by inadequate acquisition condition (in particular lighting conditions) are removed from digital images resulting in corrected colour images. The main goal for colour shift correction is to compensate for the change in the spectrum of the incident light in relation to the actual illumination used in the acquisition [58]. Most digital colour cameras have the "white balance adjustment" feature, where the levels of red and blue are fitted to the green level either from a camera specific mode or when pointing the camera at a white surface. The White Balance can also be set to factory pre-set values, often given in a colour temperature. However, colour casts can still be produced due to the avoidable variations in the ambient light during image acquisition.

Most of the developed techniques for colour shift correction are based on assumptions about the statistical properties of the illumination source used in the photography and surface reflectance [59]. They generally involve two phases. First, the illumination source parameters are estimated from the image. Then the image colours are corrected based on this estimate [60]. Figure 3.7 shows the effect of varying illumination on the perceived colours of objects. Figure 3.7 (a) shows an

image of a room photographed by two light sources; the tungsten lamp and the daylight from the window. The yellow cast caused by the light from the tungsten lamp makes the objects in the room appear with colours that differ from their original ones. Figure 3.7 (b) shows the same image after colour correction has been applied resulting in correct rendering of the objects colours.



(a) Image before colour correction

(b) Image after colour correction

Figure 3.7: Effects of varying illumination on the perceived colours of objects

3.3 Principal Component Analysis

Principal Components Analysis (PCA) is a mathematical technique that utilises an orthogonal linear transformation to convert a dataset of observations into a new dataset of uncorrelated variables called the principal components. The main idea behind PCA is to obtain a new dataset of principal components so that most of the variance (hence signal energy) in the original dataset is retained in the first few principal components ordered from greatest variance in the first principal component, second greatest variance in the second principal component, and so on [61]. The main goal of PCA is to identify the most meaningful basis to re-express complex multidimensional datasets as simple lower dimensions datasets to filter out noise and extract useful hidden information underlying within the original datasets [62]. This linear transformation is applied in multivariate data analysis of many fields such as neuroscience, computer graphics and image data compression [63]. In the following subsections, the theories behind the formulation of the PCA as well as estimating the principal components are elaborated.

3.3.1 Eigenvalues and Eigenvectors

Consider a square matrix A of size $(k \times k)$. If there are a scalar λ and a vector γ that fulfil the following relation:

$$A\gamma = \lambda\gamma \quad (3.2)$$

then λ is an eigenvalue of the matrix A if it satisfies the k -th order polynomial equation:

$$|A - \lambda I| = 0 \quad (3.3)$$

where I is an identity matrix.

There are up to k eigenvalues of the matrix A that can be found by solving Equation (3.3). For each eigenvalue λ , there exists corresponding eigenvector γ that can be obtained by solving Equation (3.2) [64].

3.3.2 Covariance Matrix

Covariance matrix is a square matrix of co-variance values that measure the degree of the relationship between variables in the datasets. A large positive co-variance value indicates strongly correlated data while a large negative value denotes strongly uncorrelated data. The covariance between two equal X and Y is found as:

$$COV(X, Y) = \frac{\sum_{i=1}^n (X_i - \bar{X})(Y_i - \bar{Y})}{(n-1)} \quad (3.4)$$

where \bar{X} and \bar{Y} are the means of vectors X and Y respectively, and n is the number of elements in the vectors. Note that $COV(X, Y) = COV(Y, X)$.

Assuming a dataset of three vectors X , Y and Z , the corresponding (3×3) square matrix C_{XYZ} is found as follows:

$$C_{XYZ} = \begin{bmatrix} COV(X, X) & COV(Y, X) & COV(X, Z) \\ COV(Y, X) & COV(Y, Y) & COV(Y, Z) \\ COV(Z, X) & COV(Z, Y) & COV(Z, Z) \end{bmatrix} \quad (3.5)$$

Covariance matrix C_{XYZ} is a square matrix that is symmetrical along the main diagonal. The diagonal values of C_{XYZ} represent the covariance between one of the dimensions and itself. The off-diagonal values represent the covariance between the vectors [63].

The covariance matrix provides the advantage of easily inferring statistical information about the variables in the dataset and the relationship among them given that they are measured in the same unit [61]. Hence, the covariance matrix is employed to estimate the principal components of the observed dataset.

3.3.3 Standardized Linear Combination

The main objective of PCA is to find suitable basis to re-express a given dataset as a linear combination of these basis vectors for the purpose of either dimension reduction or extraction of useful hidden information from the dataset. Hence, the problem of finding these basis vectors is simplified by confining these vectors to this linear combination [64].

Given a dataset A , there exists a weighted average expressed as:

$$\left[\delta^T A = \sum_{j=1}^n \delta_j A_j \right] \quad (3.6)$$

where n denotes number of elements in the dataset, δ denotes the weighting vectors. The aim is to maximize the variance of $\delta^T A$ by choosing δ according to the condition $\max_{\{\|\delta\|=1\}} Var(\delta^T A) = \max_{\{\|\delta\|=1\}} \delta^T Var(A) \delta$ which occurs when δ is selected as the eigenvector γ corresponding to the largest eigenvalue, λ of the covariance matrix C_A [64]. The resultant weighted vector is a projection of A into the one-

dimensional space, weighted by the elements of the eigenvector, γ , which is referred to as the first principal component. The second principle component can be found by selecting δ as the eigenvector corresponding to the second largest eigenvalue and so on.

3.3.4 Estimation of Principle Components

To find the principal components of a dataset; an image for example, the mean value is initially subtracted from each of image spectral bands Red, Green and Blue to obtain a zero mean variable data as follows:

$$\begin{aligned} R &= R_0 - \mu_{R_0} \\ G &= G_0 - \mu_{G_0} \\ B &= B_0 - \mu_{B_0} \end{aligned} \tag{3.7}$$

where R_0 , G_0 and B_0 denote image spectral bands before subtraction and μ_{R_0} , μ_{G_0} and μ_{B_0} denote the mean value of image spectral bands.

The covariance matrix is then computed for the three spectral bands of the image. The covariance matrix of an image in RGB form is defined as follows:

$$C_{RGB} = \begin{bmatrix} COV_{RR} & COV_{GR} & COV_{BR} \\ COV_{RG} & COV_{GG} & COV_{BG} \\ COV_{RB} & COV_{GB} & COV_{BB} \end{bmatrix} \tag{3.8}$$

where COV_{xx} is calculated using Equation (3.4).

The eigenvectors are then determined from the covariance matrix by solving the following equation:

$$C_{RGB} = \gamma \lambda \gamma^T \tag{3.9}$$

where λ is a diagonal matrix representing eigenvalues of covariance matrix C_{RGB} and γ is a matrix of eigenvectors of covariance matrix arranged as columns.

The eigenvectors are used as linear transformation of original Red, Green and Blue values. It is reported that the resulting vectors have uncorrelated components, or in other words, the primary axis of the data has been aligned where the variance is maximal [65]. The vectors in new space $[X_1 \ X_2 \ X_3]^T$ are obtained by:

$$\begin{bmatrix} X_1 \\ X_2 \\ X_3 \end{bmatrix} = \begin{bmatrix} \gamma_{11} & \gamma_{12} & \gamma_{13} \\ \gamma_{21} & \gamma_{22} & \gamma_{23} \\ \gamma_{31} & \gamma_{32} & \gamma_{33} \end{bmatrix} \begin{bmatrix} R \\ G \\ B \end{bmatrix} \quad (3.10)$$

where $\begin{bmatrix} \gamma_{11} & \gamma_{12} & \gamma_{13} \\ \gamma_{21} & \gamma_{22} & \gamma_{23} \\ \gamma_{31} & \gamma_{32} & \gamma_{33} \end{bmatrix}$ are the eigenvectors of the covariance matrix.

3.4 Independent Component Analysis

Many observations of physical systems are produced by a linear combination of underlying sources. Independent Component Analysis (ICA) is a multivariate data analysis technique used to recover source signals from observed linear combinations of them. The term "independent" implies that the recovery depends on the assumption that the sources are mutually independent [66]. ICA is the most widely applied solution to the problem of Blind Source Separation (BSS) where the sources of observed signals are mixed and unknown [66], [67].

3.4.1 Linear Mixing Model

Consider M source signals in vector form, $s(t) = [s_1(t), s_2(t), s_3(t), \dots, s_M(t)]^T$, the N observations, $x(t) = [x_1(t), x_2(t), x_3(t), \dots, x_N(t)]^T$, are generated by a mixture; often corrupted by additive observational or sensor noise $n(t)$; as follows:

$$x(t) = f(s(t)) + n(t) \quad (3.11)$$

The goal of blind source separation is to invert the function f and recover the sources. The term "blind" implies that the source signals and the way they were

mixed are unknown [68]. The mixing function f , the noise n , and the sources s are unknown and must be estimated. ICA makes the assumption that the sources are linearly mixed by a mixing matrix A [67]. Thus, observations are assumed to be generated by:

$$x(t) = A(s(t)) + n(t) \quad (3.12)$$

Although the function f has been replaced with an unknown square matrix A , the problem of identifying the sources s is still under-determined, because there are $N + M$ unknown signals of the sources and the noises, with N known signals (the observations). Furthermore, assumptions about the characteristics of the noise and the source densities lead to a range of ICA models. However, the majority of ICA models are noiseless [67]. Hence, the linear mixing model of ICA can be written as:

$$x = As \quad (3.13)$$

The aim of ICA is to recover the original sources from the observations alone. In ICA, the sources are assumed independent such that each source signal is generated by a process unrelated to the other sources [67]. The concept of independence is explained in the next section. The ICA model therefore seeks a separating matrix W which when applied to the observations, recovers estimated sources u as:

$$u = Wx \quad (3.14)$$

The ICA model is illustrated in Figure 3.8. The signals $s = [s_1, s_2, s_3, \dots, s_n]$ are mixed using elements from the mixing matrix A to create a set of observations $x = [x_1, x_2, x_3, \dots, x_n]$ according to Equation (3.13). Independent source signals $u = [u_1, u_2, u_3, \dots, u_n]$ are then estimated from the observation set using the separating matrix W according to Equation (3.14).

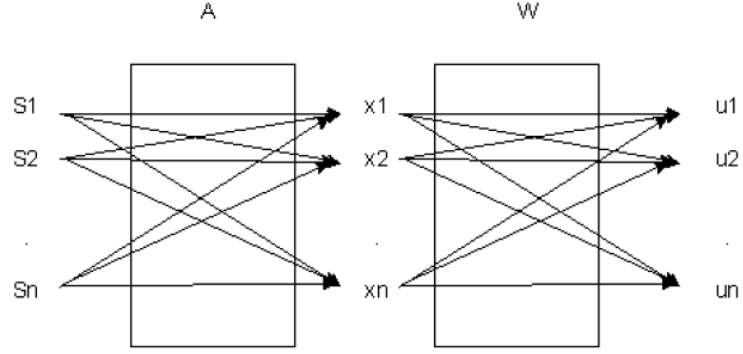


Figure 3.8: Basic model of Independent Component Analysis (ICA) [68]

3.4.2 Definition of Independence

In ICA models, the sources are assumed to be statistically independent [66], [67]. The statistical independence means that the joint probability density function of the original sources can be written as the product of marginal independent distributions described as $p(s) = \prod_{i=1}^M p_i(s_i)$. If the probability density function of the estimated sources is also the product of its marginal distributions, then the estimated sources are independent and the separation has been achieved [67].

The definition of independence comes from information theory. The independence between the sources is measured by the amount of mutual information they contain, which is defined in terms of entropies [67]. Let X and Y , be random variables, the (differential) entropy of X is defined as:

$$H(X) = H[p(x)] \stackrel{def}{=} - \int p(x) \log p(x) dx \quad (3.15)$$

The joint entropy X, Y is:

$$H(X, Y) = - \sum_x \sum_y P(x, y) \log_2 [P(x, y)] \quad (3.16)$$

where x and y are particular values of X and Y respectively, and $P(x, y)$ is the probability of these values occurring together.

The conditional entropy of X given Y is given as:

$$H(X | Y) = H(Y) - H(Y, X) \quad (3.17)$$

Finally, the mutual information between X and Y is:

$$I(X; Y) = H(X) + H(Y) - H(X | Y) \quad (3.18)$$

The mutual information measures the average amount of information that X conveys about Y or vice versa. It will always be positive and will only equal zero when the components are independent [67]. Hence, the problem of ICA is formulated as to minimize the mutual information between source signals [69].

3.5 FastICA

FastICA is an ICA technique developed by Aapo Hyvärinen [66], [69-71]. In this method, the independent components are found as projections that maximize non-Gaussianity. The following subsections describe the principles and processes involved in estimating the independent source components using FastICA.

3.5.1 Whitening

The aim of ICA is to find a linear transformation W of the observed signals x that makes the output u as independent as possible. However, due to the complexities of ICA algorithms, it is important to pre-process the observed signal x to simplify the estimation of the transformation W [70].

The input data is pre-processed using whitening. One popular method for whitening is to use principle component analysis (PCA) [70]. As explained in section 3.3.4, PCA utilises the eigenvalue decomposition of the covariance matrix $\tilde{x}\tilde{x}^T = \gamma\lambda\gamma^T$ where γ is the orthogonal matrix of eigenvectors of $\tilde{x}\tilde{x}^T$ and λ is the diagonal matrix of its eigenvalues. Whitening can be performed as follows:

$$\tilde{x} = \gamma \lambda^{-\frac{1}{2}} \gamma^T x \quad (3.19)$$

where the matrix $\lambda^{-\frac{1}{2}}$ is computed as $\lambda^{-\frac{1}{2}} = \text{diag}(\lambda_1^{-\frac{1}{2}}, \dots, \lambda_n^{-\frac{1}{2}})$. Subsequently, whitening transforms the mixing matrix A into a new one \tilde{A} such that:

$$\tilde{x} = \gamma \lambda^{-\frac{1}{2}} \gamma^T x = \gamma \lambda^{-\frac{1}{2}} \gamma^T A s = \tilde{A} s \quad (3.20)$$

Whitening transforms the signals x linearly to the new vector \tilde{x} whose components are uncorrelated and their variances equal unity [70]. In this case, the covariance matrix of \tilde{x} equals the identity matrix, $E\{\tilde{x}\tilde{x}^T\} = I$.

3.5.2 Basic Principle of ICA Estimation in FastICA

The basic intuitive of ICA comes from Central Limit Theory which states that the distribution of a sum of random independent variables tends to be a Gaussian distribution (normal density function) under the condition that the variables are defined under the same probability space and share the same probability distribution and are independent [66].

Given whitened dataset \tilde{x} that is distributed according to the ICA model as $\tilde{x} = \tilde{A} s$, estimating the independent components s can be accomplished by finding the appropriate linear combinations of the mixture variables. Thus, to estimate one of the independent components, it is possible to consider a linear combination of \tilde{x}_i that can be expressed as follows:

$$a = w^T \tilde{x} = \sum_i w_i \tilde{x}_i \quad (3.21)$$

where w is a vector to be determined.

If w is one of the rows of the inverse \tilde{A} , this linear combination would actually equal to one of the independent component [66]. By defining $z = \tilde{A}^T w$, Equation (3.21) can be re-written as:

$$a = w^T \tilde{x} = w^T \tilde{A}s = z^T s \quad (3.22)$$

Central Limit Theory ensures that the sum of original variables, $z^T s$ is more Gaussian than any of the independent components s_i and become least Gaussian when it equals to one of them. Therefore, taking w as a vector that maximizes the non-Gaussianity of $w^T \tilde{x}$, this vector will correspond to a z which has only one nonzero component [66], [68]. In this case, $w^T \tilde{A}s = z^T s$ equals to one of the independent components.

3.5.3 Measures of Non-Gaussianity

According to information theory, a Gaussian variable has the largest entropy among all variables of equal variance. Entropy is interpreted as the degree of information that the variable gives. Negentropy, or negative entropy, measures the difference of entropy between a Gaussian variable and a given variable. Hence, negentropy can be used as a measure for non-Gaussianity.

Negentropy J is defined as:

$$J(x) = H(x_{\text{gaussian}}) - H(x) \quad (3.23)$$

where x_{gaussian} is a Gaussian random variable of the same covariance matrix as x . Negentropy is always non-negative, and it is zero if and only if x has a Gaussian distribution [66].

Using negentropy, as a measure of non-Gaussianity is well justified by statistical theory. However, computing negentropy using Equation (3.23) is very difficult. Hence, a simplified approximation of negentropy is used.

3.5.4 Approximation of Negentropy

General non-quadratic functions to generalize the higher order cumulant are proposed to approximate negentropy [72]. In general, the approximation of negentropy $J(x)$ can be written as:

$$J(x) \approx k_1 (E(\{G^1(x)\}))^2 + k_2 (E(\{G^2(x)\}) - E\{G^2(v)\})^2 \quad (3.24)$$

where G^1 and G^2 are odd and even non-quadratic functions respectively, k_1 and k_2 are positive constants, and v is a Gaussian variable of zero mean and unit variance. The variable x is assumed to have zero mean and unit variance. Roberts and Everson pointed out that this approximation is not very accurate. However, it can be used to construct a consistent measure of non-Gaussianity in a sense that it is always non-negative and equals zero if x has a Gaussian distribution [67]. If only one non-quadratic function G is used, Equation (3.24) becomes:

$$|J(x) \propto [E\{G(x)\} - E\{G(v)\}]^2| \quad (3.25)$$

The performance of the approximation of negentropy shown in Equation (3.25) depends on the non-quadratic function G . Choosing G that does not grow so fast, one obtains robust estimation of negentropy [69]. Generally, the following choices of G have been proven useful:

$$G_1(u) = \tanh(a_1 u) \quad (3.26)$$

$$G_2(u) = u \exp(-u^2 / 2) \quad (3.27)$$

$$G_3(u) = u^3 \quad (3.28)$$

where $1 \leq a_1 \leq 2$ is some suitable constant [69].

3.5.5 Fixed Point Algorithm

Fast ICA is based on fixed-point iteration scheme for finding a maximum of the non-Gaussianity of $w^T \tilde{x}$. The maxima of the non-Gaussianity of $w^T \tilde{x}$ are obtained at

certain optima of $E\{G(w^T \tilde{x})\}$. The optima of $E\{G(w^T \tilde{x})\}$ under the constraint $\|w\|^2 = 1$ are obtained at points where:

$$E\{\tilde{x}G(w^T \tilde{x})\} + \beta w = 0 \quad (3.29)$$

where β is some constant.

Newton's method is implemented to solve Equation (3.29). Denoting the term on the left side by F , we obtain its Jacobian matrix, $JF(w)$ as:

$$JF(w) = E\{\tilde{x}\tilde{x}^T G'(w^T \tilde{x})\} + \beta I \quad (3.30)$$

To simplify the inversion of the matrix, the first term of Equation (3.30) is estimated first. Since the data is whitened, the approximation can be written as:

$$E\{\tilde{x}\tilde{x}^T G'(w^T \tilde{x})\} \approx E\{\tilde{x}\tilde{x}^T\} E\{G'(w^T \tilde{x})\} = E\{G'(w^T \tilde{x})\} I \quad (3.31)$$

Thus the Jacobian matrix becomes diagonal, and can be inverted. From Equation (3.29), the approximation of Newton's iteration becomes:

$$w \leftarrow w - \frac{[E\{\tilde{x}G(w^T \tilde{x})\} + \beta \tilde{x}]}{E\{G'(w^T \tilde{x})\} + \beta} \quad (3.32)$$

which can be simplified to give the following basic fixed-point iteration:

$$w \leftarrow E\{\tilde{x}G(w^T \tilde{x})\} - E\{G'(w^T \tilde{x})w\} \quad (3.33)$$

3.5.6 Estimation of Independent Components

Given a dataset x that constitutes of linear mixtures of independent source signals, these steps should be followed to estimate the independent sources employing the FastICA algorithms:

1. Pre-process the input dataset, x , and transform it into the whitened dataset \tilde{x} .
2. Initialize the weight vector w of unit norm.
3. Let $w \leftarrow E\{\tilde{x}G(w^T \tilde{x})\} - E\{G'(w^T \tilde{x})w\}$, where G is chosen to be one of the functions defined in Equations (3.26), (3.27) and (3.28).

4. Divide w by its norm $w \leftarrow \frac{w}{\|w\|}$.
5. Repeat the two previous steps until convergence criterion is met

Convergence means that the old and new values of w point in the same direction (their dot product is almost equal to 1). This implies that either vectors w or $-w$ could be estimated and both would define the same direction.

3.6 Machine Learning and Clustering-Based Classification

Machine learning is divided into two approaches: supervised learning and unsupervised learning. In supervised learning, labels are assigned to the datasets to be learned so that when new data arrive, they can be classified according to the labels learned [73]. Unsupervised learning on the other hand does not assign any labels to the data. Instead, it tries to find a suitable natural representation of the underlying distribution or characteristics of the data [73], [74]. Clustering is an unsupervised data classification technique that has been used by many applications in pattern recognition and data classification.

3.6.1 Clustering

Clustering is a common technique of unsupervised learning and classification where elements of a dataset are partitioned into several disjoint groups (clusters) so that points in one group are similar to each other and are as different as possible from points in other groups [74]. This is done through selection of a suitable proximity measure that groups similar data together. The choice of an appropriate proximity measure depends on the nature of the data and directly affects the performance of the clustering algorithm.

Clustering can be classified into hard clustering and fuzzy clustering based on membership of each data. A hard clustering algorithm divides data into distinct clusters, where each data element belongs to exactly one cluster. In fuzzy clustering, data elements can belong to more than one cluster and defined by belonging

probabilities or membership degrees [74]. A fuzzy clustering becomes a hard clustering when each data element is assigned to the cluster with the largest membership level.

3.6.2 Fuzzy C-means Clustering

The simplest and most commonly used soft clustering algorithm is fuzzy c-means clustering. In fuzzy c-means, each point in the dataset is assigned membership grades to each of k number of clusters based on a similarity measure, usually the Euclidean distance, between the point and the cluster centre [75]. The fuzzy c-means aims to optimize an objective function J_m via an iterative process. The objective function J_m is defined by the Euclidean distance between data points and the cluster centres:

$$J_m = \sum_{i=1}^n \sum_{j=1}^c u_{ij}^m \|x_i - v_j\|^2 \quad (3.34)$$

where m is any real number greater than 1 chosen to adjust the merge of the clusters [76], u_{ij} is the degree of membership of data point x_i in the cluster c_j and v_j is the j^{th} class centre. This function is a generalized form of least-squares objective function often used in unsupervised machine learning [75], [76]. At each iteration step, the memberships u_{ij} and the cluster centres are updated as follows:

$$u_{ij} = \frac{1}{\sum_{k=1}^c \left(\frac{\|x_i - v_j\|}{\|x_i - v_k\|} \right)^{\frac{2}{m-1}}} \quad (3.35)$$

$$v_j = \frac{\sum_{i=1}^n u_{ij}^m x_i}{\sum_{i=1}^n u_{ij}^m} \quad (3.36)$$

Given a dataset with n number of data points (x_1, x_2, \dots, x_n) which to be partitioned into k clusters (c_1, c_2, \dots, c_k) , where $k < n$. The fuzzy c-means performs clustering of this dataset following these steps:

1. Choose cluster centres (v_1, v_2, \dots, v_k) randomly based on the data and given clusters number k .
2. Calculate initial matrix $U = u_{ij}$, U^0 so that $0 \leq u_{ij}^m < 1$, $\sum_{i=1}^c u_{ij}^m = 1$ and $0 < \sum_{j=1}^m u_{ij}^m < n$.
3. Assign each data to the nearest cluster centre based on the objective function J_m given by Equation (3.34).
4. For the next i -th step, calculate new cluster centres (v_1, v_2, \dots, v_k) via U^i according to Equation (3.36).
5. Update U^i to U^{i+1} .
6. Stop the iteration if the condition $\|U^{i+1} - U^i\| \leq \varepsilon$ otherwise return to step 3.

When the stopping criterion is met, the process converges to a local minimum of the objective function J_m and the optimum fuzzy clustering of data is achieved [75].

Figure 3.9 represents an example of fuzzy c-means clustering on a two-dimensional data. The three initial cluster centres; shown as light pink dots; are chosen randomly and their associated Voronoi tessellations are indicated by line number 1. The membership grades and associated cluster centres are adjusted with each iteration step. The algorithm converges after four iterations. The final cluster centres are denoted by bold red dots and their Voronoi tessellations are indicated by line number 4.

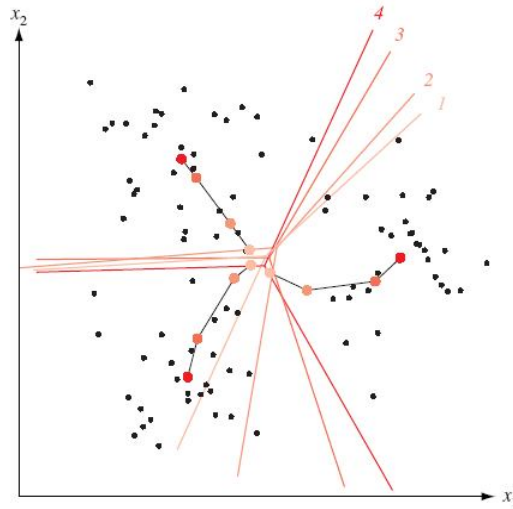


Figure 3.9: Illustration of cluster centres trajectories in fuzzy c-means clustering applied in a two-dimensional data [76]

The performance of clustering algorithms depends on the selected cluster number k and the initial positions of cluster centres. Usually, the number of clusters k is provided by the user or determined from the data using some pre-defined criteria. The choice of the initial cluster centres depends on the type of the data given and can be inferred from the data itself. The final cluster centres differ based on the initial starting centres used when performing fuzzy c-means clustering.

3.7 Threshold-Based Segmentation

Thresholding is one of the simplest and most common segmentation techniques in image processing. The goal of thresholding is to segment regions of pixels with intensity values more than or less than a certain threshold from the rest of the image. The most common thresholding technique which is used in this work is thresholding using Otsu's method [77].

3.7.1 Otsu's Thresholding Method

Otsu's thresholding method is based on maximizing the inter-class variance which is a common measure in statistical discriminative analysis [77], [78]. The basic idea is

that an optimum threshold value is selected so that distinctive regions are well separated with respect to intensity values [78]. The computation of the threshold value utilises information derived from the histogram of the image.

The algorithm assumes that there are two classes or regions in the image that are represented by a bi-modal histogram of the image. The algorithm then calculates the optimal threshold based on information from the histogram separating these two regions so that their combined inter-class variance is maximal.

Let the pixels of a given image A be represented by L grey levels $[1, 2, \dots, L]$. The total number of image pixels is given by N . The histogram of the image is normalized and computed as a probability distribution represented as:

$$p_i = n_i / N \quad \text{given that } p_i \geq 0 \text{ and } \sum_{i=1}^L p_i = 1 \quad (3.37)$$

Suppose the pixels in the image are partitioned into two classes C_o and C_1 by a threshold value j such that all pixels with levels $[1, 2, \dots, j]$ belong to class C_o and all pixels with levels $[j+1, \dots, L]$ belong to class C_1 respectively. The probabilities of class occurrence are given by:

$$\omega_o = \Pr(C_o) = \sum_{i=1}^j p_i = \omega(j) \quad (3.38)$$

$$\omega_1 = \Pr(C_1) = \sum_{i=j+1}^L p_i = 1 - \omega(j) \quad (3.39)$$

where $\omega(j) = \sum_{i=1}^j p_i$ is the 0th – order cumulative moment of the histogram evaluated up till level j . The class mean levels are given by:

$$\mu_o = \sum_{i=1}^j \frac{i \cdot p_i}{\omega_o} = \frac{\mu(j)}{\omega(j)} \quad (3.40)$$

$$\mu_1 = \sum_{i=j+1}^L \frac{i \cdot p_i}{\omega_1} = \frac{\mu_T - \mu(j)}{1 - \omega(j)} \quad (3.41)$$

where $\mu(j) = \sum_{i=1}^j i \cdot p_i$ is the 1st- order cumulative moment of the histogram up till level

j and $\mu_T = \mu(L) = \sum_{i=1}^L i \cdot p_i$ is the total mean level of the original image A .

To calculate an optimum threshold level that best segments both classes C_o and C_1 the inter-class variance is used as a measure of class separation [77]. The inter-class variance σ_B^2 is defined as:

$$\sigma_B^2 = \omega_o (\mu_o - \mu_T)^2 - \omega_1 (\mu_1 - \mu_T)^2 = \omega_o \omega_1 (\mu_1 - \mu_o)^2 \quad (3.42)$$

The threshold value is then determined as the value that maximizes the inter-class variance define in Equation (3.42). Figure 3.10 illustrates an example of image segmentation based on Otsu's thresholding method. Figure 3.10 (a) shows the original grey-level image that depicts two distinctive regions, the coins and the wall background. Figure 3.10 (b) shows the bi-modal histogram of the image with the location and value of the segmentation threshold selected based on Otsu's method indicated by the arrow. As depicted in the histogram, pixels with intensity values less than the calculated threshold belong to the coins regions while the pixels intensity values more than the threshold belong to the background. Figure 3.10 (c) shows the binary images resulted from the segmentation. The image clearly shows the coins regions segmented from the background. Otsu's thresholding method is best used to separate distinctive objects from backgrounds [78].

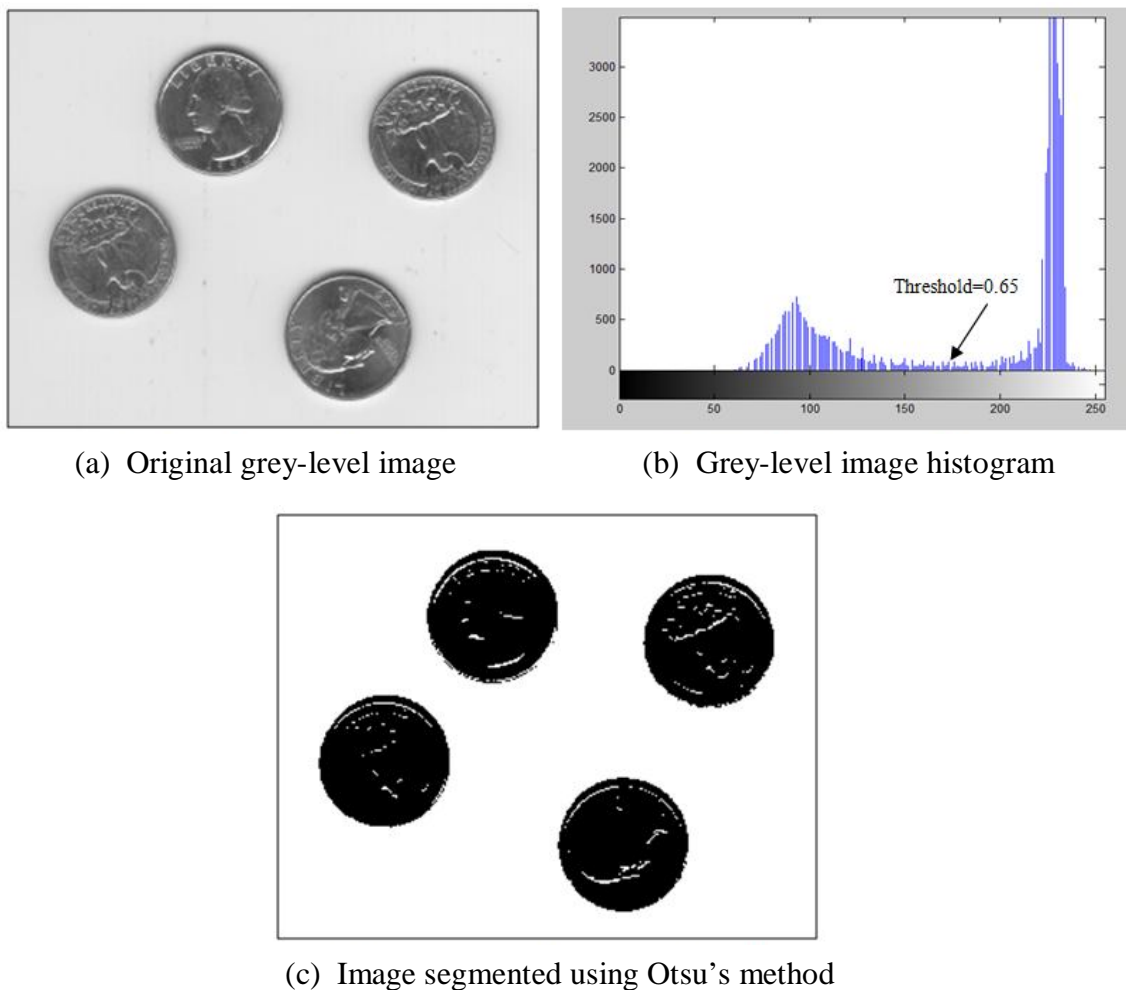


Figure 3.10: Segmentation using Otsu's thresholding method

3.8 Summary

This chapter explores the concept of colour vision and the formation of digital colour images. It also investigates some of the important data analysis and image processing techniques that are utilised in this research work.

Colour vision is the ability to distinguish objects based on the wavelength of the light reflected, emitted or transmitted from/through them. The light reflected from an object incorporates both the light source spectral properties and its spectral properties corresponding to wavelengths in the visible spectrum. The reflected light then enters the retina in the eye where it interacts with the cone cells that send signals to the visual cortex of the brain to interpret the colour of the object. The light reflected from

objects can be registered with acquisition devices such as digital cameras. Most digital cameras use CCD sensors covered with Bayer colour filter mask to generate an RGB colour image [56], [57]. Digital cameras and other devices however do not have the ability to perceive colours correctly especially if the spectrum of the incident illumination is altered due to varying ambient light conditions. It is important to correct any colour and compensate for the change in the spectrum of the incident light in relation to the actual illumination used in the acquisition [58].

Principal Components Analysis (PCA) is a mathematical technique that is applied in multivariate data analysis of many fields such as neuroscience, computer graphics and image data compression. The main idea behind PCA is to utilise an orthogonal linear transformation to obtain new datasets of principal components so that most of the variance in the original datasets is retained in the first few principal components [61]. The goal of PCA is to identify the most meaningful basis to re-express complex multidimensional datasets as linear combinations of these basis vectors for the purpose of either dimension reduction or extraction of useful hidden information from the dataset [64].

Independent Component Analysis (ICA) is a multivariate data analysis technique used to recover source signals from their observed linear combinations. It is the most widely used technique applied in blind source separation. ICA assumes that the observed signals are generated by linearly mixing original source signals with an unknown mixing matrix [66], [67]. ICA estimates the source signals by relying on the assumption that the sources are statistically independent which is achieved when the probability density function of the sources can be written as the product of their marginal independent distributions [67]. In this study, fastICA technique is implemented where the independent components are found as projections that maximize non-Gaussianity [66], [69-71]. In this method, Negentropy, which measures the difference of entropy between a Gaussian variable and a given variable, is used as a measure for non-Gaussianity. Since computing negentropy is very difficult, Newton's iterative approximation is used to find the independent components. The performance of the approximation depends on the choice of non-quadratic function used.

Clustering is a common technique of unsupervised learning and classification where elements of a dataset are partitioned into several clusters so that points in one group are similar to each other and are as different as possible from points in other groups [74]. In this study, soft clustering is employed utilising fuzzy c-means algorithms. In fuzzy c-means, each point in the dataset is assigned membership grades to each of k number of clusters based on a similarity measure, usually the Euclidean distance, between the point and the cluster centre [75]. The performance of clustering algorithms depends on the selected cluster number k and the initial values of cluster centres. A fuzzy soft clustering becomes a hard clustering when each data element is assigned to the cluster with the largest membership level.

Thresholding is one of the simplest and most common segmentation techniques in image processing. The goal of thresholding is to segment regions of pixels with intensity values more than or less than a certain threshold from the rest of the image. The most common thresholding technique which is used in this work is thresholding using Otsu's method [77]. Otsu's method performs thresholding based on maximizing the inter-class variance which is a common measure in statistical discriminative analysis [77], [78]. The method assumes that there are two classes or regions in the image that are represented by a bi-modal histogram of the image. The algorithm then calculates the optimal threshold based on information from the histogram separating these two regions so that their combined inter-class variance is maximal.

CHAPTER 4

GRANULATION TISSUE DETECTION SYSTEM FOR CHRONIC ULCERS

4.1 Introduction

The ability to measure objectively early stages of ulcer healing is crucial for ulcer assessment and management. In chronic ulcers, healing is indicated by the growth of granulation tissue. This Chapter presents the developed system for detection of granulation tissue from colour images of chronic ulcers. Identifying and quantifying the amount of detected granulation tissue gives an indication of the healing progression which reflects on the efficacy of the ulcer management and treatment.

Section 4.2 illustrates the flow of the granulation detection system development. Section 4.3 elaborates the process of acquiring the digital colour images of chronic ulcers required for this study. Section 4.4 illustrates the pre-processing procedures applied on the acquired images. Sections 4.5 and 4.6 explore the main algorithms developed to detect regions of granulation tissue in images of chronic ulcers. Section 4.7 illustrates how the detected regions of the granulation tissue can be utilised to monitor the ulcer healing progression. Finally, the main ideas and findings of this Chapter are summarized in section 4.8.

4.2 Flow Chart of Granulation Tissue Detection System

Figure 4.1 depicts the flow chart of the granulation tissue detection system developed in this study. The system comprises five main sections: acquiring colour images of chronic ulcers, pre-processing of acquired ulcer images and dataset preparation, data transformation applied on ulcer images to determine regions of granulation tissue,

clustering-based segmentation of granulation tissue regions and finally, measuring the amount of detected granulation tissue that can be used for healing assessment and monitoring. These processes are elaborated in the following sections.

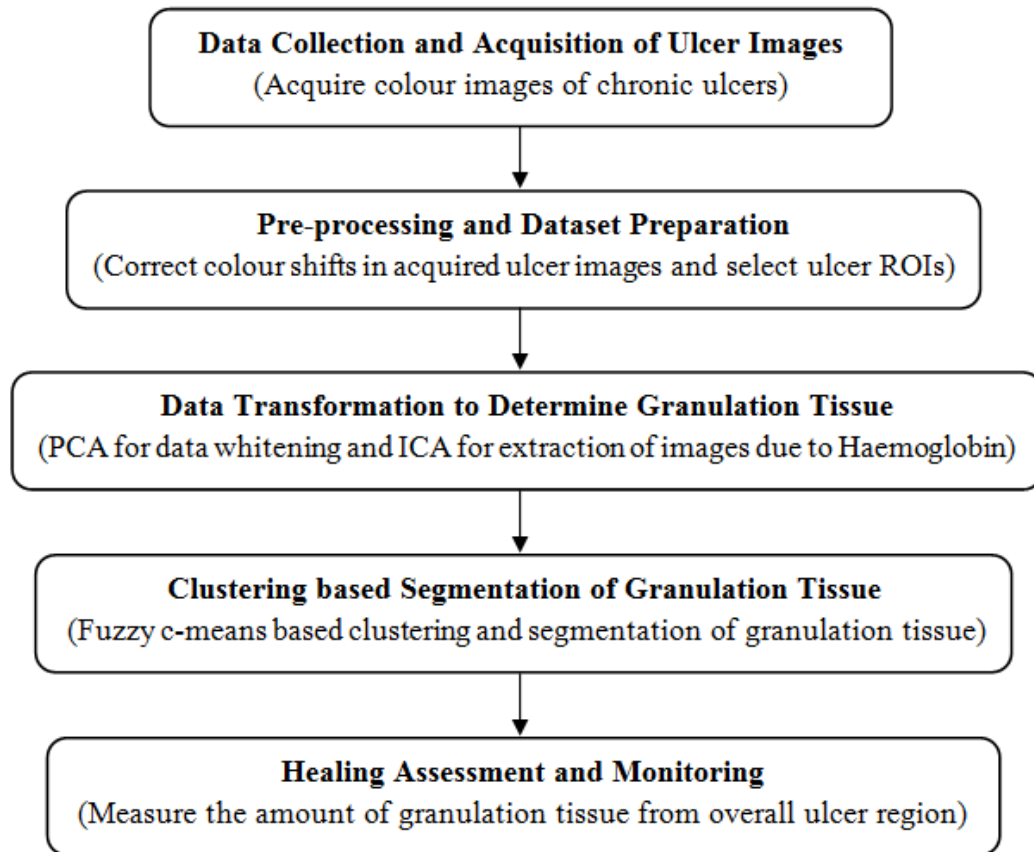


Figure 4.1: Flow chart of granulation tissue detection system

4.3 Data Collection and Acquisition of Ulcer Images

Colour images of chronic leg ulcers of different types and aetiologies that contain a mixture of tissues were acquired at Hospital Kuala Lumpur, Malaysia. This was very crucial to this study as it ensured working on ulcer images taken under actual acquisition conditions. For this study, ninety colour images were acquired from sixty-nine patients with chronic leg ulcers at ulcer clinics at the Department of Dermatology and at the Out-Patient Department in Hospital Kuala Lumpur.

This research work is a collaborative study between Universiti Teknologi Petronas (UTP) and Hospital Kuala Lumpur. It has been approved by the Ethics Committee of the Ministry of Health, Malaysia, and registered with the National Medical Research Registry (NMRR, Malaysia) under the study code NMRR-11-50-8340.

4.3.1 Data Acquisition Settings

Acquisition Device: Ulcers are chronic wounds that cause severe pain and discomfort to the patients. There is a high chance of bacterial infections if these ulcers are not managed properly during data acquisition sessions. Hence, it was important to ensure that the data acquisition device used in this study did not come in contact with the ulcer and the overall acquisition process was non-invasive. Furthermore, the selected acquisition device had to produce high resolution images to ensure an accurate assessment and analysis. A handheld digital single lens reflector (DSLR) camera, Nikon D300, with a resolution of 12.3 megapixels was used to acquire the colour images of the chronic ulcers. Since the ulcer size can vary from small and deep to large and shallow, a standard lens AF-S DX Nikon 16-85mm f/3.5-5.6G ED VR was used to ensure that the ulcer region was enclosed within the field of view of the lens. Figure 4.2 shows the digital camera and lens used to acquire the ulcer images.



Figure 4.2: Digital Single Lens Reflector Camera (Nikon D300) and AF-S DX Nikon 16-85mm f/3.5-5.6G ED VR Lens

Light Source: Due to the severe conditions of the ulcers for some patients who were unable to walk or sit properly, it was not possible to conduct the data acquisition sessions in a photography room that is specifically designed for this purpose. Instead, the images were acquired at the dressing room where the ulcers were examined by the

attending nurses. The ambient light in the dressing room is a combination of fluorescent light from the ceiling and daylight coming from the window as shown in Figure 4.3. This ambient light was not adequate to acquire images and could vary depending on the weather conditions. Hence, a Nikon SB-900 flashlight, shown in Figure 4.4, was used to provide adequate reproducible lighting for image acquisition. A diffuser dome was mounted on the flashlight to avoid harsh lighting and shadows.



Figure 4.3: Wound dressing room where most of the images are acquired



Figure 4.4: Nikon SB-900 flashlight with diffuser dome

Colour and Size Reference: As has been explained in Chapter 3 (section 3.2.4), varying ambient light can cause undesirable colour casts in the acquired digital images. During the acquisition sessions for this study, colour casts were produced due to the combined effect of several light sources (fluorescent light and sunlight) and

the flashlight reflected back from the surrounding brown-yellow walls in the dressing room. Hence, a white reference (white point) was included in the image to correct for these colour shifts. A 3x6cm white colour sticker was placed near the ulcer during the photography sessions to provide a reference for colour shifts correction. For small ulcers that were located in challenging locations such as toes, heels and the sides of feet, a small white sticker of size 9x13 mm was used instead. The white sticker was also used as a size reference to measure the area of the detected granulation tissue. Figure 4.5 shows the reference stickers placed next to ulcers during the data acquisition sessions.



Figure 4.5: Reference stickers placed near ulcers for colour and size reference

4.3.2 Data Acquisition Procedure

Chronic ulcers cause severe pain and discomfort to the patients which make them unable to walk most of the time. When patients come in to the dressing room in the clinic, their comfort must be given a high priority. Patients will be attended to by the nurses who will help them to lie down or sit comfortably on the dressing bed extending their legs on the bed and their feet rested on a special pillow. The ulcers are then examined and cleaned by the nurses. The ulcer images for this study were acquired before the new dressing was applied to the ulcers.

The data acquisition procedure involved three main steps as depicted in the flow chart of Figure 4.6:

- a) **Fulfilling Inclusion/Exclusion Criteria:** The target population for this study was adult patients above eighteen years with chronic leg ulcers attending the

ulcer clinics at the Department of Dermatology and the Outpatient Department at Hospital Kuala Lumpur during the study period. All ulcers of different types and aetiologies which contained a mixture of several tissues were included in the study. However, there were ulcers that were excluded from this study such as large ulcers that extended around the leg curvature or ulcers located in challenging positions such as between the toes. Ulcers that contain heavy exudates would cause severe specular reflections when photographed with flashlight and hence were excluded from the study as well. Furthermore, due to infection that affected a number of ulcers, some parts of the ulcer heal and rose faster than other parts resulting in an uneven ulcer surface. Uneven ulcer surfaces would obstruct the light path and cause shadows when photographed with flash and hence were excluded from the study.

- b) **Obtaining Patient Consent:** Before acquiring the ulcer images, the patients were informed as to the nature and objective of the study. A written consent on participation in the study as well as acquisition of the ulcer image was then obtained from the patients. Study information sheets and patient consent forms used in this study are attached in Appendix A.
- c) **Acquisition Images of Ulcers:** Colour images of the ulcers were acquired using a high-resolution handheld DSLR camera. The camera was placed perpendicular to the ulcer to ensure the inclusion of the whole ulcer wound within the field of the view of the camera. The flashlight was directed to either the wall or the ceiling to provide a more diffused illumination to avoid specular reflections. Several images were acquired of the same ulcer from different sides.

From the ninety images acquired for this study, seventy five images that have met the inclusion criteria and provided the best view of the ulcers under optimum lighting conditions were used in the study.

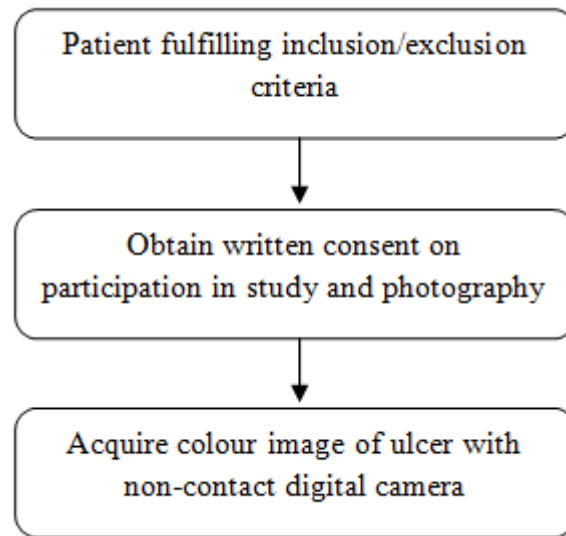


Figure 4.6: Flow chart of data acquisition procedure

4.4 Pre-processing and Ulcer Dataset Preparation

Before the ulcer images can be input to the granulation tissue detection algorithms, a set of pre-processing steps are needed to be performed. These steps comprises of correcting colour shifts and selecting regions of interest (ROIs).

4.4.1 Correcting Colour Shifts

The dressing rooms at the clinic in the Department of Dermatology and the Out-Patient Department, Hospital Kuala Lumpur are not equipped with adequate ambient illumination to perform standard digital photography. Furthermore, the light from the flash falls onto the yellow-brown wall in the room and reflects back creating a yellow cast over the acquired images. To correct these colour shifts, the digital camera was calibrated so that it produces equal RGB values for a white patch under flashlight (white illumination) photography. However, due to the variety of light sources constituting the ambient illumination in the dressing room, colour shifts that could not be easily corrected using the camera settings were still produced. Hence, there was a need to correct for these colour shifts before processing the ulcer images.

Since the dominant illumination source used in this study was white flashlight, a white point estimation algorithm, or "max white", has been implemented to correct for colour shifts. The white point algorithm assumes that there is a white reference in the image through which the chromaticity scaling factors are calculated. These scaling factors are determined based on the assumption that the maximum of each of the Red, Green and Blue channels in the image are found in this reference point and correspond to pure white [58], [60]. Figure 4.7 is a flow chart of the colour correction procedure applied on the acquired colour ulcer images in this study.

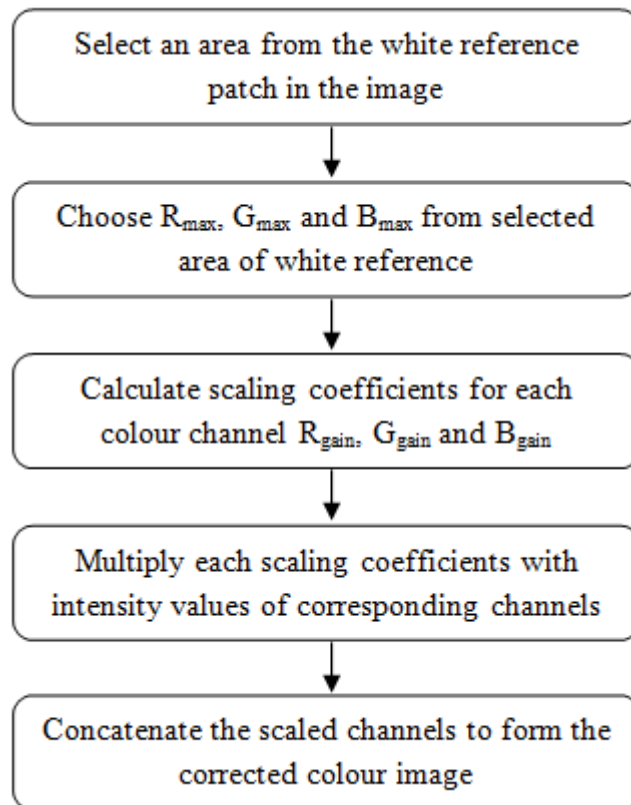


Figure 4.7: Flow chart of the colour correction procedure

A small area from the white reference sticker was selected manually and maximum intensity values R_{\max} , G_{\max} , and B_{\max} were obtained from each colour channel, respectively. By comparing these values with values of a white illuminant, the scaling coefficients were calculated accordingly:

$$R_{gain} = 2^n / R_{max} \quad (4.1)$$

$$G_{gain} = 2^n / G_{max} \quad (4.2)$$

$$B_{gain} = 2^n / B_{max} \quad (4.3)$$

where n is the number of bits per channel (in this case $n = 8$ and $2^n = 256$ which corresponds to the full intensity of white light), and R_{max} , G_{max} , and B_{max} are the maximum values extracted from the white reference sticker.

By scaling the Red, Green and Blue channels of the ulcer image using the calculated scaling factors, the corrected image was obtained. Figure 4.8 shows an ulcer image corrected using the developed colour shifts correction algorithm. Figure 4.8 (a) shows the ulcer image before colour correction and Figure 4.8 (b) shows the ulcer image after colour correction had been applied.



(a) Ulcer image before colour correction (b) Ulcer image after colour correction

Figure 4.8: Ulcer image corrected using developed colour shifts correction algorithm

4.4.2 Selecting Regions of Interest (ROIs)

After colour correction had been applied on the acquired ulcer images, two main regions of interest were manually selected from the images. The first region is the "ulcer region" which included the ulcer and some of the surrounding skin. Ulcer regions had to be excluded from the background which might contain unwanted regions of the surroundings such as other parts of the patient's body and the wall of the room. These unwanted regions could have affected the algorithm performance and

produced inaccurate results. Hence, the images that input to the granulation detection system had to be carefully selected to include the ulcer region only.

The second region selected from the image was the "reference patch region" which included the size reference patches. This was needed to calculate the area of the detected regions of the granulation tissue. Figure 4.9 illustrates the two selected regions from the colour corrected ulcer image.

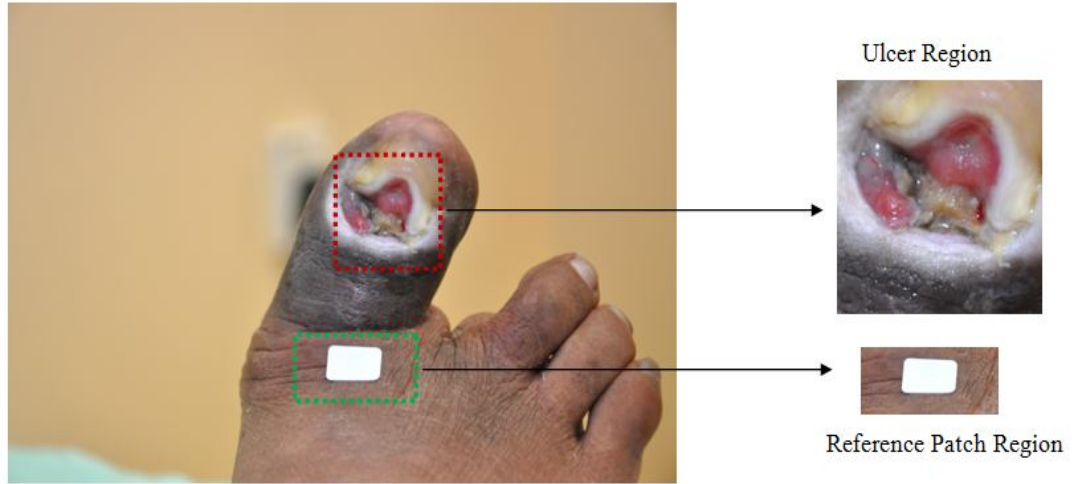


Figure 4.9: Selection of regions of interest (ROIs) from colour corrected ulcer image

4.5 Data Transformation to Determine Granulation Tissue Regions

Ulcer healing is indicated by the growth of granulation tissue which appears red in colour due to the pigment haemoglobin content in the small blood capillaries formed within the granulation tissue [24]. In this study, the main objective was to utilise the optical characteristics of pigment haemoglobin to detect the regions of the granulation tissue that formed a measure of ulcer healing. The approach is to apply data transformation on the acquired and pre-processed the colour images of chronic ulcers to extract grey-level images that show the distribution of pigment haemoglobin. Extracted areas of haemoglobin distribution reflect regions of granulation tissue on ulcer surface. Figure 4.10 is a flow chart of the developed algorithm to extract the images of the haemoglobin distribution. A detailed explanation of the algorithm is given in the following sub-sections.

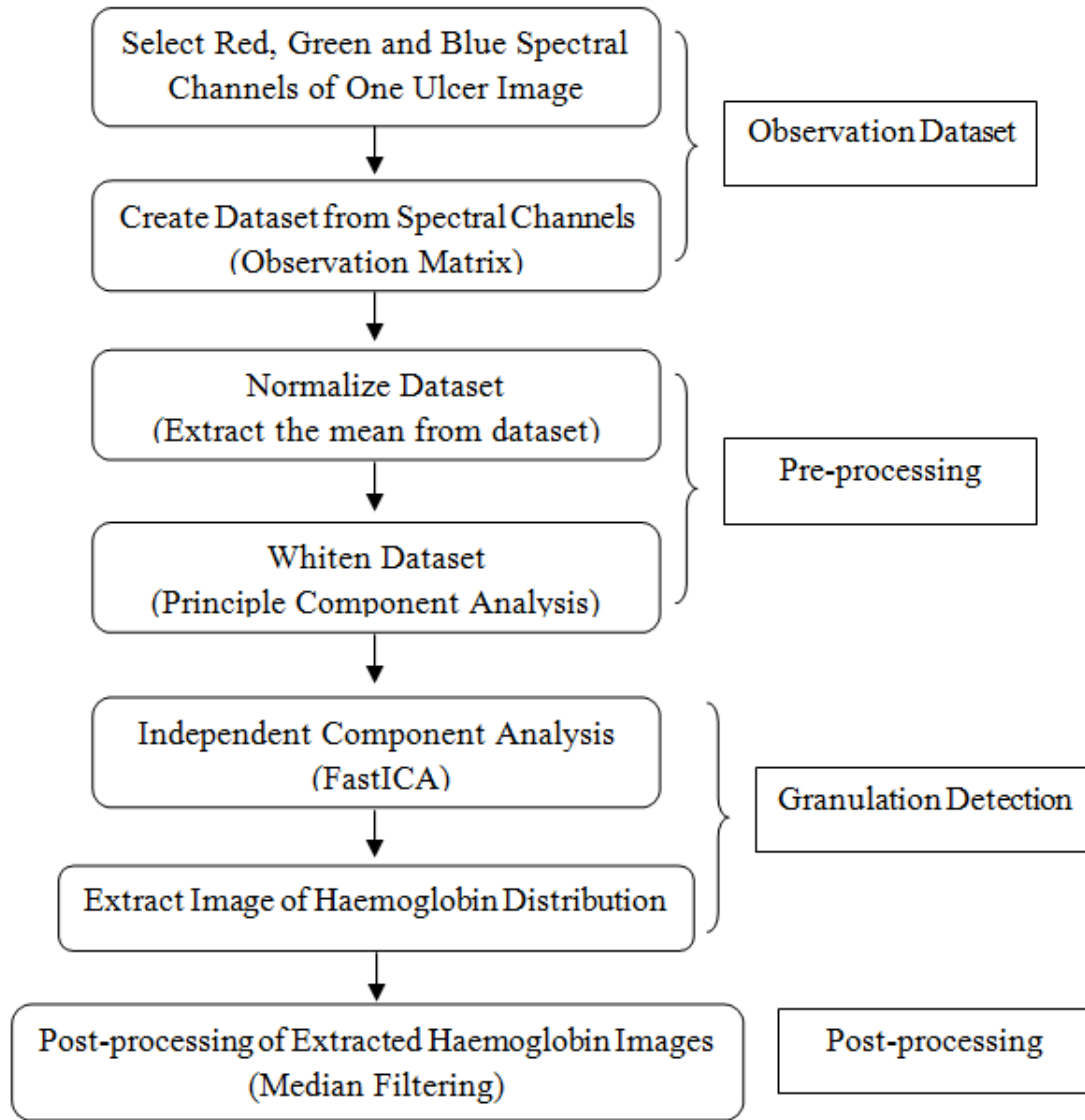


Figure 4.10: Flow chart of the developed algorithm to determine regions of haemoglobin distribution from colour ulcer images

4.5.1 Creating Observation Input Dataset

Each colour ulcer image comprises three grey-level images representing the spectral bands of Red, Green and Blue channels respectively. These images represent three observations of linear combinations of image source signals. For each ulcer image, these bands are used to create column vectors of a data matrix comprising an observation dataset (observation matrix) as shown in Figure 4.11.

The observation matrix X contains observations of the colour ulcer image. Each column of X corresponds to a set of intensity values from each of the Red, Green and Blue colour channels (three observations). Each row of X corresponds to intensity values of Red, Green and Blue channels of one particular pixel location.

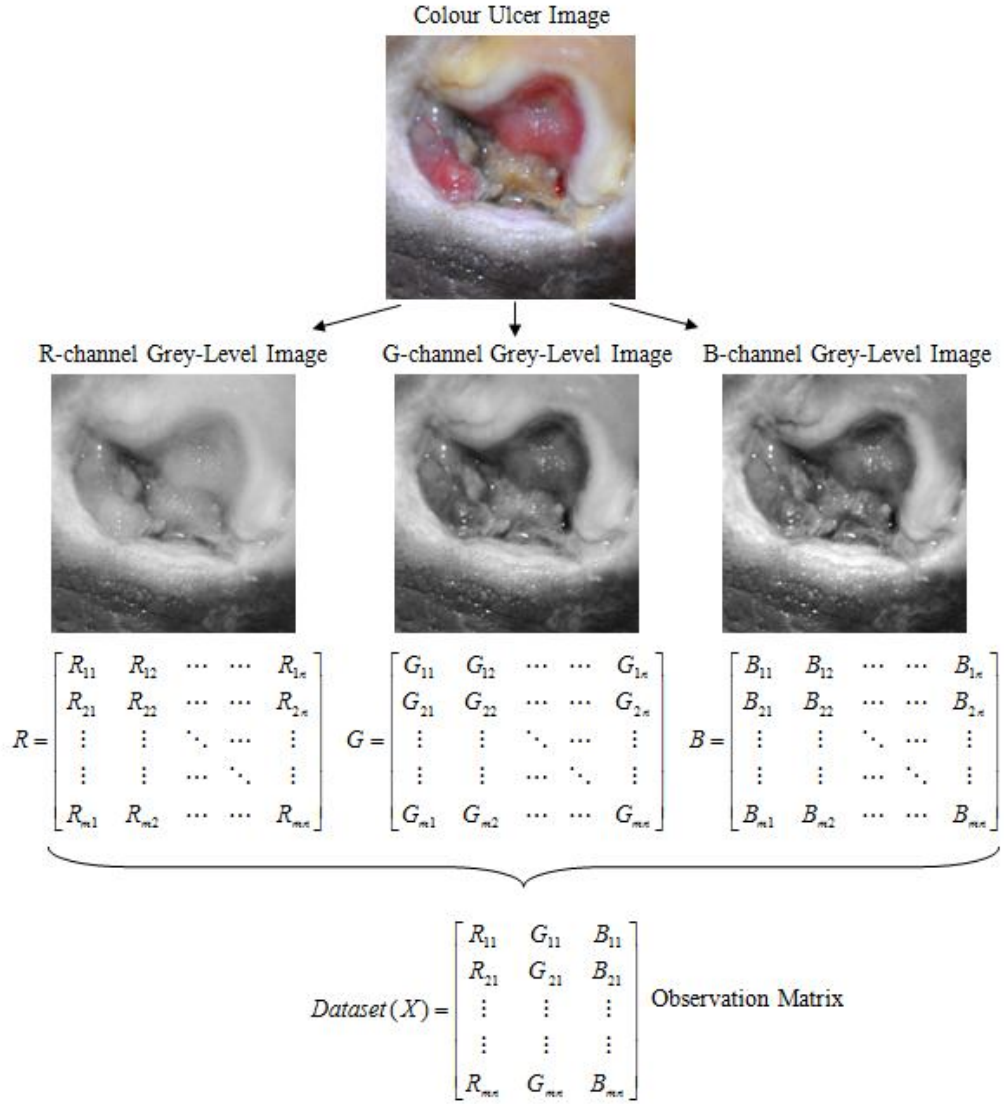


Figure 4.11: Create observation input dataset from colour ulcer image

4.5.2 Pre-Processing of Input Dataset

The Independent Component Analysis (ICA) was applied on the observation dataset to extract the independent source images from the observed ones. However, before

applying the algorithm, it was important that the dataset was pre-processed accordingly.

As depicted in Figure 4.12, pre-processing of the observation dataset involved two steps. First the dataset was normalized to centre on a zero point by extracting the mean value from each spectral band. Data whitening was then applied by employing the Principle Component Analysis (PCA) to transform the dataset linearly so that its components were uncorrelated and their variances equalled unity. The pre-processing steps were performed to simplify the ICA algorithms and reduce the number of parameters to be estimated as explained in Chapter 3 (section 3.5.1).

4.5.3 Detection of Haemoglobin Distribution

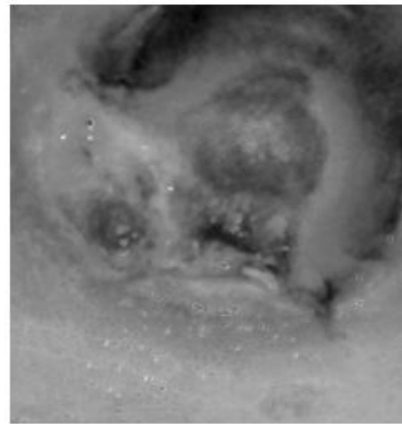
In this work, the independent component analysis was employed to extract the source grey level images that represented the regions of granulation tissue in the colour images of chronic ulcers. ICA was implemented using the fastICA algorithm explained in Chapter 3 (section 3.5). FastICA is based on a fixed-point iteration that uses maximization of non-Gaussianity as a measure of independence to estimate the independent components. The non-quadratic function G that is used to approximate negentropy as a measure for non-Gaussianity is defined in Equation (3.26).

The algorithm has been developed so that it estimates all the independent source images at once. The output from the ICA algorithm is a matrix that contains row vectors of independent components equal to the number of observations, which were three observations in this case. These row vectors are rearranged as matrices, each representing a grey-level image of an estimated independent source. One of the estimated source images was an image that showed regions of the haemoglobin distribution reflecting the existing regions of the granulation tissue on the ulcer's surface. Figure 4.12 shows a colour ulcer image and the corresponding estimated independent source images. Figure 4.12 (c) shows the second independent source image which represented the regions of a significant intensity value range (dark region in the image) that could be clearly distinguished from the rest of the image.

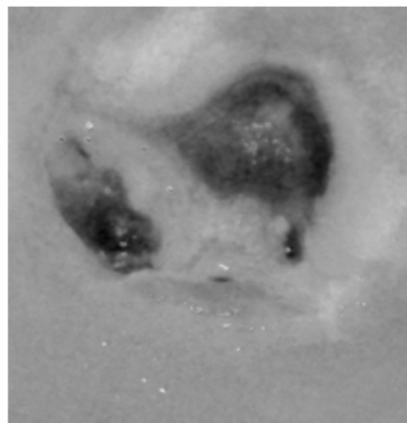
These areas indicated haemoglobin distribution that reflected the regions of granulation tissue.



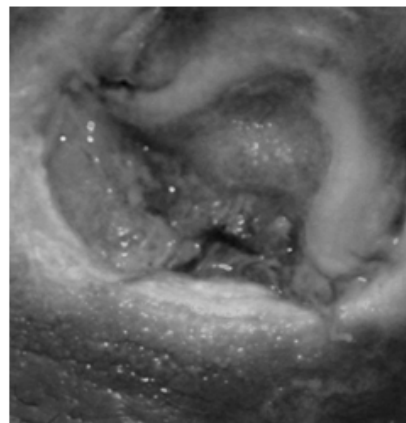
(a) Original ulcer image



(b) 1st independent component



(c) 2nd independent component

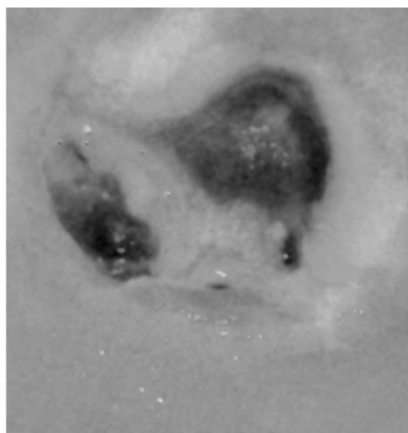


(d) 3rd independent component

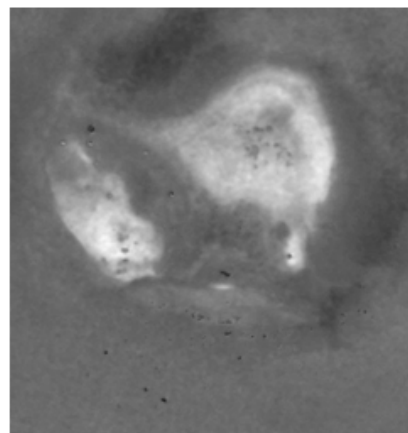
Figure 4.12: Extracted independent sources from observed colour ulcer image

It should be noted that there was no order for the estimated independent components. Figure 4.12 indicates that the second source image was the extracted haemoglobin image that showed the regions of the granulation tissue in this case. If however, the algorithm was applied on the same image again, the granulation tissue might be detected in the first or the third estimated independent source image. This is not a significant issue since the algorithm was developed to estimate all the independent sources from the original image.

It should also be noted that the estimated source images could have a negative sign and show inverted images when estimated using the developed algorithm. This is due to the nature of the convergence criterion that has to be met when estimating the independent components as explained in Chapter 3 (section 3.5.6). This would also not be an issue because the detected regions of the granulation tissue would still appear with a distinguished range of intensity values even in the inverted images. Figure 4.13 shows an example of two source images estimated at two different times from the colour ulcer image shown in Figure 4.12 (a). In both images, the arrow clearly indicates the identified region of the granulation tissue that appears with a distinctive range of intensity values that could be easily segmented from the rest of the image. However, all extracted haemoglobin images were further processed to ensure that the identified granulation regions appeared as distinctive dark regions, shown in Figure 4.13 (a), to simplify the segmentation algorithm explained in the next section. The performance of the developed data transformation algorithms to identify regions of granulation is investigated in the next Chapter.



(a) Extracted haemoglobin image



(b) Extracted haemoglobin image inverted

Figure 4.13: Extracted Image Due to Pigment Haemoglobin

4.5.4 Post-Processing of Extracted Haemoglobin Images

It has been explained in section 4.3 that ulcers with heavy exudates have been excluded from this study. However, exudates are an essential part of the wound environment and as a result most ulcers have at least a little amount of exudates present on the surface. Hence, some unavoidable specular reflections were caused

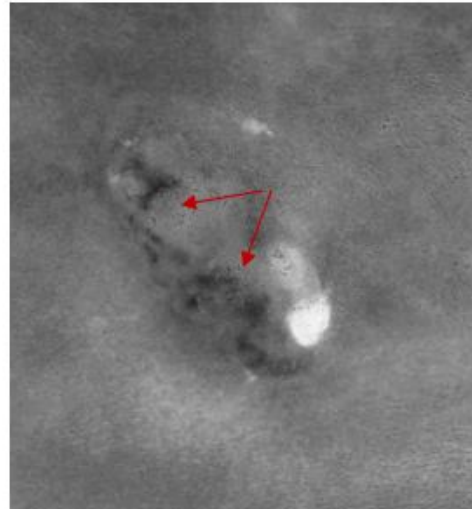
when these ulcers were photographed with the flashlight. The specular reflections pixels appeared in the extracted haemoglobin image with distinctive intensity values that differed from other neighbouring pixels. Some of these pixels were perceived as white pixels within dark grey or black neighbouring pixels while others were perceived as black pixels within light grey or white neighbouring pixels. Hence, this type of noise is normally referred to as a salt and pepper type of noise. It was important to identify and remove these pixels to ensure a better detection of the granulation regions.

Median filters are nonlinear spatial filters often used to remove salt and pepper noise (impulse noise) from images [79]. The advantage of using median filters is that they remove the noise while maintaining the details and edges in the image. The working principle of a median filter is that it uses a defined ($n \times n$) size window which slides over the whole image pixel by pixel replacing it with the median value of the neighbouring pixels contained within the window. The median filter operation forces distinct pixels values to be similar to their neighbours and hence effectively remove salt and pepper pixels [79]. However, the drawback of using median filters is that the edges and details get blurred when increasing the window size of the filter.

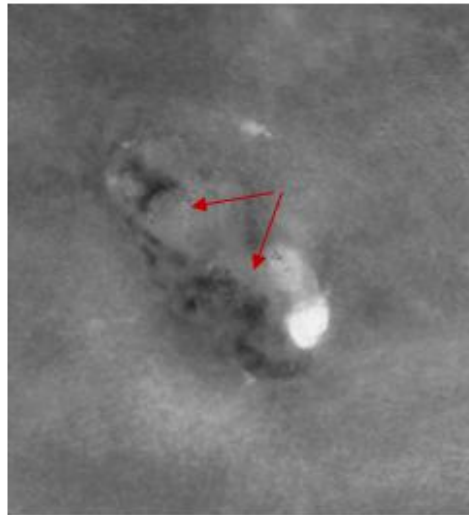
In this study, a median filter with windows sizes of 3×3 and 5×5 pixels was used to remove the resulted salt and pepper noise pixels from the extracted haemoglobin images. The size of the window was chosen after applying median filtering on extracted haemoglobin images with varying window sizes of 3×3 , 5×5 , 7×7 , and 9×9 pixels. In this study, window sizes of 3×3 and 5×5 pixels best removed most of the impulse noise from the extracted haemoglobin images while maintaining the overall shape and details in the image. Figure 4.14 depicts an example of the removal of the salt and pepper noise from the extracted haemoglobin images. Figure 4.14 (a) shows the original ulcer image with the specular reflections indicated by the green arrows, while Figure 4.14 (b) shows the extracted haemoglobin images with impulse noise pixels (salt and pepper noise) indicated by the green arrows. Figure 4.14 (c) shows the extracted haemoglobin image after removing the affected impulse pixels using median filtering with window size of 5×5 pixels.



(a) Original colour ulcer image



(b) Extracted Haemoglobin Image



(c) Filtered Extracted Haemoglobin Image

Figure 4.14: Removal of impulse noise from extracted haemoglobin images

4.6 Clustering-Based Segmentation of Granulation Tissue Regions

Segmentation is an image processing technique that is used to subdivide an image into constitute regions. It is needed to isolate regions of interest from the rest of the images for further processing and analysis. Segmentation normally results in a binary image with only two possible intensity values; 0 (black) or 1 (white). In this study, the identified regions of the granulation tissue on each extracted haemoglobin image

were segmented from the rest of the image. The segmented regions of the granulation tissue can be measured and utilised as an objective measure to monitor the ulcer healing progression.

The input images to the segmentation algorithms were the grey-level images that were extracted from the colour images of the ulcers using the data transformation algorithms explained section 4.5. These images, referred to as "haemoglobin images" in the remainder of this text, indicated the distribution of pigment haemoglobin reflecting the identified regions of the granulation tissue which appeared with a distinctive range of intensity values that could clearly be separated from the rest of the image as shown in Figure 4.13.

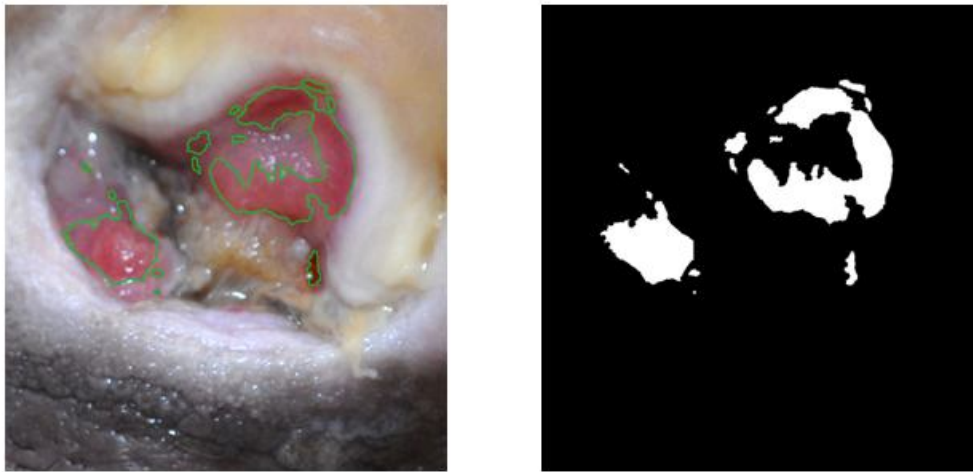
Clustering-based segmentation was employed in this study to segment the identified regions of the granulation tissue on the extracted haemoglobin images. Fuzzy c-means clustering was applied to the haemoglobin images to classify the granulation regions based on their range of intensity values. The classified granulation regions were then segmented from the rest of the images accordingly. These steps are explained in more detail in the following sub-sections. However, before elaborating further on the clustering-based segmentation algorithms employed in this study, it is important to describe the granulation region reference image which was used to select the optimum number of clusters needed to correctly classify the regions of granulation tissue on the extracted haemoglobin images.

4.6.1 Granulation Region Reference Image

As illustrated in section 4.4.2, ulcer regions, that include the ulcer and part of the surrounding skin, were manually selected from the colour corrected ulcer images and input to the granulation tissue detection system. These ulcer images were shown to two dermatologists¹ at Hospital Kuala Lumpur who were asked to trace the region of the granulation tissue manually by drawing a line around the granulation tissue region's boundary. The traced regions produced by each of the two dermatologist

¹ Dermatologists who participated in this study are Dr Adawiyah Jamil and Dr Felix Yap Boon Bin – Department of Dermatology – Hospital Kuala Lumpur.

were further examined visually by both dermatologists to determine an optimum tracing reference of the granulation tissue regions for each ulcer image. The traced regions of the granulation tissue from all of the ulcer images were utilised to create binary images that contained the segmented regions of the granulation tissue which could be used as references for further analysis. These images were referred to as granulation assessment reference images. Figure 4.15 shows a granulation assessment reference image produced from the manual tracing of the granulation tissue regions from a colour ulcer image. Figure 4.15 (a) shows the colour ulcer image with the traced granulation regions indicated with a green boundary. Figure 4.15 (b) shows the binary assessment reference image produced from the tracing.



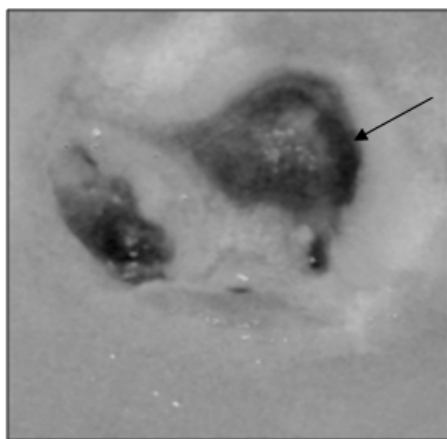
(a) Traced granulation tissue region (b) Granulation region reference image

Figure 4.15: Granulation assessment reference image obtained from manual tracing of granulation tissue

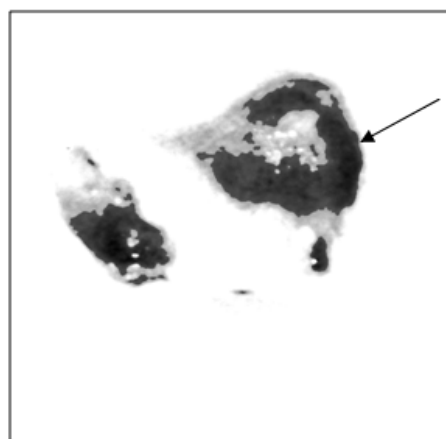
Although the granulation assessment reference images were created based on visual tracing of the granulation region, this was the closest approximation of an actual granulation tissue region in the ulcer. The granulation assessment reference images were utilised to determine the optimum number of clusters to classify the granulation regions in the extracted haemoglobin image as is shown later in the following section. They were also used to compare the amount of the detected granulation tissue using the developed algorithm with the amount traced manually by the dermatologists to calculate the amount of the region overlap for the agreement analysis discussed later in Chapter 5.

4.6.2 Classifying and Segmenting Granulation Tissue Regions

Data clustering is an unsupervised classification approach where similar data items are grouped together into clusters. Fuzzy c-means clustering was the method of soft clustering employed in this study to assign membership grades to each pixel in the extracted haemoglobin images. These membership grades determined the extent to which each pixel belonged to a certain number of clusters based on the Euclidean distance of each pixel value to the mean of the cluster centre as explained in Chapter 3 (section 3.6.2). Depending on the number of clusters k , each cluster was assigned a number $1, 2, \dots, k$. After performing fuzzy c-means clustering, the membership grades of all the pixels for each cluster were determined. The pixels were then assigned to each cluster $1, 2, \dots, k$ according to the highest membership grades corresponding to each cluster. As shown in section 4.5, the granulation tissue region appeared as a distinctive dark region in the extracted haemoglobin image. Hence, the cluster with the minimum cluster centre value was regarded as the granulation cluster and assigned the cluster number 1 accordingly. Figure 4.16 illustrates an example of the classification of the regions in the extracted haemoglobin image utilizing the fuzzy c-mean clustering algorithm. Figure 4.16 (a) shows the extracted haemoglobin image while Figure 4.16 (b) shows corresponding classified image where the pixels were assigned to different regions according to the highest membership grades. The classified granulation tissue regions in the image are indicated by the arrows in the figure.



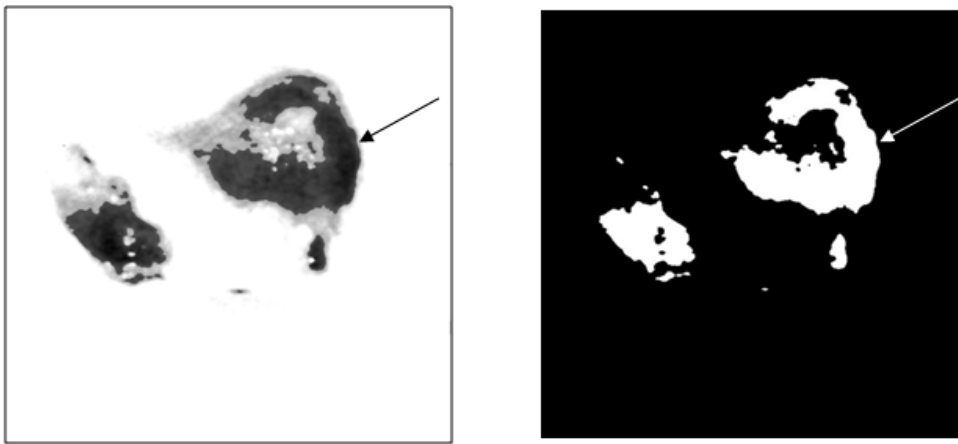
(a) Extracted haemoglobin image



(b) Clustered regions in haemoglobin image

Figure 4.16: Classification of regions in extracted haemoglobin image

The classified image was then converted into a binary image based on the intensity values of the clustered granulation tissue. The segmentation algorithm scanned the classified image resulted from the clustering algorithm for pixels values that belonged to cluster number 1 (clustered granulation tissue) and converts them to value 1 (white) while retaining all other pixels with the value 0 (black). This process produces a binary image where the detected granulation tissue appeared as a black region separated from the rest of the image which appeared as a white background. Figure 4.17 illustrates an example of the granulation tissue segmentation in the classified image. Figure 4.17 (a) shows the classified haemoglobin image and Figure 4.17 (b) shows the corresponding binary image with the segmented granulation tissue indicated by the arrow.



(a) Clustered regions in haemoglobin image (b) Segmented granulation tissue regions

Figure 4.17: Segmentation of clustered granulation tissue in classified image

4.6.3 Selection of Number of Clusters

As discussed in Chapter 3 (section 3.6.2), the selection of the number of clusters k is crucial to the clustering algorithm performance and output accuracy. In order to determine the optimum number of clusters needed for segmentation of the granulation tissue, the segmentation algorithm using fuzzy c-means was applied iteratively on each extracted haemoglobin image with parameter k ranging from $k = 2$ till $k = 10$. The iteration process started with $k = 2$ because the developed algorithm was

expected to classify at least two clusters, the granulation tissue cluster and the cluster for the rest of the ulcer parts.

At each k^{th} iteration step, the segmentation performance was computed by taking the difference between the detected granulation tissue regions using the developed clustering based segmentation algorithms for each number of clusters with the traced granulation region in the granulation assessment reference image obtained from the dermatologist's tracing as explained in section 4.6.1. Figure 4.18 illustrates an example of the computation of the difference between the assessment image and the algorithm image. Figure 4.18 (a) shows the granulation assessment reference image, Figure 4.18 (b) shows the image resulted from the algorithm segmentation of the granulation tissue and Figure 4.18 (c) shows the difference image.



(a) Granulation tissue reference image



(b) Detected granulation tissue image



(c) Granulation tissue difference image

Figure 4.18: Computing the difference between the granulation regions detected using the developed algorithm and the granulation region traced by dermatologists

The optimum number of clusters k was chosen based on the minimum segmentation difference error between the algorithm image and the assessment image. As shown in Figure 4.18 (c), the difference image contained wrongly segmented pixels which were either granulation pixels in the assessment image not detected in the algorithm image or vice versa. The segmentation difference error Er was then obtained by calculating the number of white pixels (wrongly segmented pixels) in the difference image using the following formula:

$$Er = \frac{\sum_{i=1}^n x_i}{N} \quad (4.4)$$

where n is the number of white pixels (wrongly segmented pixels) in the difference image and N is the total number of pixels in the difference image.

The clustering based segmentation algorithm was applied on the haemoglobin images extracted from the seventy-five ulcer images included in this study to segment the identified regions of the granulation tissue from the rest of the images. The minimum segmentation difference error values and the optimum number of clusters obtained for each ulcer image is presented and discussed in Chapter 5.

4.7 Ulcer Healing Assessment and Monitoring

In daily clinical practice, dermatologists depend on a subjective visual inspection of the ulcer appearance to evaluate the its severity and the healing progression. The ulcer surface is normally described as estimated percentages of red, yellow, and black colours which refer to granulation, slough and necrotic tissues, respectively as illustrated in Chapter 2 (section 2.8). The estimated percentage of granulation tissue is particularly important as it indicates the early stages of ulcer healing.

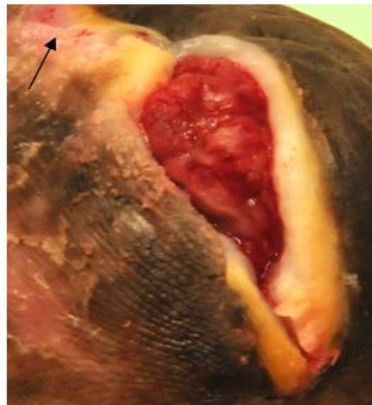
The detected and segmented regions of the granulation tissue from the ulcer images can be utilised as a measure for ulcer healing progression. For each ulcer image, the regions of the granulation tissue can be identified and segmented using the developed granulation tissue detection system. The amount of detected granulation

tissue, in terms of surface area, can be measured during consecutive visits throughout the course of a treatment and used to monitor the healing progression. If the current treatment is effective, the amount of detected granulation tissue should increase throughout the course of the treatment.

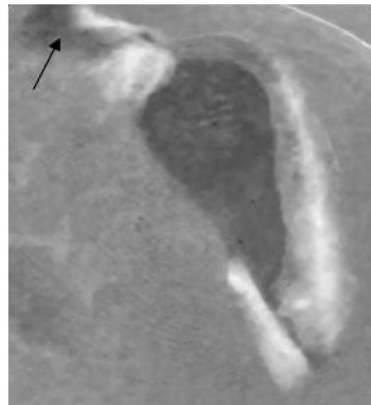
Before the surface area of the detected granulation tissue can be utilized to indicate the healing progression, it is important to eliminate any regions that may be wrongly detected as part of the granulation tissue. The ulcer boundary reference image has been developed for this purpose as shown in the following sub-section.

4.7.1 Ulcer Boundary Reference Image

It was elaborated in Chapter 2 (section 2.5) that chronic ulcers occur mostly due to underlying aetiologies such as venous insufficiency, arterial perfusion and diabetes. Such aetiologies may cause the blood to pool at the surface of the skin that surrounds the ulcers, causing erythema and skin inflammation or laceration. The lacerated skin surrounding the ulcer may have been wrongly detected as part of the granulation tissue in some of the images included in this study. This is illustrated in Figure 4.19 where the arrows indicate a region of skin laceration near the ulcer that was wrongly detected as part of the granulation tissue.



(a) Original ulcer image



(b) Extracted haemoglobin image



(c) Detected granulation tissue image

Figure 4.19: Skin laceration situated near the ulcer that is wrongly detected as granulation tissue

The original ulcer images were shown to dermatologists at Hospital Kuala Lumpur whom were asked to trace manually the boundary of the ulcer on each image. The traced ulcer boundaries were then utilised to create binary images in which the ulcer region was segmented from the rest of the image. These images were referred to as ulcer boundary reference images. Figure 4.20 (a) shows an ulcer image with the ulcer boundary traced with the green line while Figure 4.20 (b) shows the binary ulcer reference image which resulted from the tracing.



(a) Traced ulcer boundary (b) Ulcer boundary reference image

Figure 4.20: Ulcer boundary reference image obtained from manual tracing of the ulcer's boundary

The developed ulcer boundary reference images were used as masks that were applied over the output images from the granulation detection system. By doing so, the detected regions of the granulation tissue within the ulcer boundary region were retained and any wrongly detected parts of the surrounding skin outside the ulcer boundary were eliminated. Figure 4.21 (a) shows the output image from the granulation detection system before applying the ulcer boundary image mask where the arrows indicate the regions wrongly detected as part of the granulation tissue. Figure 4.21 (b) on the other hand shows the output image after applying the ulcer boundary image mask where detected regions outside the ulcer boundary were eliminated and the granulation tissue within the ulcer boundary was retained.



(a) Detection of granulation tissue before applying ulcer region mask (b) Detection of granulation tissue after applying ulcer region mask

Figure 4.21: Removing regions outside the ulcer boundary wrongly detected as granulation tissue

4.7.2 Granulation Region Area Measurement

The surface area of the detected regions of the granulation tissue within the ulcer needed to be measured as an objective measure of the ulcer healing progression. The number of detected granulation pixels (white pixels) were calculated and multiplied with the area per pixels unit (in mm^2) to measure the surface area of the granulation tissue. Therefore, a reference of the area per unit pixel needed to be included in each image.

As illustrated in section 4.4.2 of this chapter, the selected reference patch region from the colour corrected ulcer image included the size reference patch. The grey-level image was extracted from the original colour reference patch image. The size reference patch was then segmented using Otsu's thresholding, explained in Chapter 3 (section 3.7), from the rest of the grey-level image and used to provide a reference of the area per unit pixel to calculate the area of the detected granulation tissue. Figure 4.22 (a) shows the original reference patch image and Figure 4.22 (b) shows the grey-level image of the reference patch image. Figure 4.22 (c) shows the bimodal histogram of the grey-level image indicating two separable regions; the reference patch region (the light region) and the skin region (the dark region). A threshold value of 0.66 was determined from the histogram using Otsu's thresholding method explained in Chapter 3 (section 3.7). The grey-level reference patch image was then segmented using the threshold value so that the pixels of values more than the threshold value were assigned the intensity value 1 (white) and pixels with values less than the threshold value were assigned the pixels value 0 (black). Figure 4.22(d) shows the binary image resulting from Otsu's thresholding based segmentation where the reference patch was segmented from the rest of the image.

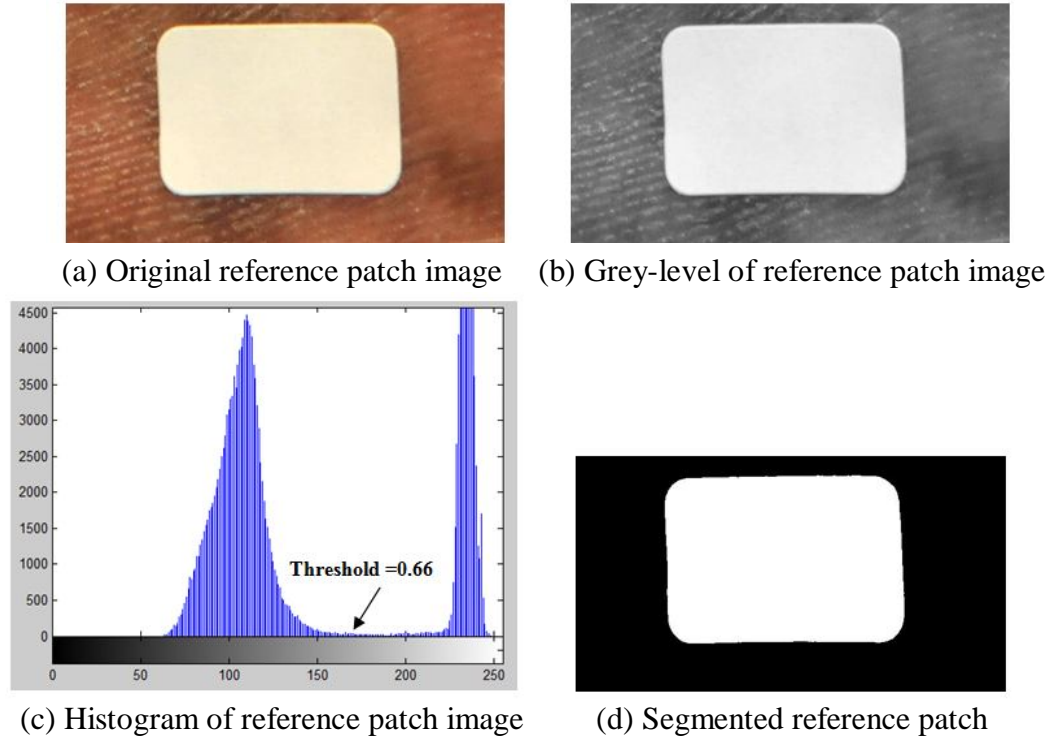


Figure 4.22: Segmentation of reference patch for area measurements

The number of white pixels within the segmented reference patch and the number of white pixels within the detected region of the granulation tissue were calculated for each ulcer image. The area of the detected granulation tissue can then be calculated as follows:

$$Area = \left(\frac{ref_area}{num_pixels_{ref}} \right) * num_pixels_{granulation} \quad (4.5)$$

where ref_area is the area of the reference patch ($9 \times 13 \text{ mm} = 117 \text{ mm}^2$, or $3 \times 6 \text{ cm} = 360 \text{ mm}^2$), num_pixels_{ref} is the number of white pixels of the segmented reference patch and $num_pixels_{granulation}$ is the number of white pixels of the detected granulation region.

Dividing the area of the reference patch over the number of the pixels contained within the reference patch for each image gave the area per unit pixel for that particular image. Multiplying the number of granulation pixels with the area per unit pixel gave the surface area of the detected granulation tissue region. Monitoring the

change in the surface area of the granulation tissue reflected on the progression of the ulcer healing and treatment efficacy. The surface area of the detected granulation tissue could be calculated using Equation (4.5) for all of the seventy-five ulcer images included in this study.

4.8 Summary

This research work aims to develop a system that is able to detect regions of granulation tissue on the surface of wounds and utilize them to provide an objective assessment of the severity condition and healing status of chronic ulcers. Identifying and quantifying the amount of the detected granulation tissue gives an indication of the healing progression which reflects on the efficacy of the ulcer management.

For this study, seventy-five colour images of chronic ulcers were acquired at Hospital Kuala Lumpur. The ulcers included in the study were of different types and aetiologies and contained a mixture of several ulcer tissues. After obtaining the patients' consent in participating in the study, images of the ulcers were acquired under controlled acquisition settings using a high resolution digital camera. A white reference sticker was also included in the image and used to correct the undesired colour shifts using the white point estimation algorithm. The ulcer region, which included the ulcer and some of the surrounding skin, was manually selected from the colour corrected images.

The ulcer region images were input to the granulation detection system developed in this study. The system was designed to detect regions of granulation tissue based on the distribution of pigment haemoglobin on the ulcer surfaces which reflected the existence of the granulation tissue. The approach was to apply data transformation utilising the independent component analysis to extract source grey-level images that show the distribution of pigment haemoglobin. The extracted haemoglobin images showed regions of haemoglobin distribution that reflected the regions of the granulation tissue on the ulcer's surface. The extracted source images may have contained salt and pepper type noise caused by unavoidable specular reflection during

the image acquisition. Hence, a median filter was utilised to remove the any noise from the images to ensure better detection of the granulation regions.

The extracted haemoglobin images identified the regions of the granulation tissue which appeared with a distinctive range of intensity values that could clearly be contrasted and separated from the rest of the image. Clustering-based segmentation was employed in this study to segment the identified regions of the granulation tissue on extracted haemoglobin images. Fuzzy c-means clustering was applied to the haemoglobin images to classify the granulation regions based on their range of intensity values. The classified granulation regions were then segmented from the rest of the images accordingly. The algorithm was applied iteratively with the number of clusters k varying from $k = 2$ till $k = 10$. The optimum number of clusters was then chosen based on the minimum segmentation difference error between the segmented granulation regions obtained from the developed system and the dermatologists' traced granulation regions at each iteration step.

The algorithm ultimately produced binary images that contained segmented regions of the granulation tissue. The detected and segmented regions of the granulation tissue from the ulcer images could be utilised as a measure for the ulcer healing progression. The amount of the detected granulation tissue, in terms of surface area, can be measured during consecutive visits throughout the course of treatment and used to monitor the healing progression. If the current treatment is effective, the amount of detected granulation tissue should increase throughout the course of the treatment.

CHAPTER 5

RESULTS AND ANALYSIS

5.1 Introduction

This chapter presents the main results and findings of this research work. The performance and limitations of the developed granulation tissue detection systems was investigated and is analysed in section 5.2. This was performed by first developing ulcer tissue reference images utilising the sample images of ulcer tissues taken from the ulcer images collected for this study. Then, the granulation detection system was applied on these images and subsequently the sensitivity, specificity and accuracy of the system was analysed accordingly. The application of the developed granulation detection system is explored by utilising the system to detect the regions of granulation tissues on seventy-five ulcer images in section 5.3. The results obtained are discussed and analysed using the granulation assessment reference images. A general discussion and summary of the overall results obtained is presented in section 5.4.

5.2 Performance Analysis of Granulation Tissue Detection Algorithms

The main objective of this research work is to identify regions of healthy granulation tissue on ulcers surfaces as a measure of the healing progression. This was performed by extracting the grey level images that showed the distribution of the haemoglobin on the ulcers' surfaces in colour images of the chronic ulcers. The identified regions of the haemoglobin distribution, or granulation tissue regions, were then segmented from the rest of the ulcer image and their surface area was measured to provide an objective measure of the ulcer healing progression.

However, before applying the developed granulation detection algorithms on real ulcer images, it was important to investigate the algorithms' performance and limitations. Ulcer tissue reference images that contained the regions of ulcer tissues were developed to investigate the performance of the developed algorithms.

5.2.1 Ulcer Tissue Sample Images

A representative set of tissue sample images was required to create the ulcer tissues reference images that contained the regions of the ulcer tissues. Tissue sample images were selected from the ulcer images collected in this study. There were a few points that needed to be considered when selecting the tissue samples from the ulcer images:

- a) The sample image had to represent a pure tissue type that was not mixed with any other type of tissues on the ulcer's surface.
- b) The sample image had to not include any shadows or specular reflections that might have distorted the data and caused a huge variation in the intensity values distribution.
- c) The sample images had to be selected after colour shifts corrections had been performed on the acquired ulcer images.

Three types of ulcer tissues were included in the tissue reference images, granulation tissue, slough and necrotic tissue. Epithelial tissue was not included as it represents later stages of ulcer healing and therefore was not included in the dataset of the ulcer images collected for this study. Skin sample images were also included to represent the skin surrounding the ulcer.

Tissue types were identified on the acquired ulcer images with the help of dermatologists at Hospital Kuala Lumpur. Then, the sample images are manually selected from ulcer images. Three sample images of the same tissue type were selected from one image and then combined to form one tissue sample image. For each combined tissue sample image, the Red, Green and Blue channel images were identified as the three main data vectors of the tissue sample image. To ensure further

accuracy, outliers were identified from the Red, Green and Blue channels data vectors for each combined tissue sample image and they were later removed. Outliers generally are data points whose values differ significantly from the rest of the data within the sample and affect the mean and standard deviation of the sample. In reference to the tissue samples images selected in this study, the outliers could have been a few random pixels of specular reflections, shadow or mixed tissues that were accidentally included within the sample images. Identifying and removing these outlier pixels was important before creating the tissue images.

The outliers were identified using the concept of box plots. Box plots are graphical means to display groups of numerical data and indicate any outliers within a sample, if any. Figure 5.1 shows a diagram illustrating the concept of box plots. As can be seen from the figure, the box plot consists of a box extending from the first quartile (Q1) which represents 25% of the data in the sample to the third quartile (Q3) which represents 75% of the data. The length of the box is called the inter-quartile range (IQR) and is defined as $IQR = |Q3 - Q1|$. The red line within the box indicates the median (M) of the sample. The lower and upper inner fences are defined as $|Q1 - 1.5 IQR|$ and $|Q3 + 1.5 IQR|$. The whiskers of the box plot extend to the extreme data within the inner fences. Data points located outside the inner fences are considered outliers in the sample [80].

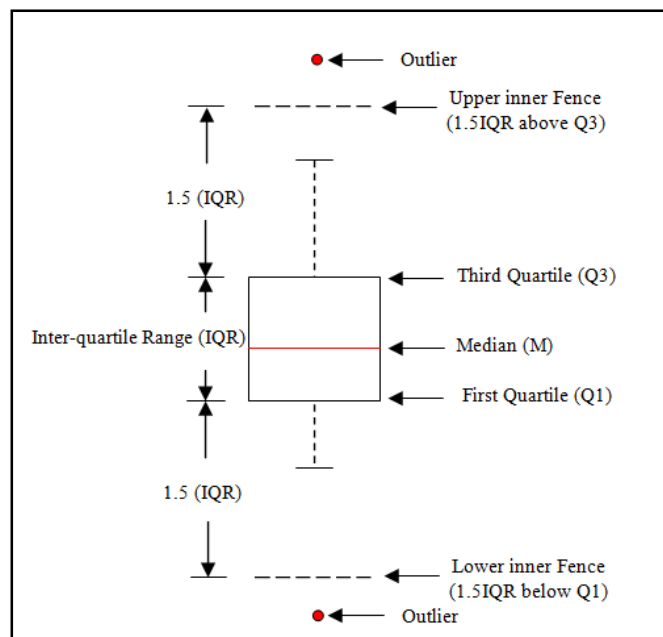


Figure 5.1: A schematic diagram illustrating a box plot with detected outliers

One of the advantages of using box plots is that they indicate the degree of dispersion in the data and identify outliers without making any assumptions of the underlying statistical distribution of the sample. In this study, the pixel distribution of the selected tissue sample images did not assume a normal distribution and hence the IQR was a more robust estimate of the spread of the data than the standard deviation, and more representative of the outlier detection. In the selected tissue sample images for this study, most of the outliers identified were random pixels of mixed tissues that were accidentally included within the sample images.

The selected tissue sample images and total number of pixels of each tissue type after identifying and removing the outliers are specified in Table 5.1. The variation in the number of sample images and total pixels was due to the lack of images that contained regions of pure tissues samples, especially slough and necrotic tissues. Most of the acquired ulcer images for this study contained a mixture of at least two types of tissues especially slough and granulation tissues respectively.

Table 5.1: Ulcer tissue sample images and total number of pixels selected

Tissue Type	Number of Sample Images	Total Number of Pixels
Granulation Tissue	10 Sample Images	1258 Pixels
Slough Tissue	4 Sample Images	406 Pixels
Necrotic Tissue	3 Sample Images	209 Pixels
Skin Tissue	5 Sample Images	4218 Pixels

For each type of tissues (granulation, slough, necrotic and skin tissues), pixels from Red, Green and Blue channels of all the sample images were collected to obtain its distribution. Figure 5.2, Figure 5.3, Figure 5.4, and Figure 5.5 show the obtained overall distribution of the Red, Green and Blue channels pixels of granulation, slough, necrotic and skin tissues respectively.

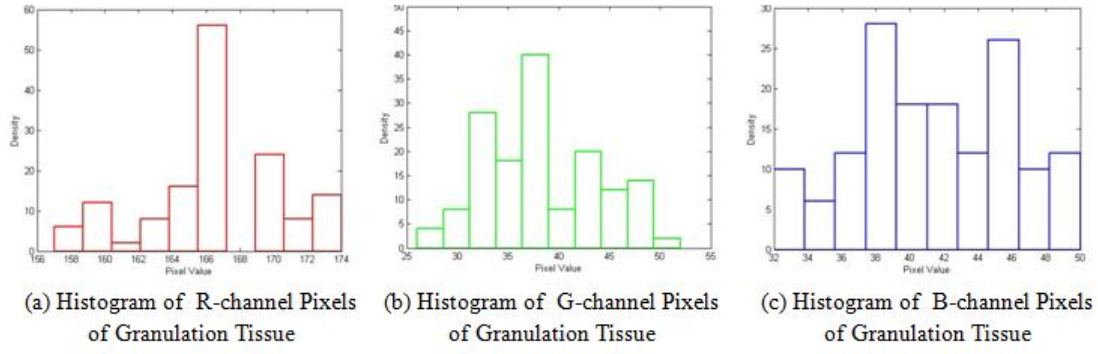


Figure 5.2: Distributions of Red, Green and Blue channels pixels of granulation tissue

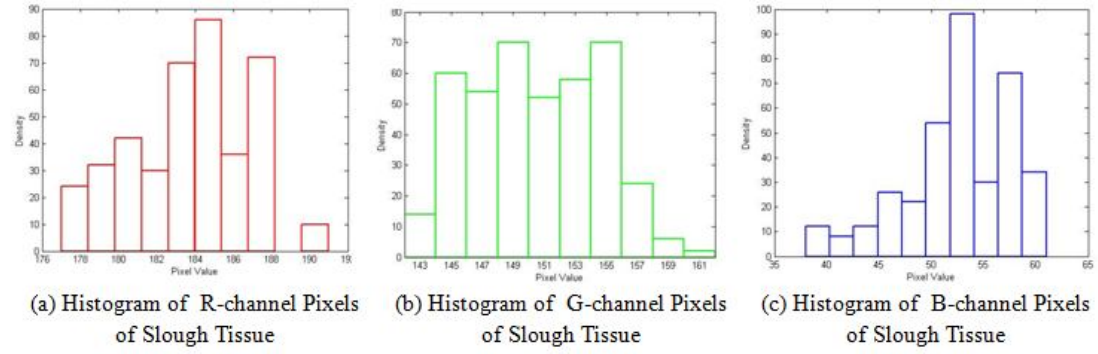


Figure 5.3: Distributions of Red, Green and Blue channels pixels of slough tissue

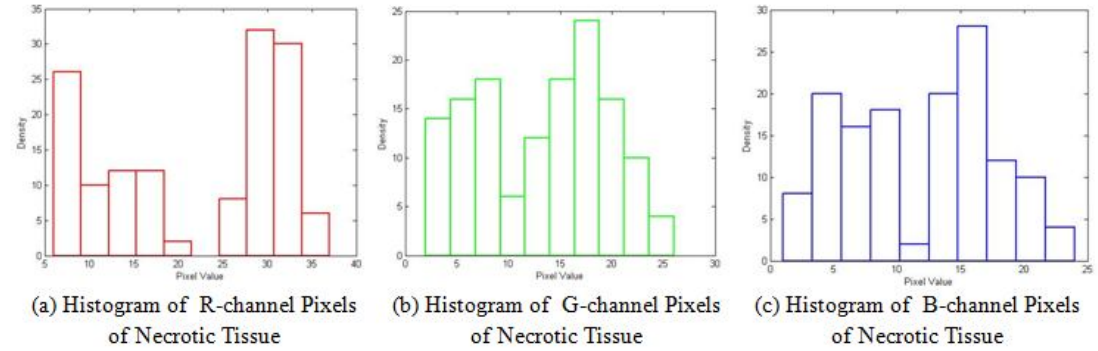


Figure 5.4: Distributions of Red, Green and Blue channels pixels of necrotic tissue

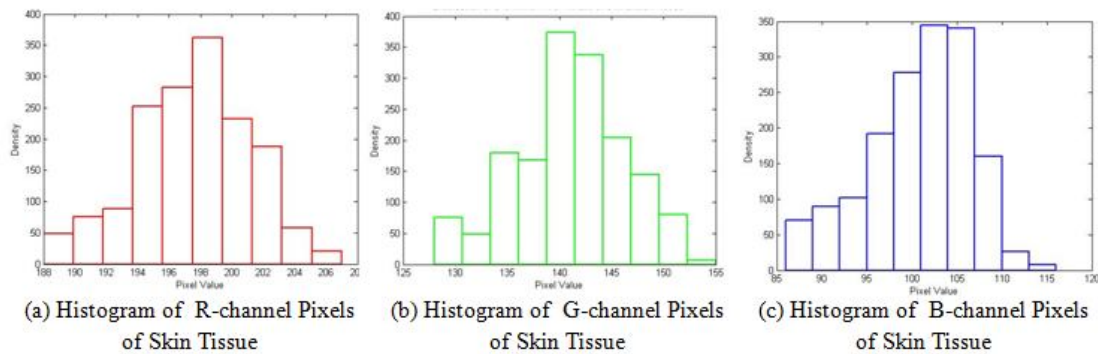


Figure 5.5: Distributions of Red, Green and Blue channels pixels of skin tissue

The probability density functions (PDFs) of the pixel distribution of the Red, Green and Blue channels pixels of granulation, slough, necrotic and skin tissues were computed and utilized to create the ulcer tissue image. Based on the PDFs of the pixel distribution of the Red, Green and Blue channels pixels of all four tissues sample images: granulation, slough, necrotic and skin, image patches were created to represent each type of tissue. For each tissue image patch, the pixels values were selected based on the Red, Green and Blue vectors and their distribution was selected from the PDF of the tissue accordingly. For example, to create the R-channel vector of the granulation tissue image patch, the following steps are followed:

- a) Select the size of the image patch as 50x50 pixels, 100x100 pixels or 200x200 pixels, and so on, depending on the size of the ulcer tissue reference that needs to be developed.
- b) Multiply the size of the image patch with the computed PDFs for the R-channel vector of the granulation tissue to determine the required number of pixels of each specific intensity value from the R-channel vector.
- c) Create a new R-channel data vector of the same size as the image patch that contains a mixture of all pixel values of the original R-channel distributed according to the PDFs computed previously.
- d) Repeat steps 1- 3 for the remaining G-channel and B-channel vectors to create the granulation tissue image patch.

Figure 5.6 shows 200x200 pixel sized image patches of skin, granulation, slough and necrotic tissues created utilising the PDFs of the Red, Green and Blue channels of each tissue type respectively.

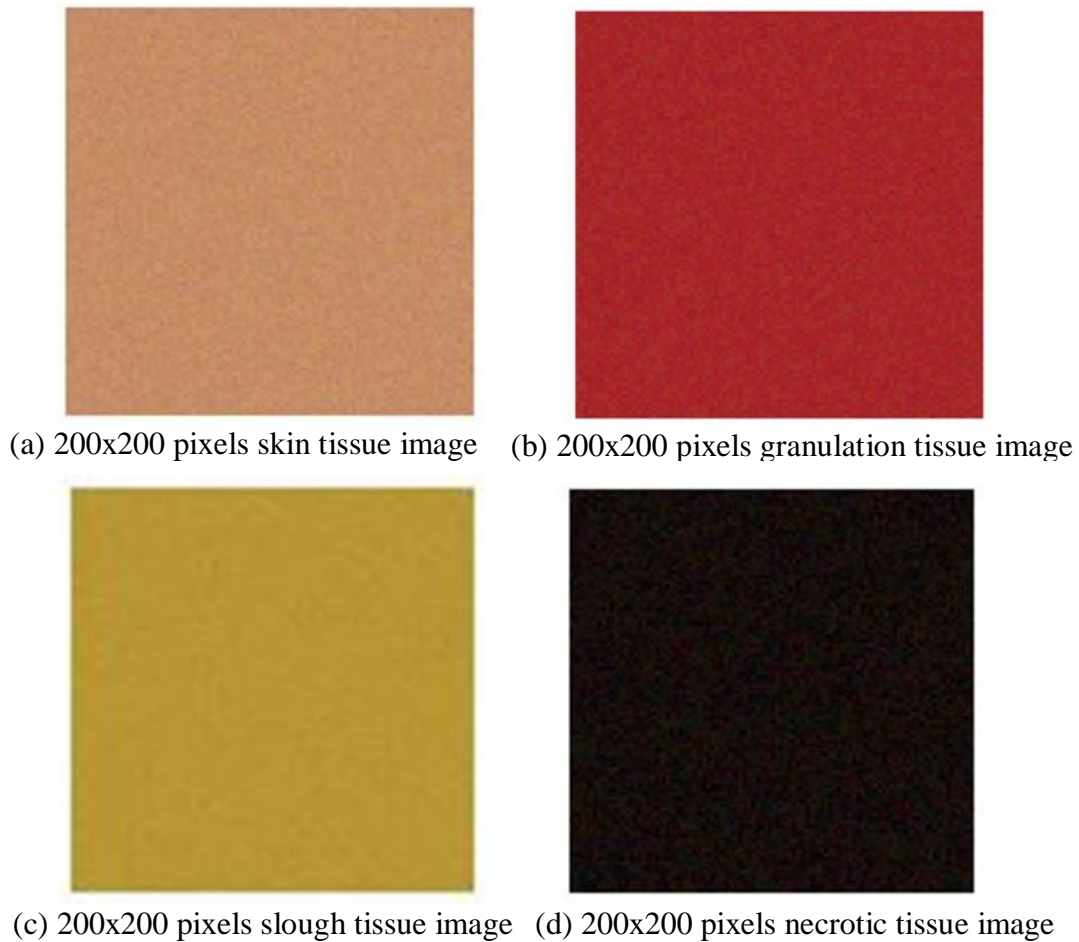


Figure 5.6: Image patches of size 200x200 pixels of skin, granulation, slough and necrotic tissues

5.2.2 Ulcer Tissue Image

In analysing the algorithm performance, three main aspects of the performance analysis needed to be investigated:

- a) The developed algorithm had to be able to clearly detect and distinguish granulation tissue from the rest of the ulcer tissues.
- b) The developed algorithm had to be able to detect regions of granulation tissue of different sizes in pixel units.
- c) The developed algorithm had to be able to detect regions of granulation tissue in images corrupted by white Gaussian noise.

The ulcer tissue image was designed according to the above criteria utilising the tissue image patches developed in the previous section. The developed ulcer tissue image is shown in Figure 5.7. It consisted of a 250x250 pixel skin image that includes slough tissue and necrotic tissue regions of a size of 50x100 pixels accordingly. Two sets of granulation tissue regions were included within the tissues regions. The first set was included between the skin and slough tissues while the second set was included within the skin and necrotic tissues. This was necessary to test the ability of the algorithm to detect and distinguish granulation tissue from the rest of the tissues types. Furthermore, each set of granulation tissue regions consisted of eight patches of sizes 30x30, 20x20, 10x10, 5x5, 4x4, 3x3, 2x2, and 1x1 pixels respectively. This in turn, was required to test the ability of the algorithm to detect granulation tissue regions of different sizes in pixel units.

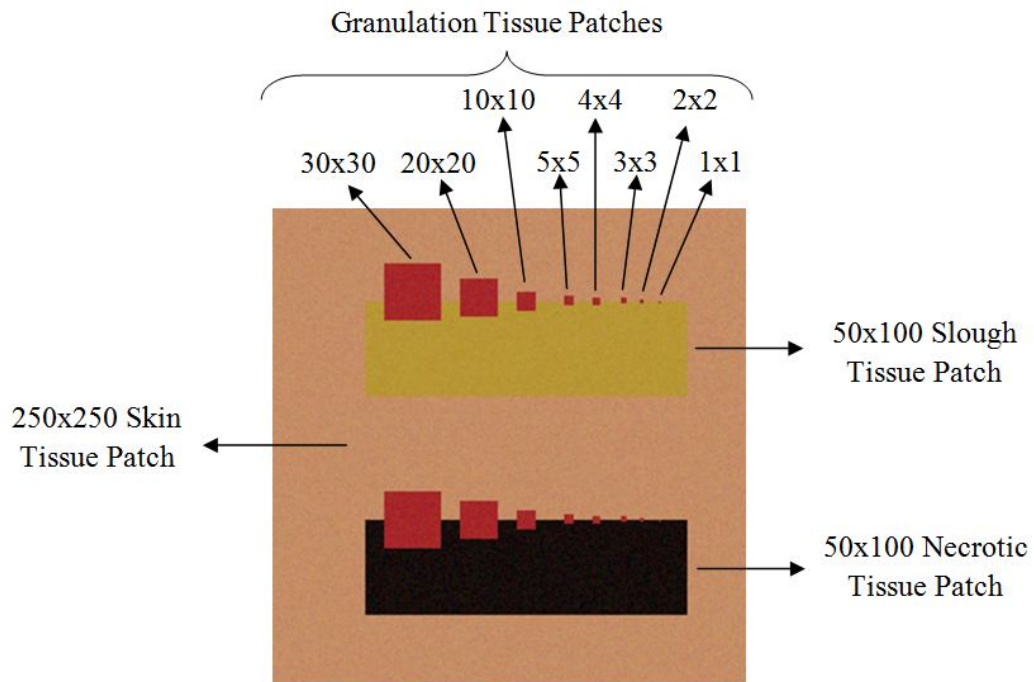


Figure 5.7: Ulcer tissue image

Granulation tissue regions in the ulcer tissue image were manually segmented from the rest of the image to create a binary reference image as shown in Figure 5.8. In this binary image, referred to as a granulation tissue reference binary image, the granulation regions were represented with white pixels (pixels of value 1) while the rest of the image was represented with black pixels (pixels with value 0). The

granulation tissue reference binary image was used to analyse the performance of the developed granulation detection algorithm as it is shown later in section 5.3.2.

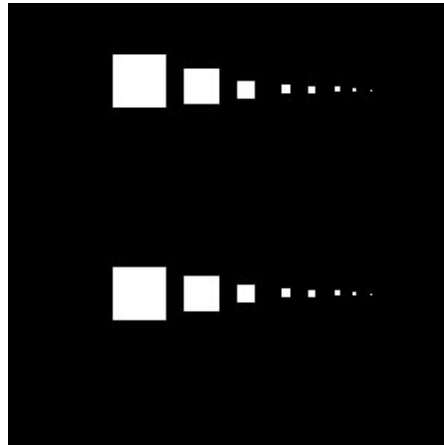


Figure 5.8: Granulation tissue reference binary image

5.2.3 Detection of Granulation Tissue Patches

The data transformation algorithms discussed in Chapter 4 (section 4.5) were applied on the ulcer tissue image developed in the previous section to extract the haemoglobin image. The extracted haemoglobin image represented patches of granulation tissue with intensity value range that could be contrasted from the rest of the image. Figure 5.9 shows the extracted haemoglobin image from the ulcer tissue image. It can be seen that the two sets of granulation tissue patches in all sizes are clearly identified with a distinctive low intensity value range (dark shade) that can be segmented from the rest of the image.

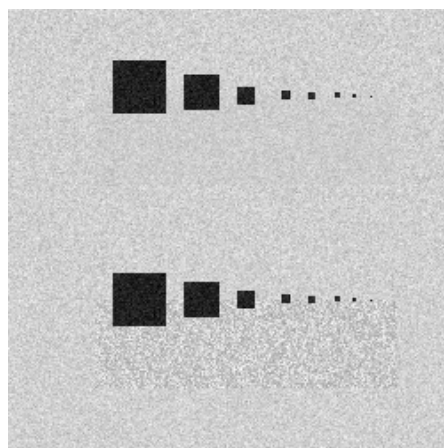
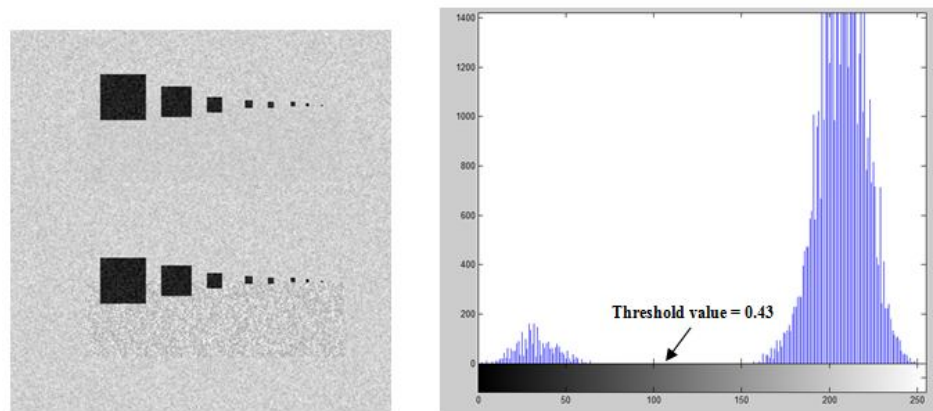
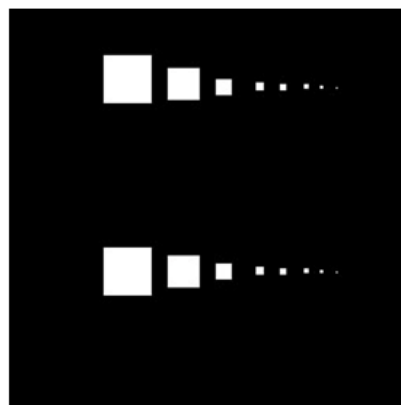


Figure 5.9: Extracted haemoglobin image from ulcer tissue image

For further analysis of the algorithm performance, the identified granulation tissue patches needed to be segmented from the rest of the image. Figure 5.10 (a) shows the extracted haemoglobin image and Figure 5.10 (b) shows its bimodal histogram which clearly indicates two distinctive regions, the identified granulation patches (the dark region) and rest of the image (the bright region). A threshold value of 0.43 was determined using Otsu's thresholding method explained in Chapter 3 (section 3.7). The extracted haemoglobin image was then segmented using the threshold value so that the pixels with intensity values less than the threshold value were assigned the intensity value 1 (white) and the pixels with an intensity value higher than the threshold value were assigned the pixel value 0 (black). Figure 5.10 (c) shows the binary image resulting from Otsu's thresholding based segmentation where the granulation patches were segmented from the rest of the image.



(a) Extracted haemoglobin image (b) Histogram of extracted haemoglobin image



(c) Binary image obtained from Otsu's based segmentation of haemoglobin image

Figure 5.10: Otsu's thresholding based segmentation of haemoglobin image extracted from ulcer tissue image

5.2.4 White Gaussian Noise Models

Real images are normally corrupted with some degree of white noise affecting the resolution and quality of the image. The more noise added to the image, the more degraded the image. White Gaussian noise images were generated and added to the ulcer tissue image to simulate and test the granulation detection system's robustness to noise before testing with real ulcer images.

Let I be the ulcer tissue image and N be the developed white Gaussian noise image. The ulcer tissue reference image R would consist of:

$$R = I + N \quad (5.1)$$

Image N is a noise image simulating white Gaussian noise defined as follows:

$$N(i; \mu, \sigma) = \frac{1}{\sigma\sqrt{2\pi}} e^{-\frac{(i-\mu)^2}{2\sigma^2}} \quad (5.2)$$

where i refers to the i^{th} pixel of the noise image, and μ and σ are the mean and standard deviation of the Gaussian distribution, respectively.

A common way of measuring the effect of adding noise to a signal is the signal to noise ratio (SNR) which is calculated as follows:

$$SNR(dB) = 10 \log \left(\frac{P_{Signal}}{P_{Noise}} \right) = 20 \log \left(\frac{A_{Signal}}{A_{Noise}} \right) \quad (5.3)$$

where P is the power and A is the RMS (root mean square) value of the signal.

Assume the signal x , the RMS value of the signal relates to its mean and standard deviation as follows:

$$A = x_{RMS} = \mu_x^2 + \sigma_x^2 \quad (5.4)$$

where x_{RMS} is the RMS value of x , μ_x is the mean value of x , and σ_x is the standard deviation of x . Hence Equation (5.4) can be written as follows:

$$SNR(dB) = 20 \log \left(\sqrt{\frac{\mu_{Signal}^2 + \sigma_{Signal}^2}{\mu_{Noise}^2 + \sigma_{Noise}^2}} \right) \quad (5.5)$$

If x is a zero-mean, the RMS value of x is equal to the standard deviation, Equation (5.5) can be written as:

$$SNR(dB) = 20 \log \left(\sqrt{\frac{\sigma_{Signal}^2}{\sigma_{Noise}^2}} \right) = 20 \log \left(\sqrt{\left(\frac{\sigma_{Signal}}{\sigma_{Noise}} \right)^2} \right) = 20 \log \left(\frac{\sigma_{Signal}}{\sigma_{Noise}} \right) \quad (5.6)$$

Using Equation (5.6), noise images could be generated with specified noise variance values and added to the ulcer tissue image to create the ulcer tissue reference images with varying noise levels. The developed ulcer tissue image had a constant variance value of $\sigma_{Signal} = 59.89$. In this work, twenty four ulcer tissue reference images are created with SNR values ranging from 36dB, which was the highest SNR level associated with the ulcer tissue reference image which resulted by adding a noise image with a variance $\sigma_{Noise} = 1$, until 1dB, which was the lowest SNR level which resulted by adding a noise image of a variance $\sigma_{Noise} = 51$. Table 5.2 lists the variance values of the ulcer tissue image, the variance values of the noise images added and the corresponding SNR value of the output ulcer tissue reference images accordingly.

Table 5.2: Signal to Noise Ratio (SNR) values of ulcer tissue reference images

No.	Image Variance (σ_{Signal})	Noise Variance (σ_{Noise})	SNR (dB)	No.	Image Variance (σ_{Signal})	Noise Variance (σ_{Noise})	SNR (dB)
1	59.89	1	36	13	59.89	15	12
2	59.89	2	30	14	59.89	16	11
3	59.89	3	26	15	59.89	18	10
4	59.89	4	24	16	59.89	21	9
5	59.89	5	22	17	59.89	24	8
6	59.89	6	20	18	59.89	28	7
7	59.89	7	19	19	59.89	30	6
8	59.89	8	17	20	59.89	32	5
9	59.89	9	16	21	59.89	36	4
10	59.89	11	15	22	59.89	41	3
11	59.89	12	14	23	59.89	46	2
12	59.89	13	13	24	59.89	51	1

Figure 5.11 shows an example of one of the developed ulcer tissue reference images. Figure 5.11 (a) shows the original ulcer tissue image while Figure 5.11 (b) shows the ulcer tissue reference image which resulted by adding a noise image with

variance of $\sigma_{Noise} = 18$. The corresponding SNR of the image was calculated and found to be about 10dB as indicated in Table 5.2. The performance of the developed algorithms for detecting regions of granulation tissue were investigated using the ulcer tissue reference images created with varying Gaussian white noise levels and are discussed in the following section.

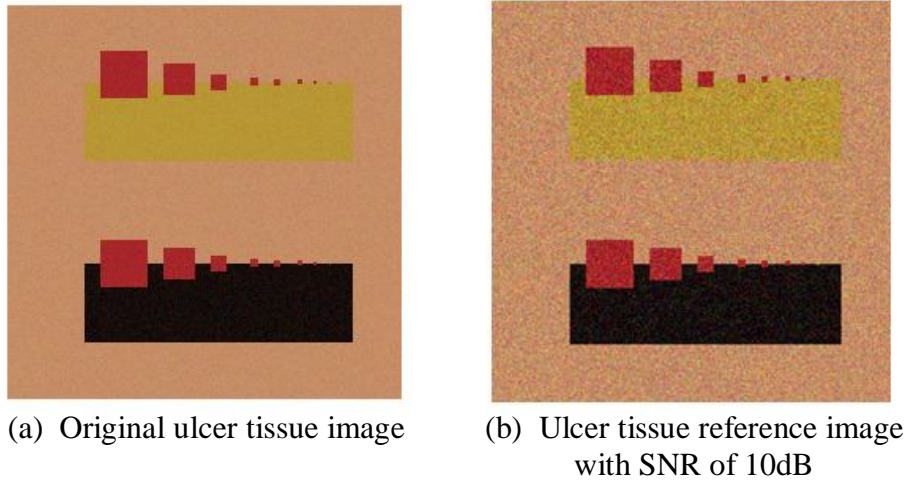


Figure 5.11: Developed ulcer tissue reference image with SNR of 10dB

5.2.5 System Performance Measures

The ulcer tissue reference images were created to test the algorithm performance in detecting regions of granulation tissue of different sizes and clearly distinguishing them from the rest of the ulcer tissues in images corrupted with Gaussian white noise. The developed system for identifying and segmenting granulation tissue patches and Otsu's thresholding algorithms were applied on the twenty-four ulcer tissues reference images created with varying Gaussian white noise levels. When applying noise to the ulcer tissue reference images accordingly, some granulation pixels might have been detected as non-granulation pixels and vice versa. Hence, the algorithm performance could be further investigated comparing the resulted binary images from the algorithms with the granulation tissue reference binary image shown in Figure 5.10.

For each binary image which resulted from the algorithms, the pixels could be divided into true positives (TP), true negatives (TN), false negatives (FN) and false positives (FP). True positives (TP) were granulation pixels that are correctly detected

as granulation, false positives (FP) were non-granulation pixels that are incorrectly detected as granulation, true negatives (TN) were non-granulation pixels that were correctly detected as non-granulation, and false negatives (FN) are granulation pixels that are incorrectly detected as non-granulation. It is useful to note that the total number of granulation pixels of all the granulation patches (true positives) in the granulation tissue reference binary image was 2910 while the rest of the pixels that corresponds to non-granulation pixels were 59590.

Figure 5.12 shows the number of granulation pixels which were detected as non-granulations (false negatives) for all of the twenty-four ulcer tissues reference images. It was noted that at the reference image with the SNR level of 17dB, the number of false negative pixels increased slowly till reaching the SNR level of 14dB. It then increased rapidly above 100 pixels as more noise was added to the image. The maximum number of detected false negatives was 355 out of 2910 that occurred at the SNR level of 1dB.

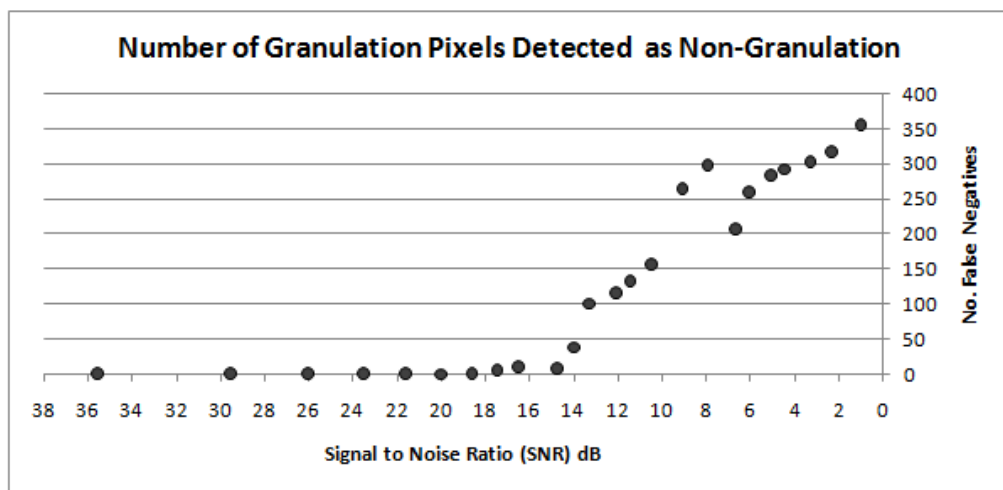


Figure 5.12: Number of granulation pixels detected as non-granulation for all ulcer tissue reference images

Figure 5.13 shows the number of non-granulation pixels that were wrongly detected as granulation (false positives) for all of the twenty four ulcer tissue reference images. It was noted that the number of detected false positives generally increased for the reference image with SNR levels of 16dB and below. At SNR levels of 16-10dB, the number of false positives was less than 1000 pixels. It increased rapidly beyond 1000 pixels for SNR levels of 9dB and below. The maximum number

of detected false positives was 26714 out of 59590 which occurred at the SNR level of 1dB.

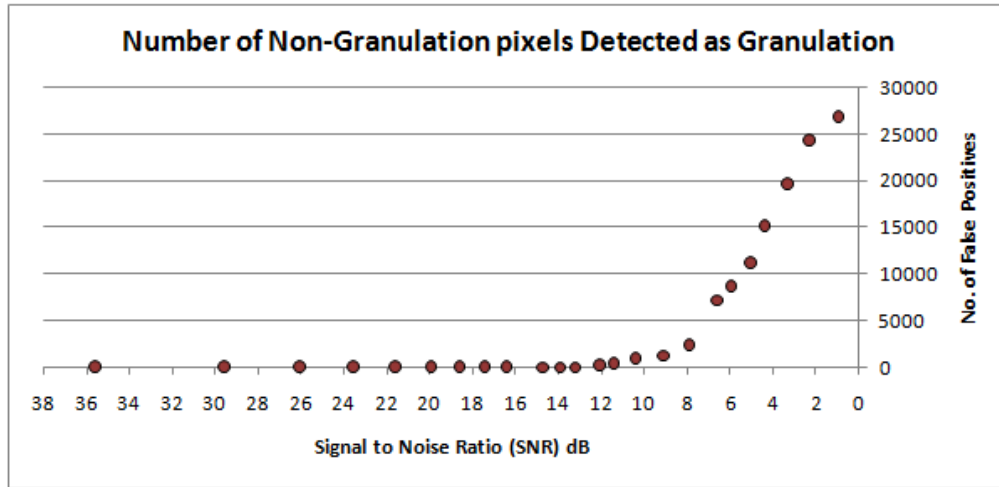


Figure 5.13: Number of non-granulation pixels detected as granulation for all ulcer tissue reference images

Statistical measures such as sensitivity, specificity and accuracy were employed to analyse the performance of the granulation detection algorithm. Sensitivity and specificity are statistical measures used to analyse the performance of a binary classification test. The sensitivity measured the proportion of the true positives (granulation pixels) that were correctly identified as such (detected as white pixels) [81], [82]. Hence the value of the sensitivity represented the probability that the algorithm could correctly identify granulation pixels in the image. Sensitivity was calculated as follows:

$$Sensitivity = \frac{TP}{TP + FN} \quad (5.7)$$

Since sensitivity was calculated from the population of true positives, a negative result in a highly sensitive test was used to rule out the condition [82]. This means if the developed algorithm has a high sensitivity value, the detected black pixels in the image most likely are non-granulation pixels.

The specificity on the other hand measured the proportion of true negatives (non-granulation pixels) that were identified as such (detected as black pixels) [81], [82].

Hence, the value of the specificity represented the probability that the algorithm could correctly identify non-granulation pixels in the image. Specificity was calculated as follows:

$$Specificity = \frac{TN}{TN + FP} \quad (5.8)$$

Since specificity was calculated from the population of true negatives, a positive result in a highly specific test was used to rule in the condition [82]. This means that if the developed algorithm has a high specificity value, the detected white pixels in the image most likely are granulation pixels.

The accuracy was a measure of the proportion of true pixels (both true positives and true negatives)[81]. In other words, accuracy measured how many granulation and non-granulation pixels were correctly identified and detected from all of the pixels in the image.

$$Accuracy = \frac{TP + TN}{TP + FP + FN + TN} \quad (5.9)$$

Figure 5.14 shows the sensitivity, specificity and accuracy values were obtained for all twenty-four ulcer tissue reference images with varying Gaussian white noise levels indicated with SNR levels from the maximum of 36dB down to the minimum of 1dB. From the figure, it is evident that the system detects regions of granulation tissue with high sensitivity, specificity and accuracy for SNR levels above 8dB. Further analysis on the system performance is presented in the next section.

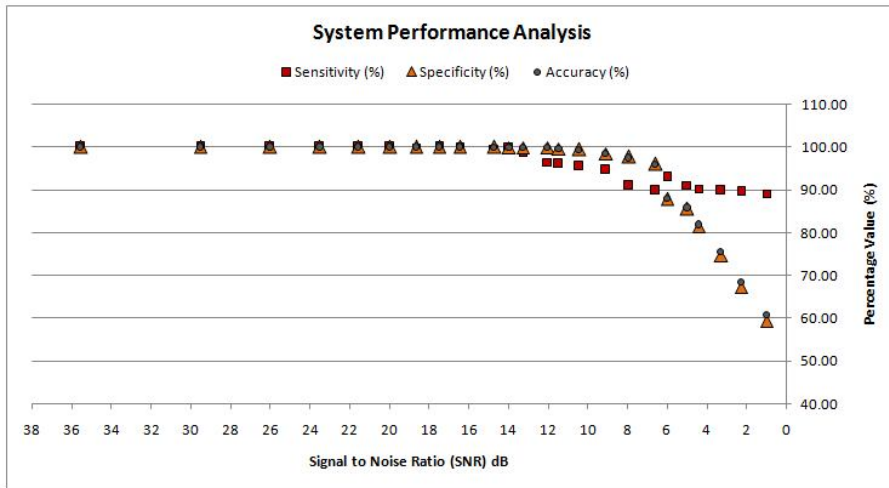


Figure 5.14: Sensitivity, specificity and accuracy of granulation detection system for all ulcer tissue reference images

5.2.6 Discussion and Analysis

Generally, the system retained high performance values (sensitivity, specificity and accuracy) of 99.0% and above for images with SNR levels above 14dB. In particular, the system clearly detected all granulation patches in both slough/skin and necrotic/skin regions with 100% sensitivity, specificity and accuracy for images with SNR levels above 19dB. For the reference image with the SNR level of 20dB which corresponded to the noise variance of about $\sigma = 6$, the system detected one granulation pixel only as non-granulation (false negative), while all other pixels were correctly identified according to the binary reference image as shown in Figure 5.15. This caused an insignificant drop in sensitivity to about 99.97%.

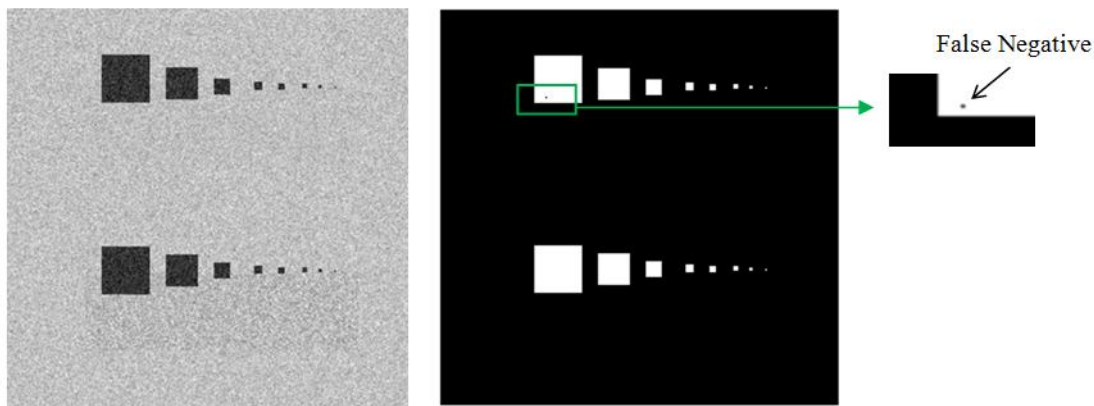


Figure 5.15: Detection of granulation patches in image with SNR of 20 dB

For the reference image with the SNR level of 17dB corresponding to noise variance of $\sigma = 8$, more granulation pixels were detected as non-granulation (false negatives) as shown in Figure 5.16 causing the sensitivity to drop to 99.83%. This also caused an insignificant drop in accuracy to 99.99%.

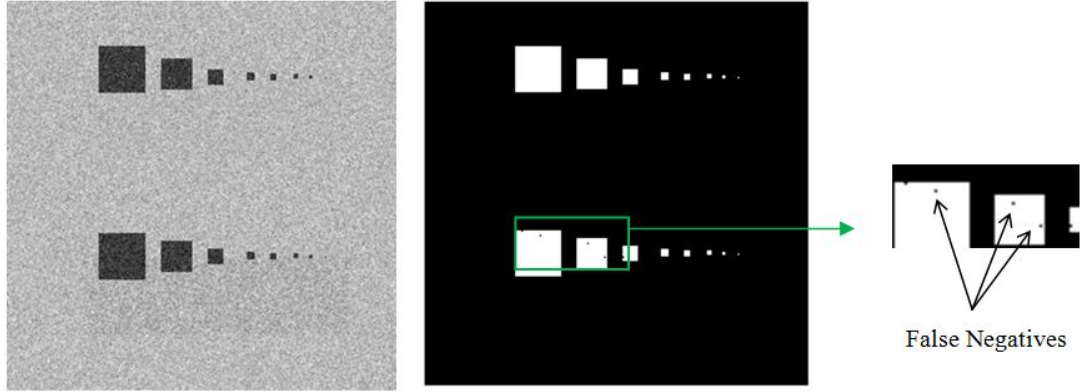


Figure 5.16: Detection of granulation patches in image with SNR of 17dB

For the reference image with the SNR level of 16dB corresponding to noise variance of $\sigma = 9$, one non-granulations pixel was detected as granulation (false positives) and several granulation pixels were detected as non-granulation (false negatives) as shown in Figure 5.17. This caused the sensitivity, specificity and accuracy values to drop slightly to 99.69%, 99.99% and 99.98% respectively.

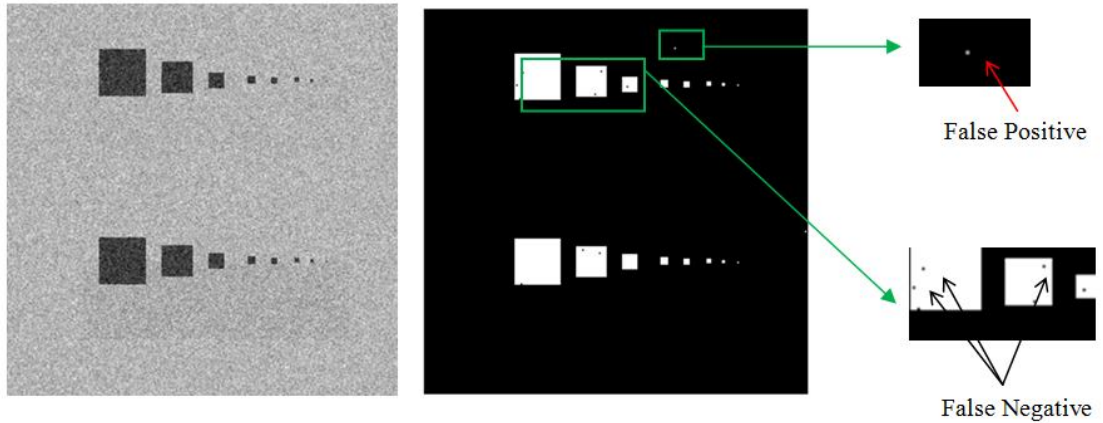


Figure 5.17: Detection of granulation patches in image with SNR of 16dB

For the reference images with the SNR level of 15dB and 14dB which corresponded to the noise variance of $\sigma = 11$ and $\sigma = 12$, respectively, more non-granulations pixels were detected as granulation (false positives) and more granulation pixels were detected as non-granulation (false negatives) as shown in

Figure 5.18 and Figure 5.19. Subsequently, the sensitivity, specificity and accuracy values dropped to 99.76%, 99.93% and 99.92% for the reference image with the SNR of 15dB and 98.66%, 99.97% and 99.91% for the reference image with the SNR of 14dB respectively.

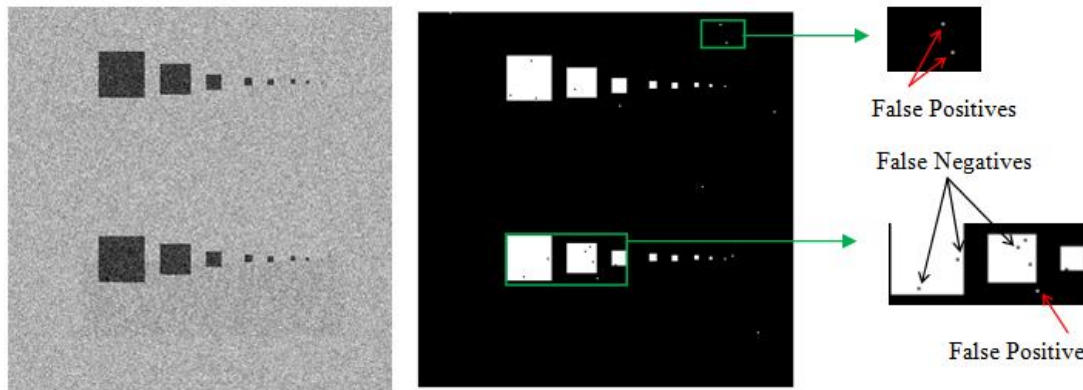


Figure 5.18: Detection of granulation patches in image with SNR of 15dB

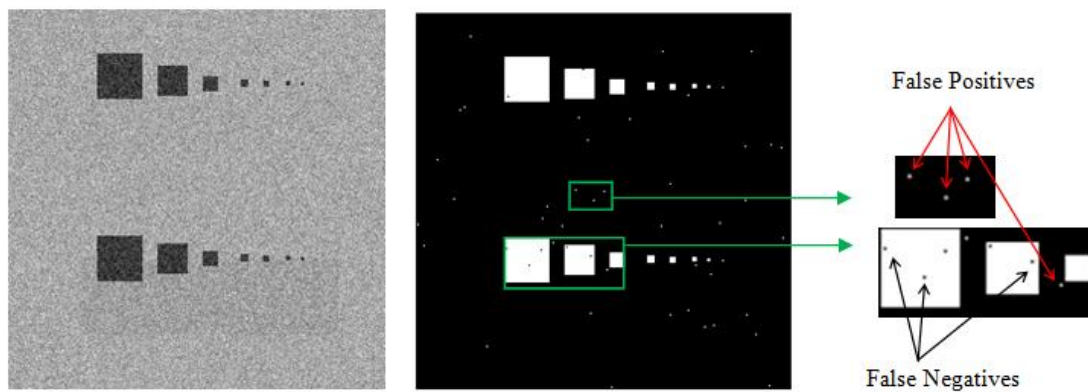


Figure 5.19: Detection of granulation patches in image with SNR of 14dB

When more noise was added to the images, more false negative and false positive pixels were detected and subsequently the performance of the system decreased gradually. The system generally retained performance values of 90% and above in images with SNR levels of 13dB - 8dB. However, the system failed to detect all of the granulation patches as more noise was added. For example, for the image with the SNR level of 12dB, which corresponded to the noise variance of $\sigma = 15$, the 1x1 pixel granulation patch was detected at the skin/slough region but not detected at the necrotic/skin region for the same image. This is illustrated in Figure 5.20 where the 1x1 pixel granulation patch is indicated by the arrows in the slough/skin region on the first row of the granulation patches and the necrotic/skin region at the second row of

the granulation patches. The performance values obtained were 96.05%, 99.68% and 99.52% for sensitivity, specificity and accuracy respectively.

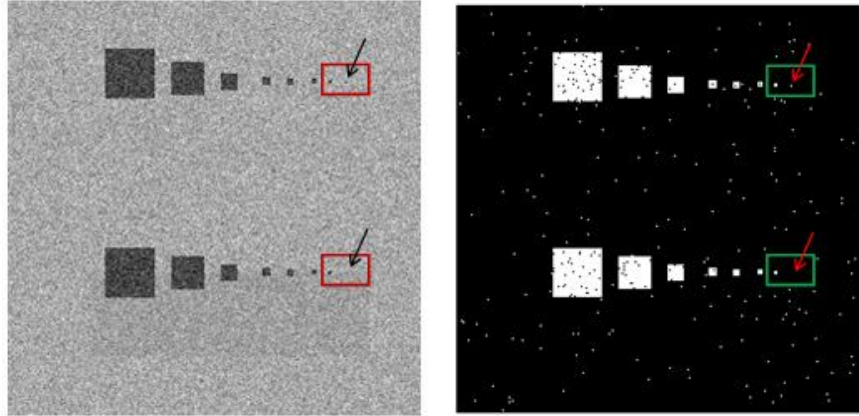


Figure 5.20: Detection of granulation patches in image with SNR of 12dB

For the reference image with the SNR level of 10dB ($\sigma=18$), the 1x1 pixel granulation patch could be distinguished clearly in the extracted haemoglobin image in either the slough/skin or the necrotic/skin regions. However, due to the noise added to the image, those pixels and others were detected as granulation pixels as indicated by the arrows in Figure 5.21. Hence, the system could identify 1x1-pixel granulation patches or distinguish them from Gaussian noise at SNR levels below 10dB. The performance values dropped accordingly to 94.67%, 98.57% and 98.38% for sensitivity, specificity and accuracy respectively.

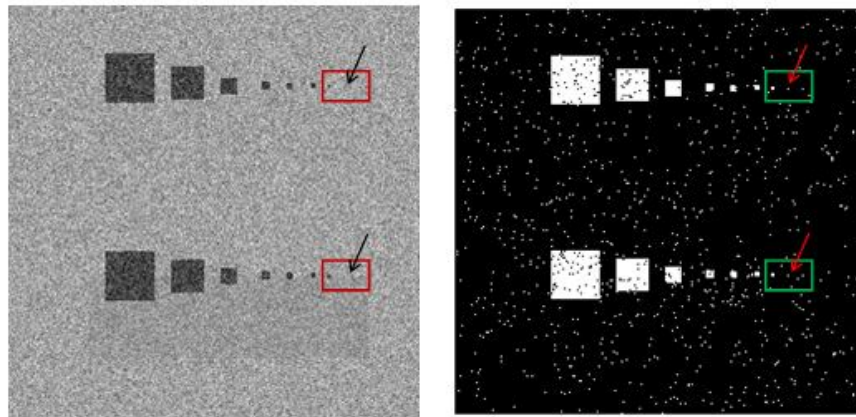


Figure 5.21: Detection of granulation patches in image with SNR of 10dB

For reference the image with the SNR level of 8dB ($\sigma=24$), the 1x1 pixel granulation patch could not be identified by the system in either the slough/skin or the necrotic/skin regions. Furthermore, the 2x2-pixel granulation patch in the

necrotic/skin region was not detected. The arrows in the first row of granulation patches row in Figure 5.22 indicate that the 3x3 pixel and 2x2 pixel granulation patches are detected in the slough/skin region. The arrows in the second row of granulation patch row indicate that only the 3x3 pixel granulation patch was detected in the necrotic/skin region. The performance values dropped accordingly, to 89.79%, 96.13% and 95.83% for sensitivity, specificity and accuracy respectively.

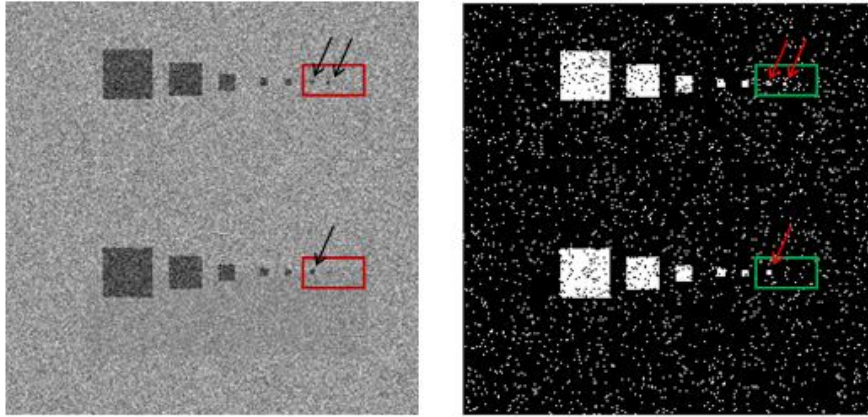


Figure 5.22: Detection of granulation patches in image with SNR of 8dB

Subsequently with increasing the amount of noise added to the image, the image got more corrupted and more false pixels (false negatives and false positives) were identified which affected the detection of the granulation tissue patches. Granulation patches were detected but they were distorted with many false pixels detected due to noise. Figure 5.23 shows the detection of the granulation patches in the image with the SNR level of 6dB which corresponded to the noise variance of $\sigma = 30$ in which the detection of the granulation patches was distorted with image noise, especially for patches of the sizes 4x4, 3x3 and 2x2 accordingly. The performance values dropped to 91.10%, 85.62% and 85.87% for sensitivity, specificity and accuracy respectively. The effect of the noise was more apparent in Figure 5.24 in which granulation patches could not be distinguished from the noise in the images with the SNR levels of 4dB ($\sigma = 36$). The performance values dropped further down to 90.0%, 74.69% and 75.40% for sensitivity, specificity and accuracy respectively.

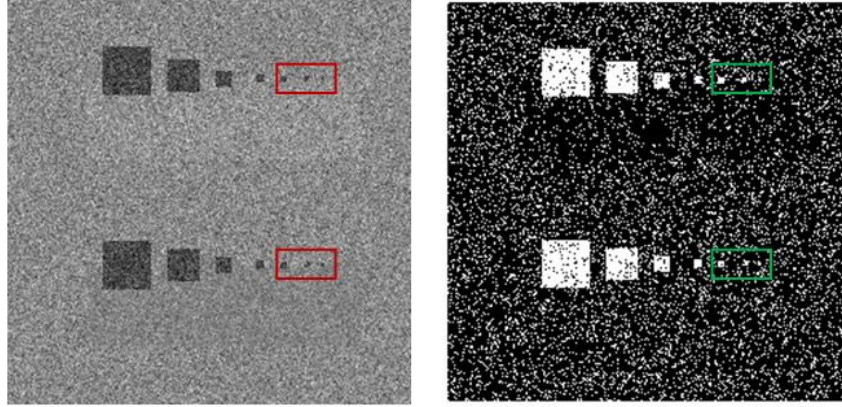


Figure 5.23: Detection of granulation patches in image with SNR of 6dB

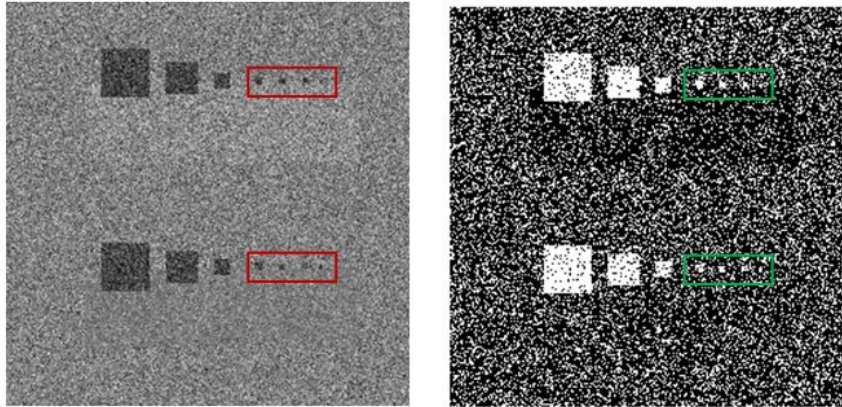


Figure 5.24: Detection of granulation patches in image with SNR of 4dB

It is evident from Figure 5.14 that performance values decreased as more noise was added to the images and more false pixels were detected. It could be noted that the sensitivity values change gradually as more noise was added to the image. For the reference images with SNR values of 36dB to 4dB, the sensitivity values remain above 90% with the maximum value of 100% for images with SNR levels of 36dB to 19dB. Sensitivity dropped to 89.62%, 89.14% and 87.80% for images with SNR 3dB, 2dB and 1dB respectively. This implies that the system can perform with high sensitivity even with degrading noise levels. It also implies that given the existing granulation region, the system has a maximum probability of 100% and minimum probability of 87.80% of identifying the region as granulation tissue under the existence of random white Gaussian noise. On the other hand, specificity values change more rapidly as more noise is added. For reference images with SNR levels of 36dB to 8dB, the specificity values obtained were more than 96.0% with the maximum value of 100% for the images with the SNR levels of 36dB to 16dB.

However, for the image with the SNR level of 7dB, the specificity dropped to 87.83% and remained above 80.0% for the image with the SNR level of 5 dB. It dropped down drastically after that to 74.69%, 67.28%, 59.41% and 55.17% for images with SNR levels of 4dB, 3dB, 2dB and 1dB respectively. This implies that given a existing non-granulation region, the system has a maximum probability of 100% and minimum probability of 55.17% of identifying the region as granulation tissue under the existence of random white Gaussian noise.

From the discussion above, it can be deduced that the developed system is able identify and detect regions of granulation tissue, from the smallest region size of 1x1 pixels and above, in ulcer images corrupted with white Gaussian noise corresponding to SNR levels of more than 12dB with performance values of more than 96.0% sensitivity, 99.6% specificity and 99.5% accuracy. For the images with SNR levels of 12dB and below, some granulation regions, especially of sizes 1x1, 2x2 and 3x3 pixel, might not be detected due to an increased number of detected false pixels for higher noise levels.

5.3 Detection of Granulation in Ulcer Images

As highlighted in Chapter 4 (section 4.3.2), seventy-five images of chronic ulcers were included in this study. The developed granulation detection system was applied on these images to detect the regions of granulation tissue on these ulcers surfaces. First, grey-level images that showed the distribution of haemoglobin on the ulcers' surfaces, referred to as haemoglobin images, were extracted from the colour images of the chronic ulcers using the data transformation algorithms illustrated in Chapter 4 (section 4.5). The identified regions of the haemoglobin distribution, or granulation tissue regions, were then segmented from the haemoglobin images utilising clustering based segmentation algorithms explained in Chapter 4 (section 4.6.2). The surface area of the detected granulation tissue regions was measured to provide an objective measure of the ulcer healing progression.

5.3.1 Optimum Number of Clusters for Clustering-Based Segmentation

The clustering based segmentation algorithms using fuzzy c-means clustering was applied iteratively on each extracted haemoglobin image with the number of clusters k ranging from $k = 2$ till $k = 10$ to determine the optimum number of clusters needed for the segmentation of the granulation tissue as explained in Chapter 4 (section 4.6.3). The segmentation difference error at each k -th iteration step was computed using Equation (4.4) and plotted for all of the ulcer images. The optimum number of clusters was then determined as the cluster number at which the minimum segmentation difference error occurred. Figure 5.25 shows an example of a plot of the segmentation difference error obtained from applying the clustering based segmentation on one ulcer image iteratively for $k = 2$ till $k = 10$. The optimum number of clusters was chosen as $k = 5$ at which the minimum difference error in this case as indicated in Figure 5.25.

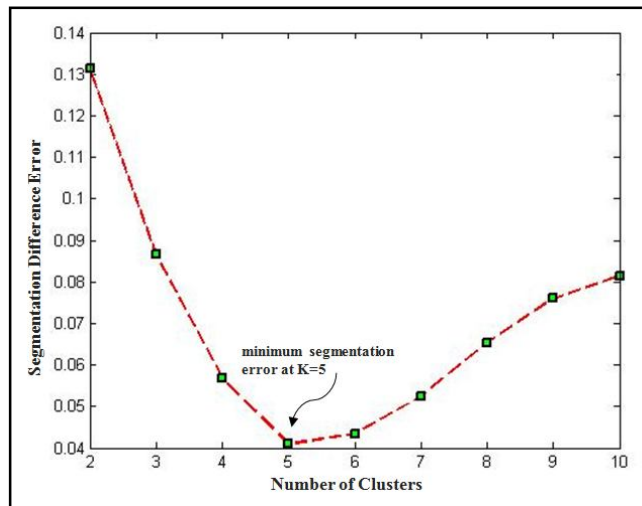


Figure 5.25: A plot of the segmentation difference error obtained from applying the clustering based segmentation on one ulcer image iteratively for $k=2$ till $k=10$

In some cases, the difference error reached a certain value at a specific cluster number and did not change much after that with increasing the cluster number resulting in an L shaped curve as indicated in Figure 5.26. In this case, the optimum number of clusters was chosen to be the cluster number after which the change in the error value between two consecutive cluster numbers was very small and almost constant. This point occurred normally at the knee of the graph as shown in Figure 5.26.

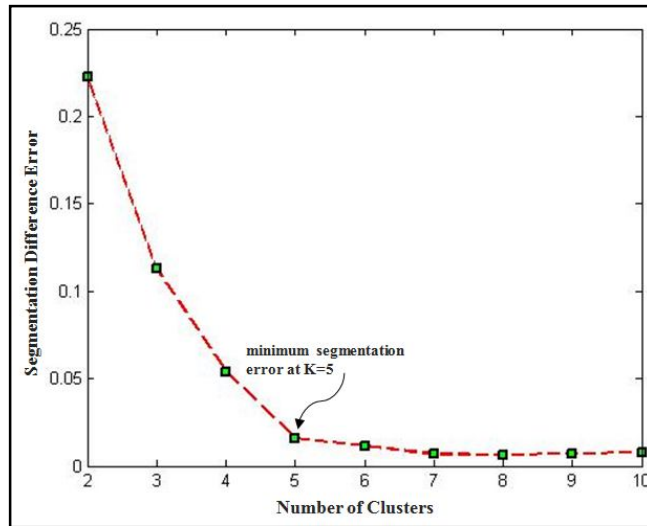


Figure 5.26: A plot of the segmentation difference error obtained from applying the clustering based segmentation on one ulcer image iteratively for $k=2$ till $k=10$

Figure 5.27 shows the minimum segmentation difference error obtained when applying the clustering-based segmentation algorithms for each ulcer image. The figure also indicates the optimum number of clusters at which the minimum segmentation difference error occurred for each ulcer image.

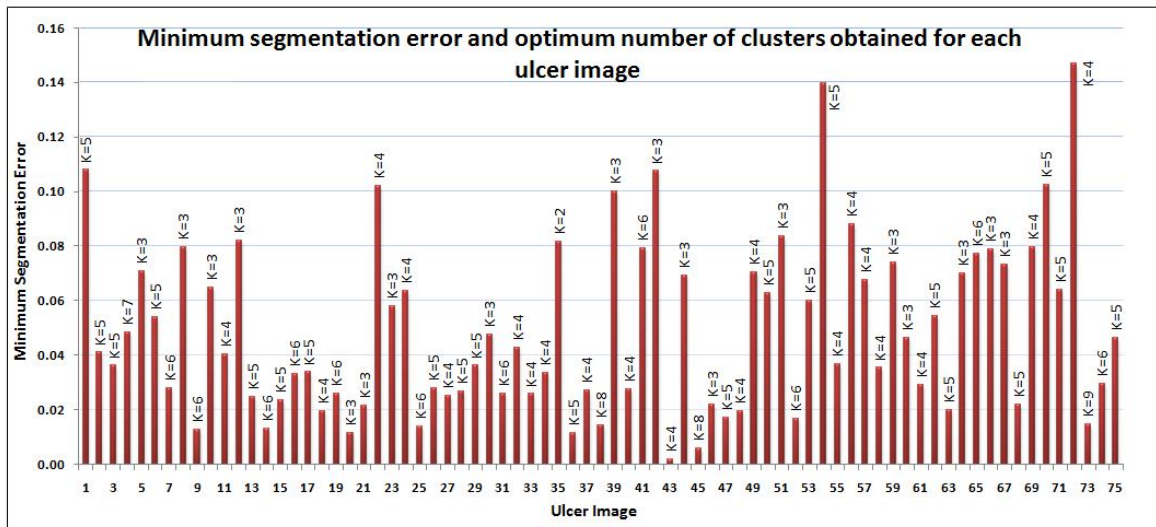


Figure 5.27: Minimum segmentation difference error and optimum number of clusters obtained for each ulcer image

Figure 5.28 shows the frequency at which the optimum number of clusters occurred among all the cluster numbers from $k = 2$ till $k = 10$ for all of the ulcer images. It can be noted from the figure that the optimum number of clusters at which

the granulation tissue was successfully segmented with the minimum difference error was between $k = 3$ and $k = 5$ with most cases occurring at $k = 4$ and $k = 5$. This can be explained by the fact that the surface of most ulcers contains a mixture of granulation, slough and necrotic tissues along with some damaged tissues or foreign materials that may exist on the surface. Hence, in order to segment and separate the granulation tissue from other tissues and regions on the surface and the surrounding skin, a cluster number of $k = 4$ or $k = 5$ is most appropriate. A few ulcers may have more foreign materials or damaged tissues within the ulcer surface and may subsequently need bigger cluster numbers, such as $k = 6$ to segment the granulation tissue from the rest of the haemoglobin image as indicated in Figure 5.28.

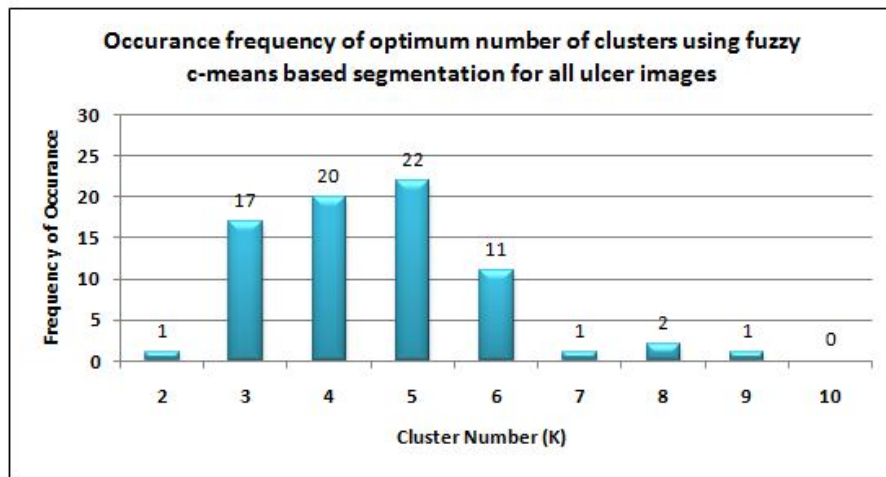


Figure 5.28: Frequency of optimum cluster number

Eventually, the granulation tissue detection system that was developed utilising both data transformation algorithms and clustering based segmentation algorithms was applied on all seventy-five ulcer images included in this study. The clustering based segmentation of the identified granulation regions is employed on each extracted haemoglobin image using fuzzy c-means clustering-based segmentation with the optimum number of clusters determined for that particular image as explained above. The surface area of the detected granulation tissues was then measured using Equation (4.5) illustrated in Chapter 4. The original colour images, the extracted haemoglobin images, and the detected granulation images in each of the seventy-five ulcer images are included in Appendix B.

5.3.2 Correlation and Overlap Analysis

The developed granulation detection system has been applied on the seventy-five ulcer images to identify and segment the regions of the granulation tissue on the ulcers' surfaces. The amount of the detected granulation tissue was then measured from the overall ulcer region and compared with the amount of granulation tissue traced by the dermatologists in the granulation assessment reference images illustrated in Chapter 4 (section 4.6.1). Figure 5.29 represents a scatter plot of the amount of the detected granulation tissue using the developed granulation detection system versus the amount of granulation tissue traced by the dermatologists. Generally, it is noted from the figure that there is a strong similarity between the amount of granulation tissue detected by the developed system and the one traced by the dermatologists.

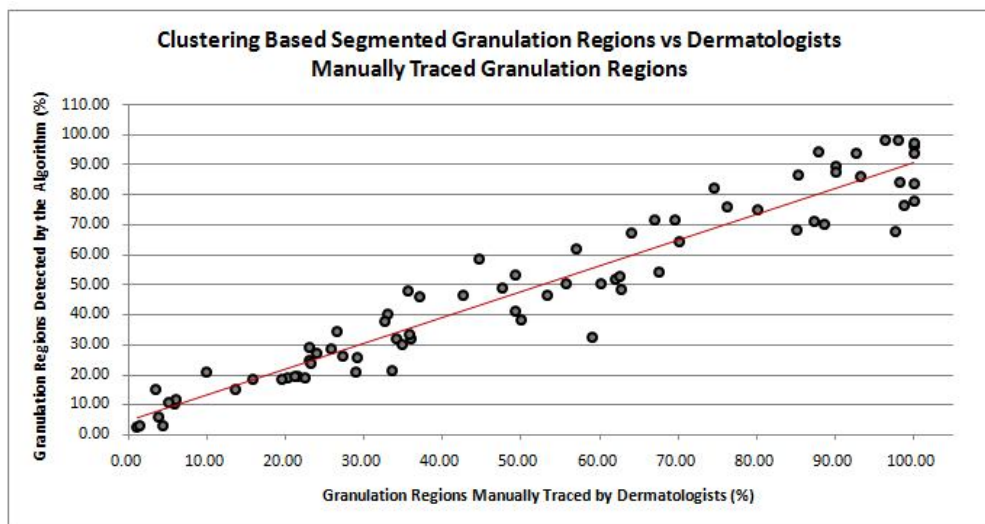


Figure 5.29: Scatter plot of detected granulation tissue using the developed granulation detection system versus the amount of granulation tissue traced by the dermatologists

In order to measure the relationship between the system's detection and dermatologists' tracings of the granulation tissue, the Pearson correlation coefficient was used. The Pearson correlation coefficient, which is denoted as r , was used to calculate the linear dependency between two measures or variables. It is defined as the covariance of the variables divided by the product of their standard deviation. Given two samples X and Y , the Pearson correlation coefficient is calculated as follows:

$$r = \frac{\sum_{i=1}^n (X_i - \bar{X})(Y_i - \bar{Y})}{\sqrt{\sum_{i=1}^n (X_i - \bar{X})^2} \sqrt{\sum_{i=1}^n (Y_i - \bar{Y})^2}} \quad (5.10)$$

where n is the number of data points in the sample and \bar{X} and \bar{Y} are the sample means. The value of the correlation coefficient ranges from 0 to (+)1 or (-)1 with values near (+)1 and (-)1 indicating strong correlation. In this study, the Pearson correlation coefficient was calculated using Equation (5.10). The correlation value obtained was 0.961 indicating a strong positive relationship and similarity between the amount of the granulation tissue detected by the system and the amount traced by the dermatologists.

The high correlation value obtained indicated a strong relationship and similarity between the system detection and the dermatologists' tracing (dermatologists' assessments) of the granulation tissue. However, it was important to inspect the actual amount of overlap (regions shared) between the granulation tissue detected by the system and the amount traced by the dermatologists for further analysis. The overlap between both amounts of granulation tissue was calculated as follows:

$$overlap = \left(\frac{2 * TP}{TP + TP + FN + FP} \right) * 100 \quad (5.11)$$

where (TP) are granulation pixels in the dermatologists' assessment that are correctly detected by the system as granulation, (FP) were non-granulation pixels that are incorrectly detected as granulation, (TN) were non-granulation pixels that were correctly detected as non-granulation, and (FN) are granulation pixels that are incorrectly detected as non-granulation.

The amount of overlap between the system's detection and dermatologists' assessments of the granulation tissue was calculated using Equation (5.11) for all seventy-five ulcer images. The results obtained can be divided into three main cases:

Case One: Here, both amounts of the detected granulation tissue and the assessed granulation tissue are quite similar with a high percentage of overlap between the two regions. Figure 5.30 shows a schematic diagram of this case. From the figure it is

evident that both regions occupy almost the same location with similar amounts on the ulcer's surface which results in a high overlap between both regions.

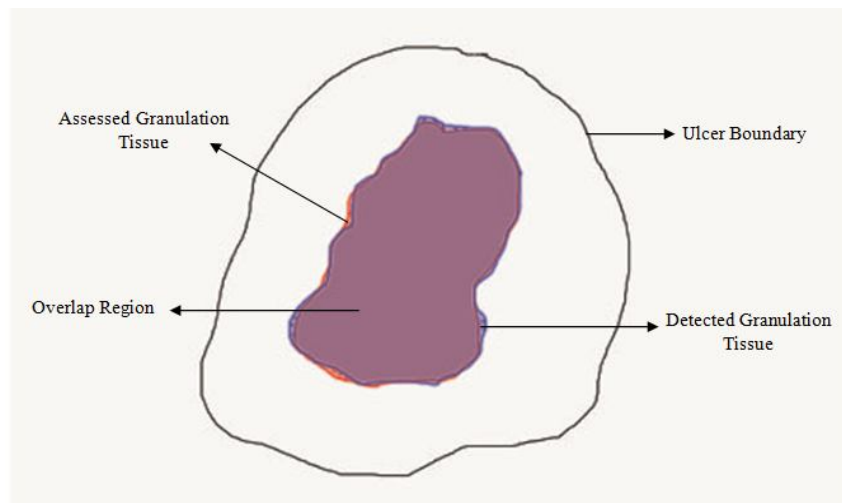


Figure 5.30: Schematic diagram of the overlap between detected and assessed granulation tissue regions (case one)

Such cases occurred mostly in ulcers where the granulation tissue covered most of the ulcer as one whole region or as a few regions with defined boundaries. In this case, the dermatologists found it quite easy to trace the granulation regions and draw lines around their boundaries to separate them manually from the rest of the ulcer when creating the granulation tissue reference images. Subsequently, the amount of detected granulation regions would be similar to the assessed ones within similar locations on ulcer surface which results in a high percentage of overlap.

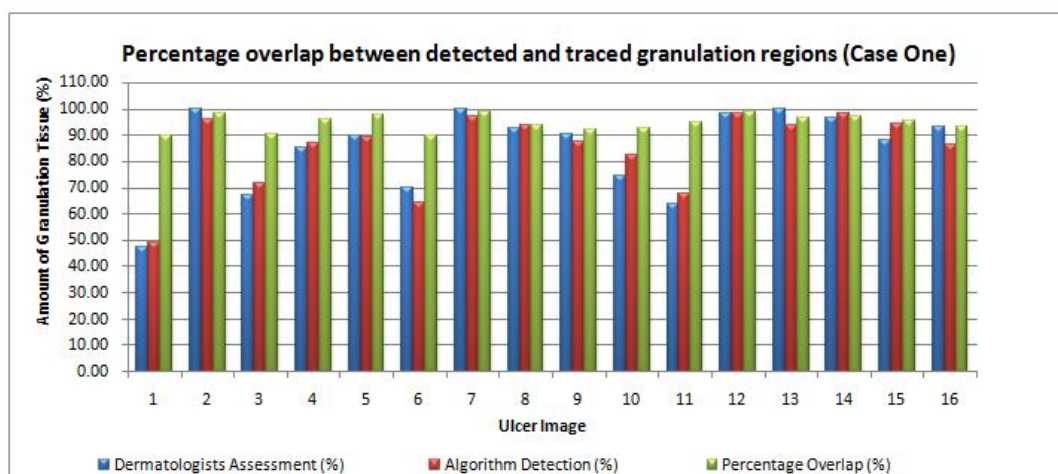


Figure 5.31: Percentage overlaps between detected and traced granulation tissue

In this study, this case has occurred in sixteen ulcer images as shown in Figure 5.31. Table 5.3 lists the amount of granulation tissue traced by dermatologists, the amount of granulation tissue detected by the system, the percentage difference and percentage overlap for each of the sixteen ulcer images. The difference range between the two regions in these cases was found to be within 0.04-7.53% while the amount of the overlap between both regions was found to be within 89.94% - 98.80% percentage of overlap. The average percentage difference was estimated as 3.6% while the average percentage overlap was 94.7% which indicates that both amounts of detected and assessed granulation regions were similar with a high percentage of overlap.

Table 5.3 Percentage overlaps between detected and traced granulation tissue

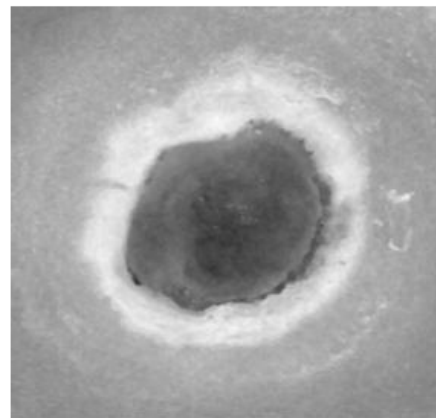
Ulcer No.	Dermatologists Tracings (%)	System Detection (%)	Difference (%)	Percentage Overlap (%)
1	47.56	48.94	1.38	89.94
2	100.00	96.09	3.91	98.01
3	66.98	71.76	4.78	90.28
4	85.20	86.82	1.62	95.77
5	90.03	89.47	0.56	97.65
6	70.21	64.35	5.86	89.84
7	100.00	97.12	2.88	98.54
8	92.61	93.71	1.10	93.71
9	90.16	87.40	2.77	91.94
10	74.62	82.15	7.53	92.86
11	63.95	67.46	3.51	95.11
12	97.96	98.00	0.04	98.80
13	100.00	93.77	6.23	96.78
14	96.40	98.07	1.67	97.31
15	87.81	94.13	6.32	95.55
16	93.15	86.12	7.02	93.37
Average			3.6%	94.7%

Figure 5.32 shows an example of this case (case number 13 in Figure 5.31). Figure 5.32 (a) shows the original ulcer image in which the granulation tissue appeared to cover the whole ulcer surface with well defined boundary that could be easily traced. Figure 5.32 (b) shows the extracted haemoglobin image with the granulation tissue region identified with a distinctive intensity range (darkest region). Figure 5.32 (c) shows the traced region of the granulation tissue while Figure 5.32 (d) shows the detected region of granulation tissue. Both regions occupied the same location with similar amounts which led to a high percentage of overlap. The

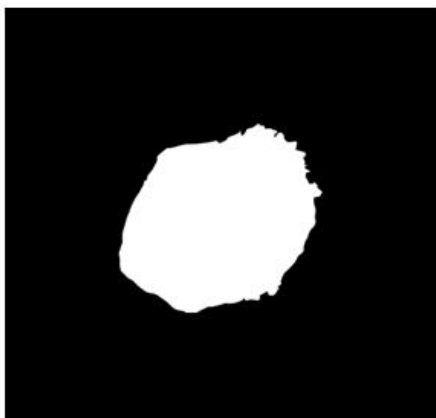
calculated percentage of overlap in this case was 96.78% with a difference of 6.2% between both regions.



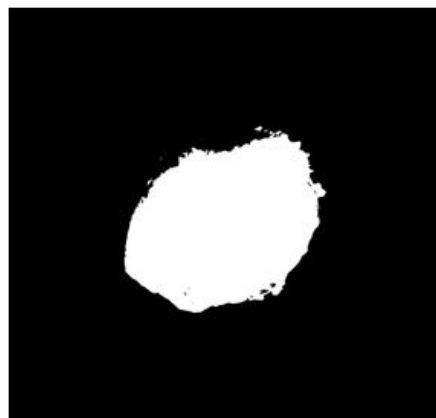
(a) Original colour ulcer image



(b) Extracted haemoglobin image



(c) Granulation tissue reference image



(d) Detected granulation region image

Figure 5.32: Example of granulation tissue detection (case one)

Case Two: Here, both the amount of the detected granulation tissue and the amount of the assessed granulation tissue are quite similar but with a low percentage of overlap between the two regions. Figure 5.33 shows a schematic diagram of this case. From the figure it is evident that both regions have quite similar amounts on the ulcer's surface. However, both regions occupy slightly different locations within the ulcer which results in a low percentage of overlap between both regions.

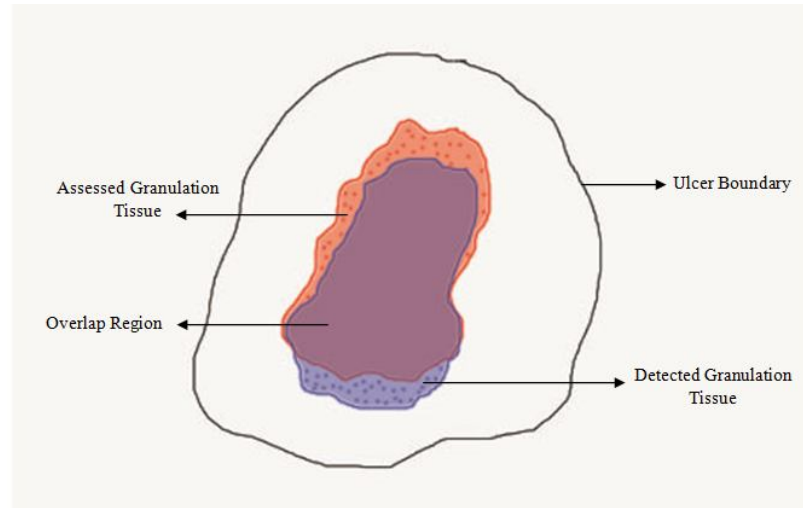


Figure 5.33: Schematic diagram of the overlap between detected and assessed granulation tissue regions (case two)

Such cases occurred mostly in ulcers where the granulation tissue was scattered all over the ulcer region mixed with other tissues especially with slough tissue. The dermatologists found it quite difficult to discern the regions of the granulation tissue and draw lines along their boundaries to separate them manually from the rest of the ulcer when creating the granulation tissue reference images. This led to either over segmentation or under segmentation of the granulation tissue in the reference images particularly in regions where the granulation tissue was heavily mixed with slough and could not be discerned visually. Subsequently, this led to regions of granulation tissue that exist in the reference images not being detected by the system (over segmentation of granulation tissue in reference image) or vice versa. In either case, the amount of the detected granulation regions could be similar to the assessed ones but would occupy quite different locations on the ulcer's surface which results in a low percentage overlap.

In this study, this case has occurred in twenty-two images as shown in Figure 5.34. Table 5.4 lists the amount of granulation tissue traced by dermatologists, the amount of granulation tissue detected by the system, the percentage difference and percentage overlap for each of the twenty-two ulcer images. The difference range between the two regions in was found to be within 0.1 -5.0% while the amount of the overlap between both regions is found to be within 58.05% - 88.62% percentage of overlap. The average percentage difference was estimated as 2.5% while the average

percentage overlap was 73.5% which indicates that both amounts of the detected and assessed granulation regions were similar but with a low percentage of overlap.

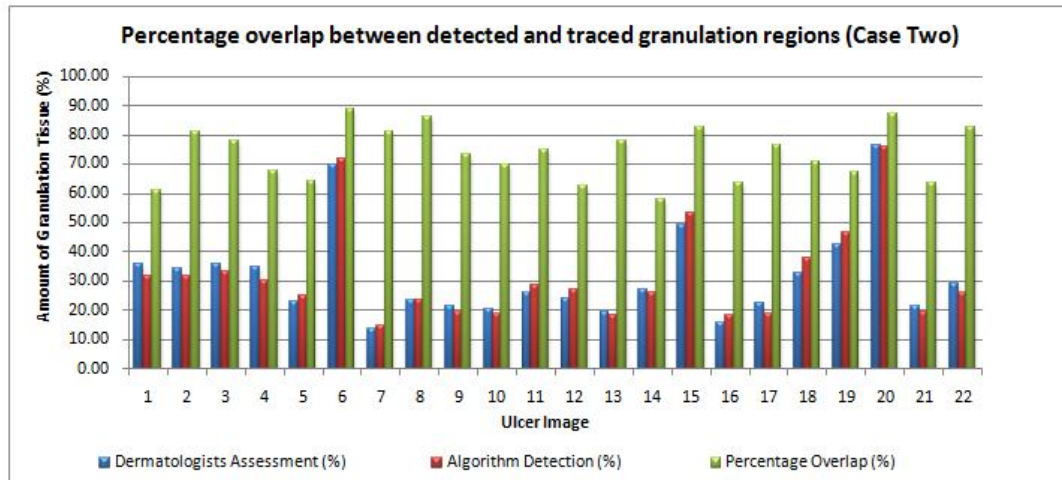


Figure 5.34: Percentage overlaps between detected and traced granulation tissue

Table 5.4 Percentage overlaps between detected and traced granulation tissue

Ulcer No.	Dermatologists Assessment (%)	Algorithm Detection (%)	Difference (%)	Percentage Overlap (%)
1	35.98	31.72	4.3	60.79
2	34.11	31.79	2.3	80.78
3	35.69	33.40	2.3	77.68
4	34.89	29.93	5.0	67.80
5	23.09	24.87	1.8	64.30
6	69.50	71.61	2.1	88.62
7	13.61	14.87	1.3	81.06
8	23.25	23.68	0.4	85.91
9	21.49	19.21	2.3	73.19
10	20.29	18.83	1.5	69.80
11	25.83	28.53	2.7	74.85
12	23.97	27.06	3.1	62.70
13	19.50	18.52	1.0	78.10
14	27.19	26.26	0.9	58.05
15	49.16	53.38	4.2	82.42
16	15.86	18.34	2.5	63.60
17	22.44	18.74	3.7	76.59
18	32.61	37.62	5.0	70.94
19	42.62	46.48	3.9	66.94
20	76.18	76.13	0.1	87.04
21	21.20	19.41	1.8	63.36
22	29.02	25.78	3.2	82.51
Average			2.5%	73.5%

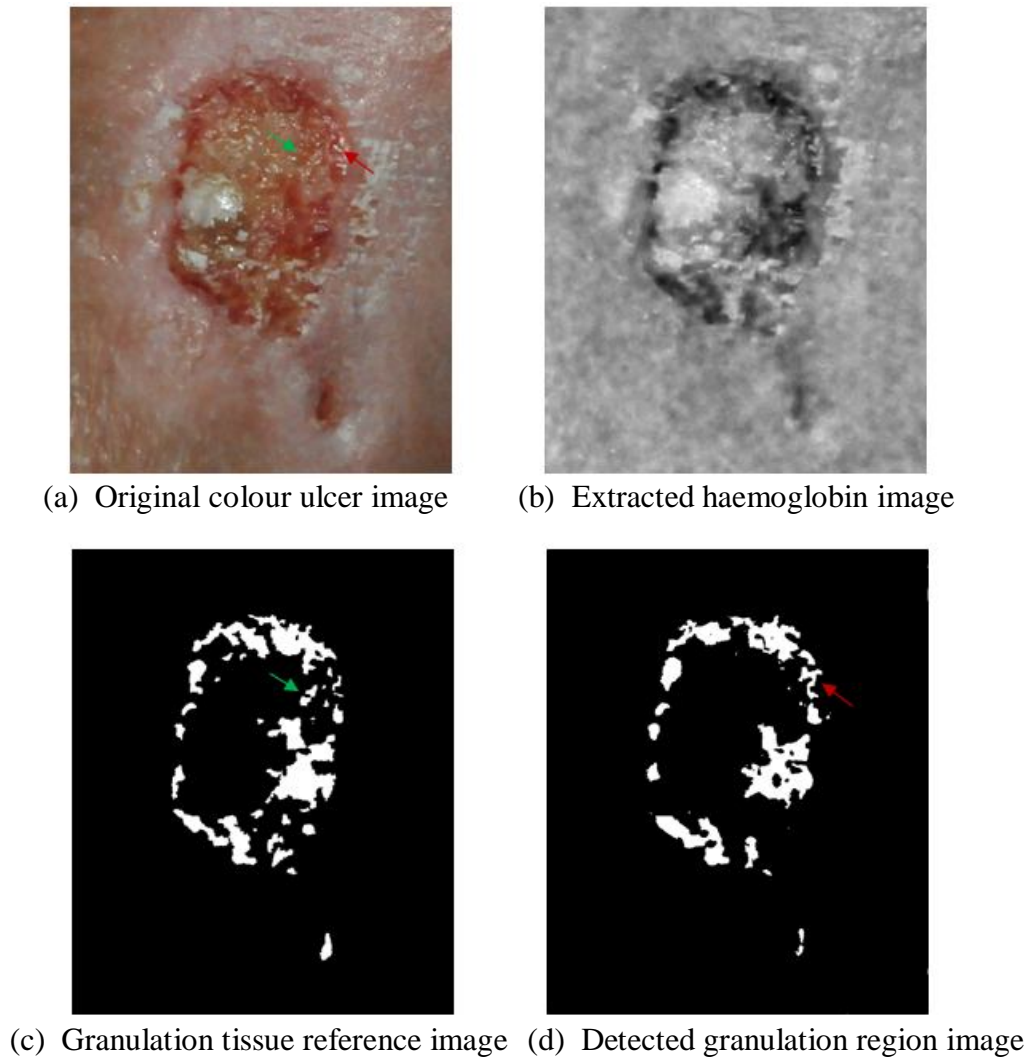


Figure 5.35: Example of granulation tissue detection (case two)

Figure 5.35 shows an example of this case (case number 9 in Figure 5.34). Figure 5.35 (a) shows the original ulcer image in which the granulation tissue appeared to be scattered all over the ulcer surface mixed with slough and other foreign materials which made it difficult to be traced visually. Figure 5.35 (b) shows the extracted haemoglobin image with the granulation tissue region identified with a distinctive intensity range (darkest region). Figure 5.35 (c) shows the traced region of the granulation tissue while Figure 5.35 (d) shows the detected region of the granulation tissue using the developed system. The green arrow in Figure 5.35 (c) indicates an example of a region that contained slough mistakenly identified as part of granulation region by the dermatologists. This region however was correctly identified as non-granulation by the system and did not appear in the system detection image as shown

in Figure 5.35 (d). The red arrow on the other hand indicates an example of the granulation tissue regions detected by the system in Figure 5.35 (d) but not traced by the dermatologists in Figure 5.35 (c). Subsequently, this would lead to both regions having similar amounts but occupying different locations in some parts on the ulcer's surface which would lead to a low percentage overlap between both regions. The calculated percentage of overlap in this case was 73.19% with a difference of 2.3% between both regions.

Case Three: Here, both the amount of the detected granulation tissue and the amount of the assessed granulation tissue are not the same with a low percentage of overlap between the two regions. There are two categories in this case:

Case Three-One: The amount of the detected granulation tissue is more than the amount of the assessed granulation tissue. Figure 5.36 shows a schematic diagram of this case. From the figure it is evident that the detected region of the granulation tissue is more than the amount of the assessed granulation tissue. Subsequently, the overlap between both regions is low.

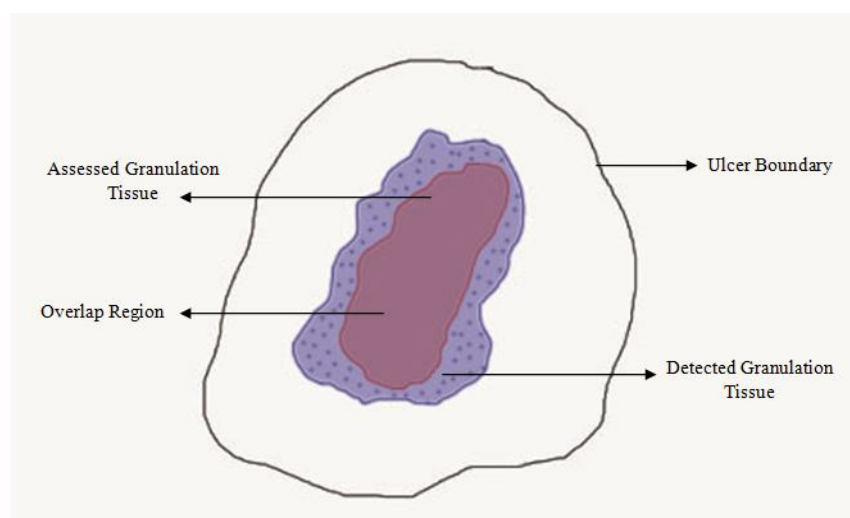


Figure 5.36: Schematic diagram of the overlap between detected and assessed granulation tissue regions (case three-1)

Such cases occurred mostly in ulcers where the granulation tissue was scattered all over the ulcer region mixed with other tissues particularly with slough tissue. The dermatologists found it difficult to discern these regions visually. If slough was the dominant tissue type in the ulcer and was slightly mixed with granulation tissue, the

dermatologists mistakenly marked the whole region as slough although there may have been some granulation tissue within the same region. The algorithm could detect those regions of granulation tissue and clearly separate them from the slough resulting in a larger number of detected granulation tissue regions compared to the assessed ones which subsequently led to a low percentage of overlap.

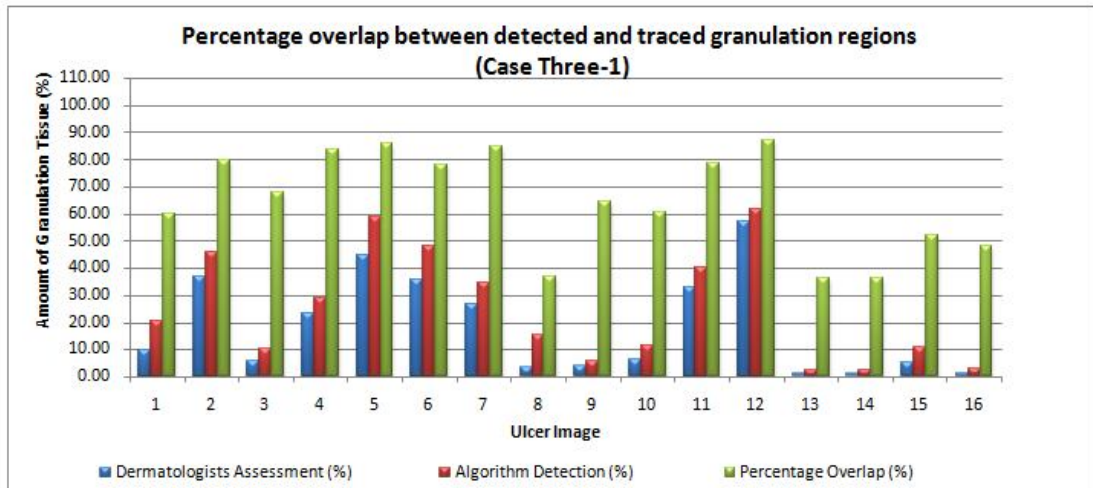


Figure 5.37: Percentage overlaps between detected and traced granulation tissue

In this study, this case has occurred in sixteen images as shown in Figure 5.37.

Table 5.5 lists the amount of granulation tissue traced by dermatologists, the amount of granulation tissue detected by the system, the percentage difference and percentage overlap for each of the sixteen ulcer images. The difference range between the two regions in this case was found to be within 1.43 -14.03% while the amount of the overlap between both regions was found to be within 36.29% - 86.87% percentage of overlap. The average percentage difference was estimated as 6.6% while the average percentage overlap was 65.0% which indicates that the amounts of the detected and assessed granulation regions are not similar with a low percentage of overlap.

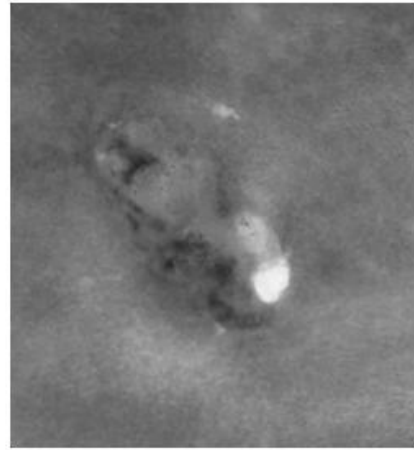
Table 5.5 Percentage overlaps between detected and traced granulation tissue

Ulcer No.	Dermatologists Assessment (%)	Algorithm Detection (%)	Difference (%)	Percentage Overlap (%)
1	9.96	20.64	10.68	59.81
2	37.07	45.78	8.71	79.83
3	5.82	10.20	4.37	67.82
4	23.02	28.88	5.86	83.45
5	44.63	58.66	14.03	85.84
6	35.59	48.05	12.46	78.23
7	26.48	34.37	7.89	84.95
8	3.41	15.19	11.78	36.65
9	3.79	5.66	1.88	64.54
10	6.03	11.65	5.62	60.34
11	33.04	39.94	6.90	78.48
12	57.04	61.90	4.86	86.87
13	1.04	2.47	1.43	36.29
14	1.04	2.47	1.43	36.29
15	5.15	10.65	5.50	52.33
16	1.30	2.93	1.63	48.20
Average			6.6%	65.0%

Figure 5.38 shows an example of this case (case number 15 in Figure 5.37). Figure 5.38 (a) shows the original ulcer image in which the granulation tissue appeared to be scattered all over the ulcer surface mixed with slough and necrotic tissues which made it difficult to trace visually. Figure 5.38 (b) shows the extracted haemoglobin image with the granulation tissue region identified with a distinctive intensity range (darkest region). Figure 5.38 (c) shows the traced region of the granulation tissue while Figure 5.38 (d) shows the detected region of the granulation tissue. It was noted that the amount of the detected granulation tissue was more than the amount of assessed the granulation tissue due to some regions of the mixed granulation and slough perceived as slough by the dermatologists as explained earlier. The system however detected the regions of the granulation tissue and clearly separated those (indicated by the red arrows in Figure 5.38 (d)) from the regions of slough which resulted in larger amounts of detected granulation tissue compared to the assessed ones and subsequently lower percentage of overlap. The calculated percentage overlap in this case was 52.33% with a difference of 5.50% between both regions.



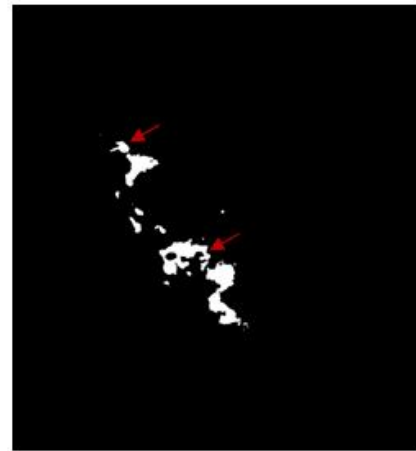
(a) Original colour ulcer image



(b) Extracted haemoglobin image



(c) Granulation tissue reference image



(d) Detected granulation region image

Figure 5.38: Example of granulation tissue detection (case three-1)

Case Three-Two: The amount of the detected granulation tissue is less than the amount of the assessed granulation tissue. Figure 5.39 shows a schematic diagram of this case. From the figure it is evident that the amount of the detected granulation tissue is less than the amount of the assessed granulation tissue. Subsequently, the overlap between both regions is low.

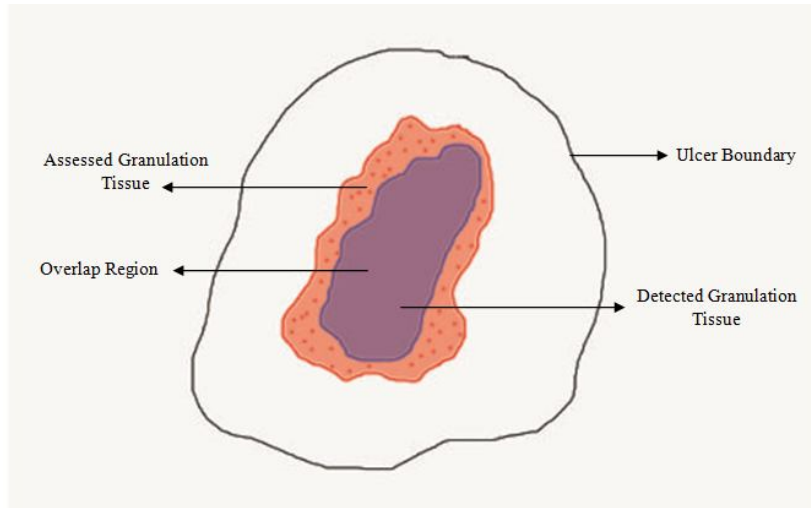


Figure 5.39: Schematic diagram of the overlap between detected and assessed granulation tissue regions (case three-2)

Such cases occurred mostly in ulcers where the granulation tissue was scattered all over the ulcer region mixed with other tissues particularly slough tissue. The dermatologists found it difficult to discern these regions visually. If granulation tissue was the dominant tissue type in the ulcer and was slightly mixed with slough or other tissues, the dermatologists mistakenly marked the whole region as granulation tissue although there may have been some slough within the same region. The algorithm could detect those regions of granulation tissue and clearly separate them from the slough resulting in a fewer detected granulation tissue regions compared to the assessed ones which subsequently led to a low percentage of overlap.

In this study, this case has occurred in twenty-one images as shown in Figure 5.40. Table 5.6 lists the amount of granulation tissue traced by dermatologists, the amount of granulation tissue detected by the system, the percentage difference and percentage overlap for each of the twenty-one ulcer images. The difference range between the two regions in this case was found to be within 1.59 -30.03% while the amount of the overlap between both regions was found to be within 55.19% - 91.37% percentage of overlap. The average percentage difference was estimated as 13.4% while the average percentage overlap was 81.4% which indicates that the amounts of the detected and assessed granulation regions were not similar with a low percentage of overlap.

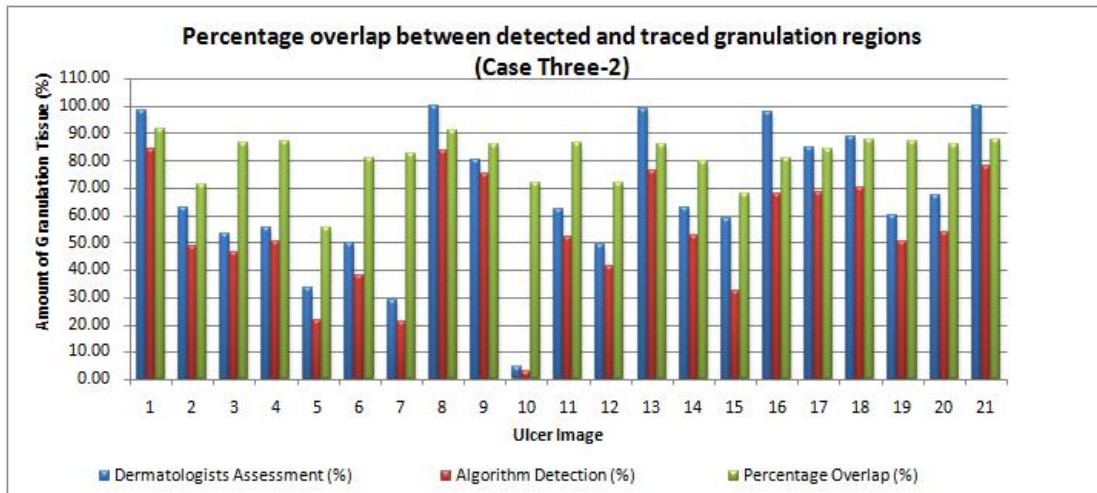


Figure 5.40: Percentage overlaps between detected and traced granulation tissue

Table 5.6 Percentage overlaps between detected and traced granulation tissue

Ulcer No.	Dermatologists Assessment (%)	Algorithm Detection (%)	Difference (%)	Percentage Overlap (%)
1	98.24	84.39	13.85	91.37
2	62.77	48.64	14.12	71.31
3	53.30	46.67	6.63	86.50
4	55.64	50.29	5.35	87.23
5	33.46	21.54	11.93	55.19
6	49.96	38.07	11.89	80.72
7	28.90	21.01	7.89	82.34
8	100.00	83.65	16.35	91.10
9	80.08	75.02	5.05	85.86
10	4.38	2.79	1.59	72.04
11	61.99	51.99	10.00	86.67
12	49.23	41.30	7.93	71.92
13	98.76	76.33	22.44	86.16
14	62.51	52.66	9.86	79.84
15	58.98	32.24	26.74	67.95
16	97.71	67.67	30.03	80.72
17	85.02	68.31	16.71	84.43
18	88.53	69.94	18.59	87.45
19	60.16	50.38	9.78	87.15
20	67.46	53.97	13.49	86.03
21	100.00	78.04	21.96	87.66
Average			13.4%	81.4%

Figure 5.41 shows an example of this case (case number 5 in Figure 5.40). Figure 5.41 (a) shows the original ulcer image in which the granulation tissue appeared to be scattered all over the ulcer surface mixed with slough tissue which made it difficult to trace visually. Figure 5.41 (b) shows the extracted haemoglobin image with the granulation tissue region identified with a distinctive intensity range (darkest regions). Figure 5.41 (c) shows the traced region of the granulation tissue while Figure 5.41 (d) shows the detected region of the granulation tissue. It was noted that the amount of the assessed granulation tissue was more than the amount of the detected granulation tissue due to some regions of mixed granulation and slough perceived as granulation by the dermatologists as explained earlier. The system detected the regions of the granulation tissue and separated them from the slough (indicated by the green arrows in Figure 5.41 (c)) which resulted in a lesser amount of detected granulation tissue compared to the assessed ones and subsequently a lower percentage of overlap. The calculated percentage of overlap in this case was 55.19% with a difference of 11.93% between both regions.

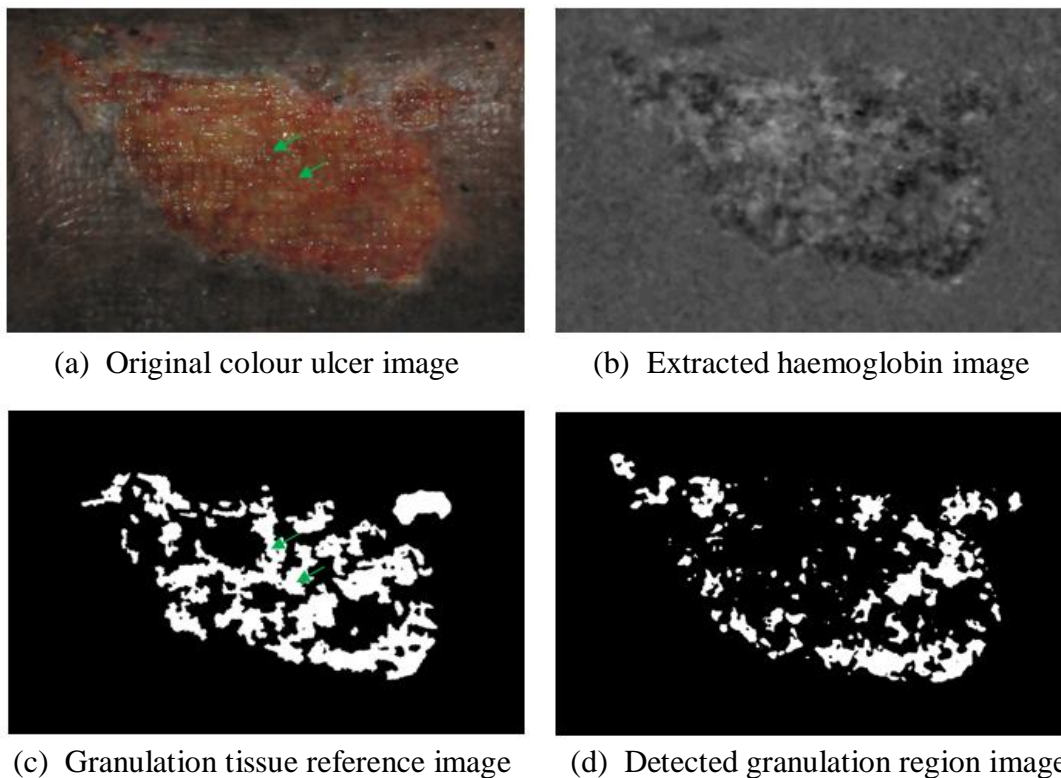


Figure 5.41: Example of granulation tissue detection (case three-2)

From the correlation and overlap analysis discussed above, it can be generally concluded that the developed granulation detection system is able to identify regions of granulation tissue that could be difficult to discern visually on real ulcer surfaces using colour images of chronic ulcers. The identified regions of the granulation tissue can be clearly contrasted and segmented from other non-granulation regions on the ulcer's surface. The amount of the detected granulation tissue, in terms of surface area, can also be measured using the developed system during consecutive visits throughout the course of treatment and used to monitor the healing progression as explained in Chapter 4 (section 4.7.2). If the current treatment is effective, the amount of the detected granulation tissue should increase throughout the course of the treatment. The original colour images, the extracted haemoglobin images, and the detected granulation images in each of the seventy-five ulcer images are included in Appendix B.

5.4 Summary

The main objective of this research work is to identify regions of healthy granulation tissue on ulcer surfaces utilising the developed granulation tissue detection system. The identified granulation tissue regions can be segmented from the rest of the ulcer image and their surface area can be measured to provide an objective measure of ulcer healing progression.

Ulcer tissue reference images that contain patches of skin, slough, necrotic and granulation tissues were developed to investigate the performance of the developed granulation detection algorithms. These images were designed to test the algorithms' ability to detect and distinguish granulation tissue regions of different sizes in pixel units from the rest of the tissues types. Furthermore, noise images were created based on white Gaussian noise model and added to the ulcer tissue reference images to investigate the algorithms' performance in images corrupted by noise as is the case with most real images. In this study, twenty four ulcer tissue reference images were created with SNR values ranging from 36dB -1dB according to varying noise levels added to the images.

The developed algorithms were applied on the ulcer tissues reference images. The extracted haemoglobin images identified granulation tissue patches with intensity value range that could be contrasted from the rest of the tissues. Otsu's thresholding was applied on the extracted haemoglobin images to segment granulation tissue patches from the rest of the image. It was found that the developed system was able to identify and detect the regions of the granulation tissue, from the smallest region size of 1x1 pixels and above, in ulcer images corrupted with white Gaussian noise corresponding to SNR levels of more than 12dB with performance values of more than 96.0% sensitivity, 99.6% specificity and 99.5% accuracy. It was also found that with more noise added to the images, more false pixels (false negatives and false positives) were detected and subsequently the performance of the system decreased gradually. For images with SNR levels of 12dB and below, some granulation regions, especially of sizes 1x1, 2x2 and 3x3 pixel, might not be detected due to the increased number of detected false pixels.

The developed granulation detection system was applied on seventy-five ulcer images to detect the regions of the granulation tissue on the ulcers' surfaces. The system extracted the haemoglobin images from the colour images of ulcers that highlight the regions of the granulation tissue with a range of intensity values that could be contrasted from the rest of the image. Clustering-based segmentation was then applied on the extracted haemoglobin images to segment the granulation tissue regions from the rest of the image. The optimum number of clusters k at which the granulation tissue was successfully segmented with the minimum segmentation difference error occurred mostly at $k = 4$ and $k = 5$.

The amount of the detected granulation tissue was measured and compared with the amount of the granulation tissue traced by the dermatologists at Hospital Kuala Lumpur. It was found that there was a strong positive relationship and similarity between the amount of the granulation tissue detected by the system and the amount traced by the dermatologists as indicated by the obtained high Pearson correlation coefficient value of 0.961.

For further analysis, the actual amount of the overlap between the granulation tissue detected by the system and the amount traced by the dermatologist was inspected. There are three sets of cases that can be observed. In the first set of cases (occurred in sixteen ulcer images), both the amount of the detected granulation tissue and the amount of the traced granulation tissue are quite similar with a high percentage of overlap between them. In the second set of cases (occurred in twenty-two ulcer images), both the amount of the detected granulation tissue and the amount of the traced granulation tissue are quite similar but with a low percentage of overlap between them. In the third set of cases the amount of the detected granulation tissue and the amount of the assessed granulation tissue are not the same with a low percentage of overlap between the two regions. This set of cases has been further categorized into cases in which the amount of detected granulation tissue is more than the traced one (occurred in sixteen ulcer images) and cases in which the amount of the detected granulation is less than the traced one (occurred in twenty-one ulcer images).

Granulation tissue appeared mixed with slough and other tissues in most of ulcer cases which made it difficult for the dermatologists to identify those regions based on visual inspection. The difference between the amount of the granulation tissue detected by the developed system and the amount traced by the dermatologists is due to the system's ability to identify and clearly separate the regions of the granulation tissue that could be difficult to discern visually from the rest of the non-granulation regions on the ulcers' surfaces. This is very significant in detecting early stages of ulcer healing that is indicated by the growth of the granulation tissue on ulcers' surfaces that could not be detected using simple visual inspection. The amount of detected granulation tissue, in terms of surface area, can be measured using the developed system during consecutive visits throughout the course of the treatment and used to monitor the ulcer healing progression.

CHAPTER 6

CONCLUSION

6.1 Introduction

Chronic skin ulcers occur when the injured tissues do not follow the normal healing process within a specific period of time due to underlying aetiologies or improper wound management. They cause severe pain to the patients and put them at the risk of limb amputation. Detecting early stages of ulcer healing is important to improve clinical decisions and enhance the effectiveness of the treatment. In this study, statistical and digital image processing techniques are employed to develop an image analysis system that detects regions of granulation tissue as an objective assessment measure of early healing stages in chronic ulcers.

6.2 An Overall Summary

The appearance of the ulcer's surface changes throughout the healing process [10]. Depending on the severity status, ulcers can initially appear covered with layers of unhealthy black necrosis and yellow slough. As ulcers heal, healthy red granulation tissue starts to grow from the ulcer base gradually replacing the unhealthy tissue and filling the ulcer cavity. Identifying regions of granulation tissue growing on the ulcer's surface is an important measure of ulcer healing progression which reflects on the efficacy of ulcer management and treatment.

Most of the assessment methods implemented currently in clinical practice depends on a visual inspection of the ulcer's appearance and tissue types on the ulcer's surface. Human vision inspection is subjective and lacks precision and

consistency and hence is not suitable to perform tissue analysis. Monitoring of ulcers requires an objective, precise quantitative and reproducible assessment. Digital image analysis has been employed to detect and classify ulcer tissues to provide an accurate objective assessment of ulcer healing. A detailed discussion on ulcer tissue assessment using digital imaging was given in Chapter 2. Most of the work developed in the field of wound assessment via digital imaging utilized colour features and attributes as the main components for analysis. However, colour analysis is always compromised by the unavoidable differences in acquisition conditions which affect the colour quality and leads to inaccurate results.

Most of the incident light penetrates into the ulcer and skin tissues following a complex path where it interacts with different interior structures and pigments and gets remitted back from the skin [22]. These interactions change the spectral composition of the light which reflects the optical properties of the ulcer tissues structures and pigments. The remitted light can be captured by digital cameras to produce colour digital images of chronic ulcers [56], [57]. Hence, an understanding of the colour image formation reveals diagnostically important facts about the internal structure and composition of the skin ulcers [23].

Ulcer healing is indicated by the growth of granulation tissue which appears red in colour due to the pigment haemoglobin content in the newly built blood capillaries [24]. Anderson *et al.* studied the absorption spectra of haemoglobin and other skin pigments and found that haemoglobin exhibits total reflection of light at 600nm and above [22]. This range of wavelengths corresponds to the red colour component of the visible spectrum which explains why the granulation tissue that contains haemoglobin pigment appears red in colour when viewed under visible light [24]. Studies show that the optical characteristics of haemoglobin can be detected in colour images and used to show their content within human skin [25], [26].

Therefore, this study aimed to develop an image analysis system that identifies and detects regions of granulation tissue on ulcer surface based on the content of the pigment haemoglobin and its distribution on ulcers' surfaces. Since the growth of granulation tissue indicates ulcer healing, identifying and quantifying the amount of

detected granulation tissue gives an indication of the healing progression which reflects on the efficacy of the ulcer management and treatment.

The approach utilized in developing the granulation tissue detection system is to apply data transformation utilising the independent component analysis (ICA) to extract source grey-level images that show the distribution of the pigment haemoglobin. Independent component analysis is a multivariate data analysis technique used to recover source signals from their observed linear combinations. ICA assumes that the observed signals, in this case the Red, Green and Blue data vectors of each ulcer image, are generated by linearly mixing original source signals with an unknown mixing matrix [66], [67]. ICA estimates the source images assuming that they are statistically independent which is achieved when their probability density function can be written as the product of their marginal independent distributions [67]. In this study, the fastICA technique was implemented on each of the acquired seventy-five ulcer images to estimate their source images as projections that maximize non-Gaussianity which is used to measure independence [66], [69-71]. In this method, an approximation of negentropy, which is Newton's iterative approximation, was used to measure non-Gaussianity and estimate the independent source images. Among the estimated source images for each observed colour ulcer image is the haemoglobin image that showed the regions of haemoglobin distribution reflecting regions of granulation tissue on the ulcer's surface.

Ulcer tissues reference images that contained patches of skin, slough, necrotic and granulation tissues were developed to investigate the performance of the developed granulation detection algorithms. The developed system successfully extracted haemoglobin images that identified granulation tissue regions with an intensity value range that could be contrasted from the rest of the tissues. It was also found that the developed system was able to detect regions of granulation tissue, from the smallest region size of 1x1 pixels and above, in ulcer images corrupted with white Gaussian noise corresponding to SNR levels of more than 12dB with performance values of more than 96.0% sensitivity, 99.6% specificity and 99.5% accuracy. With more noise added to the images, more false pixels (false negatives and false positives) were detected and subsequently the performance of the system decreased gradually. For

images with SNR levels of 12dB and below, some granulation regions, especially of sizes 1x1, 2x2 and 3x3 pixel, might not be detected due to an increased number of detected false pixels.

The developed granulation detection system was applied on seventy-five ulcer images to detect regions of granulation tissue on their surfaces. The system extracted haemoglobin images that highlighted the regions of granulation tissue with a range of intensity values that could be contrasted from the rest of the image. Clustering-based segmentation was employed in this study to segment the identified regions of granulation tissue on the extracted haemoglobin images. Clustering is a common technique of unsupervised learning and classification where elements of a dataset are partitioned into several clusters so that points in one group are similar to each other and are as different as possible from points in other groups [74].

In this study, soft clustering was employed utilising fuzzy c-means algorithms applied to the haemoglobin images to classify the granulation regions based on their range of intensity values. In fuzzy c-means, each point in a dataset is assigned membership grades to each of the k number of clusters based on a similarity measure, usually the Euclidean distance, between the point and the cluster centre [75]. The classified granulation regions are then segmented from the rest of the images accordingly. The optimum number of clusters k , at which the granulation tissue is successfully segmented with a minimum segmentation difference error, occurred mostly at $k = 4$ and $k = 5$.

The amount of detected granulation tissue was measured and compared with the amount of granulation tissue traced by the dermatologists at Hospital Kuala Lumpur. It was found that there was a strong similarity between the amount of granulation tissue detected by the system and the amount traced by the dermatologists as indicated by the obtained high Pearson correlation coefficient value of 0.961. Furthermore, it was noted that the granulation tissue appeared mixed with slough and other tissues in most of the ulcer cases which made it difficult for dermatologists to identify those regions based on visual inspection. The developed system has the ability to identify and clearly separate regions of granulation tissue that could be difficult to discern

visually from the rest of the non-granulation regions on the ulcers' surfaces. The amount of the detected granulation tissue, in terms of surface area, could be measured using the developed system during consecutive visits throughout the course of the treatment and used to monitor the ulcer healing progression.

6.3 Contribution and Future Work

The main contribution of this work is the development of an imaging-based system that detects regions of granulation tissue growing on ulcer surfaces using colour images of chronic ulcers. Detecting the growth of granulation tissue on ulcers surfaces is an important measure of the ulcer healing progression.

The development of the granulation tissue detection system incorporates a unique approach which is based on investigating the optical characteristics of pigment haemoglobin and utilising its content to detect regions of granulation tissue. This approach is unique in a way that it does not focus on colour image features and attributes directly like previous work in this field, instead it draws an understanding of tissue histology utilising a physics-based interpretation of image colour.

The developed system is able to detect regions of granulation tissue, from the smallest size of 1x1 pixels and above, that are mixed with other tissues on the ulcer's surface and cannot be discerned visually. This is very significant in detecting early stages of ulcer healing especially in ulcers where granulation tissue is spreading slowly over the ulcer's surface and cannot be detected using simple visual inspection.

Clinicians inspect the ulcer visually and provide a subjective assessment based on the approximation of the amount of different tissues, particularly granulations tissue, to assess the healing progression. This leads to an inaccurate and inconsistent assessment which affects the performance and quality of the treatment and care. The system provides an objective, quantitative and reproducible assessment of the healing progression that can improve clinical decisions and enhance treatment efficacy.

In this study, ulcer boundary reference images have been developed based on a manual tracing of the ulcer boundary to illuminate any regions of the surrounding skin outside the ulcer wrongly detected as granulation tissue as explained in Chapter 4 (section 4.7.1). The developed granulation detection system can be further enhanced by incorporating algorithms that detect the ulcer boundary automatically and confine the granulation detection to the ulcer region.

Since clustering-based segmentation is employed in this study, determining the number of clusters is critical in ensuring the correct segmentation of granulation tissue. In this study, it has been found that the optimum number of clusters varies between $k=3$ and $k=5$ as shown in Chapter 5 (section 5.3.1). The system's segmentation can be further improved by investigating the properties of the intensity values of the identified granulation regions in the extracted haemoglobin images. Information obtained can then be integrated with the findings of this study to determine the number of clusters automatically.

It is hoped that this study will open the door for possible avenues of more research works that focus on investigating the optical characteristics of ulcer tissues based on their histology and cellular composition and utilising them to detect their content in colour images of chronic ulcers. Ultimately, the goal is to develop a new objective and non-invasive scheme to assess the healing progression of chronic ulcers in a more precise and reliable way.

REFERENCES

- [1] A. Shai and H. I. Maibach, Wound Healing and Ulcers of the Skin - Diagnosis and Therapy - The Practical Approach. Berlin Heidelberg New York: Springer, pp. 1-132, 2005.
- [2] M. I. Yusof, A. R. Sulaiman, and M. D. A. J, "Diabetic foot complications : a two-year review of limb amputation in a Kelantanese population," *Medical Journal Of Malaysia*, vol. 48, no. 8, pp. 729-732, 2007.
- [3] F. Werdin, M. Tennenhaus, H.-E. Schaller, and H.-O. Rennekampff, "Evidence-Based Management Strategies for Treatment of Chronic Wounds.," *Eplasty*, vol. 9, pp. 169-179, Jan. 2009.
- [4] K. Faridah and M. Azmi, "Retrospective Study of Predictors for Foot Ulceration among Diabetic Patients attending Kuala Langat Health Centre from 1999 to 2008," *Journal of Community Health*, vol. 15, no. 2, pp. 43-59, 2009.
- [5] D. J. Margolis, W. Bilker, J. Santanna, and M. Baumgarten, "Venous Leg Ulcer: Incidence and Prevalence in the Elderly," *Journal of the American Academy of Dermatology*, vol. 46, no. 3, pp. 381-6, Mar. 2002.
- [6] S. A. Amin et al., "Analysis Study on Healthcare Provider Cost for Diabetic Foot Treatment at Orthopaedic Ward, Universiti Kebangsaan Malaysia Medical Centre in Year 2006," *Community Health*, vol. 15, no. 1, pp. 32-38, 2009.
- [7] N. J. M. London and R. Donnelly, "ABC of arterial and venous disease: Ulcerated lower limb," *British Medical Journal*, vol. 320, no. 7249, pp. 1589-1591, Jun. 2000.
- [8] "The Care of Patients with Chronic Leg Ulcer - A National Clinical Guideline," no. 26. Scottish Intercollegiate Guidelines Network, pp. 1-19, 1998.
- [9] G. Gethin, "The Importance of Continuous Wound Measuring," *Wounds*, vol. 2, no. 2, pp. 60-8, 2006.

- [10] R. Goldman and R. Salcido, "More than One Way to Measure a Wound: An Overview of Tools and Techniques," *Advances in Skin and Wound Care*, vol. 15, no. 5, pp. 236-245, 2002.
- [11] M. Romanelli, G. Gaggio, M. Coluggia, F. Rizzello, and A. Piaggese, "Technological Advances in Wound Bed Measurements," *Wounds*, vol. 14, no. 2, pp. 58-66, 2002.
- [12] D. Gray, R. White, P. Cooper, and A. Kingsley, "Applied Wound Management Supplement: The Wound Healing Continuum - An Aid to Clinical Decision Making and Clinical Audit," *Wounds- UK*. Wounds- UK, pp. 9-12, 2004.
- [13] M. Herbin, A. Venot, J. Y. Devaux, and C. Piette, "Color Quantitation Through Image Processing in Dermatology," *IEEE transactions on medical imaging*, vol. 9, no. 3, pp. 262-9, Jan. 1990.
- [14] M. Herbin et al., "Assessment of Healing Kinetics Through True Color Image Processing," *IEEE transactions on medical imaging*, vol. 12, no. 1, pp. 39-43, Jan. 1993.
- [15] A. Hoppe, D. Wertheim, J. Melhuish, M. Horris, K. G. Harding, and R. J. Williams, "Computer Assisted Assessment of Wound Appearance using Digital Imaging," in *23rd Annual International Conference of the IEEE Engineering in Medicine and Biology Society*, pp. 25-8, 2001.
- [16] A. A. Perez, A. Gonzaga, and J. M. Alves, "Segmentation and Analysis of Leg Ulcers Color Images," in *International Workshop on Medical Imaging and Augmented Reality (MIAR'01)*, pp. 262-266, 2001.
- [17] W. P. Berris and S. J. Sangwine, "A Colour Histogram Clustering Technique for Tissue Analysis of Healing Skin Wounds," in *Proceedings of the 6th International Conference on Image Processing (IPA97)*, no. 443, pp. 693-697, 1997.
- [18] H. Zheng, L. Bradley, D. Patterson, M. Galushka, and J. Winder, "New Protocol for Leg Ulcer Tissue Classification from Colour Images," in *Proceedings of the 26th Annual International Conference of the IEEE EMBS*, pp. 1389-1392, 2004.

- [19] J. R. Mekkes, W. Westershof, M. Jan R, and W. Westerhof, "Image Processing in the Study of Wound Healing," *Clinics in Dermatology*, vol. 13, no. 4, pp. 401-407, 1995.
- [20] H. Wannous, S. Treuillet, and Y. Lucas, "A Complete 3D Wound Assessment Tool for Accurate Tissue Classification and Measurement," in *15th International Conference on Image Processing , ICIP*, pp. 2928-2931, 2008.
- [21] H. Wannous, S. Treuillet, and Y. Lucas, "Supervised Tissue Classification from Color Images for a Complete Wound Assessment Tool," in *29th Annual International Conference of the IEEE EMBS*, pp. 6031-6034, 2007.
- [22] R. R. Anderson and J. A. Parrish, "The Optics of Human Skin," *Journal of Investigative Dermatology*, vol. 77, no. 1, pp. 13-19, 1981.
- [23] E. Claridge, S. Cotton, P. Hall, and M. Moncrieff, "From Colour to Tissue Histology: Physics Based Interpretation of Images of Pigmented Skin Lesions," in *LNCS 2488*, pp. 730-738, 2002.
- [24] K. P. Nielsen, L. Zhao, J. J. Stamnes, K. Stamnes, and J. Moan, "The Optics of Human Skin : Aspects Important for Human Health," no. 1, pp. 35-46, 2008.
- [25] N. Tsumura, H. Haneishi, and Y. Miyake, "Independent Component Analysis of Skin Color Image," in *The 6th Color Imaging Conference: Color Science, Systems and Applications*, vol. 1, pp. 177-180, 1999.
- [26] H. Nugroho, A. M. H. Fadzil, S. Norashikin, and H. H. Suraiya, "Determination of Skin Repigmentation Progression," in *IEEE Engineering In Medicine And Biology Society*, pp. 3442-3445, 2007.
- [27] R. F. Diegelmann and M. C. Evans, "Wound Healing: An Overview of Acute, Fibrotic and Delayed Healing," *Frontiers in Bioscience*, vol. 9, no. 4, pp. 283-289, 2004.
- [28] T. K. Hunt, "Basic Principles of Wound Healing," *Journal of Trauma*, vol. 30, no. 12, pp. S122-8, Dec. 1990.
- [29] C. Pearson, "How Wounds Heal: A Guide for the Wound-Care Novice," *Wound Care Canada*, vol. 4, no. 2, pp. 10-4, 2006.
- [30] M. J. Callam, C. V. Ruckley, D. R. Harper, and J. J. Dale, "Chronic Ulceration of the Leg: Extent of the Problem and Provision of Care," *British Medical Journal (Clinical research ed.)*, vol. 290, no. 6485, pp. 1855-6, Jun. 1985.

- [31] J. V. Cornwall, C. J. Dore, and J. D. Lewis, "Leg Ulcers: Epidemiology and Aetiology," *British Journal of Surgery*, vol. 73, no. 9, pp. 693-6, 1986.
- [32] J. F. O'Brien, P. A. Grace, I. J. Perry, and B. P. E., "Prevalence and Aetiology of Leg Ulcers in Ireland," *Irish Journal of Medical Science*, vol. 169, no. 2, pp. 110-2, 2000.
- [33] O. Nelzén, D. Bergqvist, A. Lindhagen, and T. Hallböök, "Chronic Leg Ulcers: An Underestimated Problem in Primary Health Care Among Elderly Patients," *Journal of Epidemiology and Community Health*, vol. 45, no. 3, pp. 184-7, Sep. 1991.
- [34] M. C. Robson and A. Barbul, "Guidelines for the Best Care of Chronic Wounds," *Wound Repair and Regeneration*, vol. 14, no. 6, pp. 647-8, 2007.
- [35] "Leg Ulcers," *New Zealand Dermatological Society Incorporated*. pp. 1-6, 2008.
- [36] P. Hartman, Phase-Specific Wound Management of Venous Leg Ulcer, Medical Ed. Paul Hartmann AG, D-89522 Heidenheim, 2006.
- [37] S. E. S. E. Zimmet, "Venous Leg Ulcers: Modern Evaluation and Management," *Dermatologic Surgery*, vol. 25, no. 3, pp. 236-241, Mar. 1999.
- [38] "Assessment and Management of Venous Leg Ulcers," no. June. Registered Nurses' Association of Ontario, 2006.
- [39] J. Stamps, "Venous Ulcer with Exposed Tendon in Patient with Arterial Insufficiency Treated Successfully with Polymeric Membrane Dressings," in *WOCN Society 39th Annual Conference*, 2007.
- [40] R. Salcido and A. Popescu, "Pressure Ulcers and Wound Care," *Medscape*, 2009. [Online]. Available: <http://emedicine.medscape.com/article/319284-overview>. [Accessed: 18-Oct-2011].
- [41] "Decubitus Ulcers - Bed Sore Ulcer Information and Wound Stages," *LDHP Medical Review Services Corporation*, 1999. [Online]. Available: http://www.expertlaw.com/library/malpractice/decubitus_ulcers.html. [Accessed: 18-Oct-2011].
- [42] M. Murandu and C. Dealey, The Use of Granulated Sugar to Treat Two Pressure Ulcers. United Kingdom , pp. 1-6, 2009.

- [43] K. Vowden and P. Vowden, "Wound Bed Preparation," *World Wide Wounds*, 2002. [Online]. Available: <http://www.worldwidewounds.com/2002/april/Vowden/Wound-Bed-Preparation.html>. [Accessed: 19-Oct-2011].
- [44] R. G. Sibbald et al., "Preparing the Wound Bed--Debridement, Bacterial Balance, and Moisture Balance," *Ostomy Wound Management*, vol. 46, no. 11, pp. 14-22, 24-8, 30-5; quiz 36-7, Nov. 2000.
- [45] M. Collier, "The Elements of Wound Assessment," *Nursing times*, vol. 99, no. 13, pp. 48-9, 2003.
- [46] M. Müller, K. Morris, and K. Coleman, "Venous Leg Ulcer Management : The Royal Brisbane Hospital Leg Ulcer Clinic Experience," *Vascular*, no. November, pp. 162-166, 1999.
- [47] "Care of the Wound Bed Assessment and Management Algorithm." pp. 10-38, 2009.
- [48] "Wound Care Guidelines." East Lancashire Health Authority, pp. 1-48, 2001.
- [49] "Care of People with Chronic Leg Ulcers - An Evidence Based Guideline," *Ratio*, no. December. pp. 6-24, 1999.
- [50] C. Dealey, *The Care of Wounds - A Guide for Nurses*. pp. 13-78, 2005.
- [51] D. W. Craig et al., "Assessing and Managing Chronic Wounds - Wound Care Reference Guide," *Nature reviews. Genetics*, vol. 12, no. 10, pp. 730-6, Oct. 2011.
- [52] M. Callieri, P. Cignoni, P. Pingi, and R. Scopigno, "Derma : Monitoring the Evolution of Skin Lesions with a 3D System," in *Vision, Model. Visualizat*, pp. 167-174, 2003.
- [53] M. Galushka, H. Zheng, D. Patterson, and L. Bradley, "Case-Based Tissue Classification for Monitoring Leg Ulcer Healing," in *18th IEEE Symposium on Computer-Based Medical Systems (CBMS'05)*, pp. 353-358, 2005.
- [54] T. Igarashi, K. Nishino, and S. K. Nayar, *The Appearance of Human Skin*. New York, USA: , pp. 1-62, 2005.
- [55] M. D. Fairchild, "Human Color Vision in Color Appearance Models", 2nd ed., vol. 1, John Wiley & Sons, pp. 1-34, 2005.
- [56] C. Peterson, "How It Works: The Charged-Coupled Device, or CCD," *Journal of Young Investigators*, vol. 3, no. 1, 2001.

- [57] B. E. Bayer, "Color Imaging Array," U.S. Patent 39710651976.
- [58] B. Funt, K. Barnard, and L. Martin, "Is Machine Colour Constancy Good Enough?," in *5th European Conference of Computer Vision*, pp. 455-9, 1998.
- [59] S. Bianco, F. Gasparini, and R. Schettini, "Combining Strategies for White Balance," *In Proc. Digital Photography III*, vol. IS&T, 2007.
- [60] V. C. Cardei, B. Funt, and K. Barnard, "White Point Estimation for Uncalibrated Images," in *The IS& T/SID Seventh Color Imaging Conference*, pp. 97-100, 1999.
- [61] I. T. Jolliffe, *Principal Component Analysis*. Secausus, NJ, USA: Springer, 2002.
- [62] J. Shlens, "A Tutorial on Principal Component Analysis," *New York*. 2009.
- [63] L. I. Smith, "A Tutorial on Principal Components Analysis," *Statistics*. 2002.
- [64] D. C. Lay, *Linear Algebra and Its Applications*, 3rd ed. Pearson - Addison Wesley, 2006.
- [65] A. H. Gregory, E. U. Scott, H. M. Randy, and V. S. William, "Unsupervised Color Image Segmentation with Applications to Skin Tumor Borders," *IEEE Engineering In Medicine And Biology*, vol. 15, no. 1, pp. 104-111, 1996.
- [66] A. Hyvärinen and E. Oja, "Independent Component Analysis: Algorithms and Applications," *Neural Networks*, vol. 13, pp. 411-430, 2000.
- [67] S. Roberts and R. Everson, *Independent Component Analysis - Principles and Practice*. Cambridge, United Kingdom: Cambridge University Press, 2001.
- [68] T. W. Lee, *Independent Component Analysis - Theory and Applications*. Dordrecht, Netherlands: Kluwer Academic Publishers, pp. 27-62, 1998.
- [69] A. Hyvärinen and E. Oja, "Fast and Robust Fixed-Point Algorithms for Independent Component Analysis," *IEEE Transactions on Neural Networks*, vol. 10, no. 3, pp. 626-634, 1999.
- [70] A. Hyvärinen and E. Oja, "A Fast Fixed-Point Algorithm for Independent Component Analysis," *Neural Computation*, vol. 9, pp. 1483-1492, 1997.
- [71] D. Langlois, S. Chartier, and D. Gosselin, "An Introduction to Independent Component Analysis: InfoMax and FastICA algorithms," *Tutorials in Quantitative Methods for Psychology*, vol. 6, no. 1, pp. 31-38, 2010.

- [72] A. Hyvärinen, "New Approximations of Differential Entropy for Independent Component Analysis and Projection Pursuit," in *Advances in Neural Information Processing Systems 10 (NIPS'98)*, 1998, vol. 10, pp. 273-279.
- [73] G. Fung, "A Comprehensive Overview of Basic Clustering Algorithms." pp. 1-37, 2001.
- [74] R. Xu and W. Donald, "Survey of Clustering Algorithms," *IEEE Transactions on Neural Networks*, vol. 16, no. 3, pp. 645-678, 2005.
- [75] J. C. Bezdek, R. Ehrlich, and W. Full, "FCM: The Fuzzy c-means Clustering Algorithm," *Computers & Geosciences*, vol. 10, no. 2, pp. 191-203, 1984.
- [76] R. O. Duda, P. E. Hart, and D. G. Stork, *Pattern Classification - Unsupervised Classification and Clustering*, 2nd ed. Pearson, pp. 528-530, 2000.
- [77] N. Otsu, "A Threshold Selection Method from Gray-Level Histograms," in *IEEE Transactions on Systems, Man and Cybernetics*, vol. C, no. 1, pp. 62-66, 1979.
- [78] R. C. Gonzalez and R. E. Woods, *Digital Image processing*, 3rd ed. Pearson - Prentice Hall, pp. 764-778, 2010.
- [79] R. C. Gonzalez and R. E. Woods, *Digital Image Processing*, 3rd ed. Pearson - Prentice Hall, pp. 166-179, 2010.
- [80] R. Dawson, "How Significant Is A Boxplot Outlier?," *Journal of Statistics Education*, vol. 19, no. 2, pp. 1-12, 2011.
- [81] W. Zhu, N. Zeng, and N. Wang, "Sensitivity , Specificity , Accuracy , Associated Confidence Interval and ROC Analysis with Practical SAS ® Implementations," *NESUG 2010 - Health Care and Life Sciences*, pp. 1-9, 2010.
- [82] A. K. Akobeng, "Understanding diagnostic tests 1 : sensitivity , specificity and predictive values," *Acta Paediatrica*, no. 96, pp. 338-341, 2007.

LIST OF PUBLICATIONS

1. F. M. Hani, L. Arshad, A. S. Malik, A. Jamil, B. B. Felix Yap, “Digital Image Analysis of Chronic Ulcers Tissues”, 5th Kuala Lumpur International Conference on Biomedical Engineering 2011, IFMBE Proceedings, Vol. 35, pp. 635-638, 2011.
2. Ahmad Fadzil M. Hani, Leena Arshad, Aamir Saeed Malik, Adawiyah Jamil, Felix Yap Boon Bin, “Assessment of chronic ulcers using digital imaging”, National Postgraduate Conference – Energy and Sustainability: Exploring the innovative Minds, NPC’11, 2011.
3. Ahmad Fadzil M. Hani, Leena Arshad, Aamir Saeed Malik, Adawiyah Jamil, Felix Yap Boon Bin, “Segmentation of Granulation Tissue in Chronic Ulcers”, Journal of Australian Physical and Engineering Sciences In Medicine, Vol. 34, pp. 592, 2011.
4. Hani, A. F. M., Arshad, L., Malik, A. S., Bin, F. Y. B., “ Detection and classification of granulation tissue in chronic ulcers”, Lecture Notes in Computer Science (including subseries Lecture Notes in Artificial Intelligent and Lecture Note in Bioinformatics), 7066 LNCS (Part 1), pp. 139-150, 2011.
5. Ahmad Fadzil M. Hani, Leena Arshad, Aamir Saeed Malik, Adawiyah Jamil, Felix Yap Boon Bin, “Heamoglobin Distribution in Ulcers for Healing Assessment”, 4th International Conference on Intelligent and Advanced Systems (ICIAS’12), Vol. 1, pp. 362-367, 2012.
6. A. Fadzil, L. Ahmed, A. Malik, A. Jamil, F. B. Bin, “Heamoglobin Distribution in Ulcers for Healing Assessment”, Journal of Investigative Dermatology, Iss. 132 *Angiogenesis, Vascular Biology and Wound Healing*, S13, 2012.
7. Hani, A. F. M., Eltigani, N.M., Arshad, L., Hussein, S. H., Jamil, A., Gill, P., “Wound model reconstruction from three-dimensional skin surface imaging

using the convex hull approximation method”, IET Image Processing, Vol. 6, Iss. 5, pp. 521-533, 2012.

8. Patent Filed: Methodology and Apparatus for Objective and in vivo Assessment of Granulation Tissue Growth in Chronic Ulcers using Digital Imaging, MYIPO - PI 2012000550, 2012.
9. Technical Exhibitions:
 - Malaysia Technology Expo 2012 (MTE'12) 2012 - Silver Medal.
 - 23rd International Invention, Innovation and Technology Exhibition 2012 (ITEX'12) - Silver Medal.
 - British Invention Show 2012 (BIS'12) - Silver Medal.

APPENDIX A

STUDY INFORMATION SHEETS AND PATIENT CONSENT FORMS

PATIENT INFORMATION SHEET

Study Title: Digital Image Analysis of Chronic Ulcers Tissues

Investigators: Leena Arshad Mohammed Ahmed

Dr. Felix Boon Bin

Institution address:

1. Department of Dermatology/Outpatient Department
Hospital Kuala Lumpur
Jalan Pahang
50586 Kuala Lumpur

2. Universiti Teknologi PETRONAS
Bandar Seri Iskandar
31750 Tronoh
Perak Darul Ridzuan

INTRODUCTION

You are invited to participate in a study conducted by the Department of Dermatology Hospital Kuala Lumpur, Outpatient Department Hospital Kuala Lumpur and Universiti Teknologi PETRONAS. This is because you have a condition called chronic leg ulcer. As a potential research subject, you have the right to know the consequences of participating in this study. The following information explains the possible benefits and risks of being in the study to help you make a decision about participation. Your participation in this study is strictly voluntary and you have no obligations to participate whatsoever.

It is important that you read this document thoroughly and discuss any queries with your doctor or anyone else you prefer before agreeing to participate. Your signature, dated, on the consent form is required before the researchers can perform study procedures on you.

PURPOSE OF THE STUDY

Leg ulcer is a chronic disease that is difficult to cure. It is a significant health and socioeconomic issue. It is a difficult condition to treat. It causes considerable discomfort, and limitations in social activities to the patient. Treatment of leg ulcer is time consuming and

often not very effective. In this study, we aim to build a new method for doctors to assess your ulcer condition in a more objective way.

WHO WOULD THIS STUDY INVOLVE

This study will involve patients who had been diagnosed to have chronic leg ulcer.

WHAT WILL HAPPEN TO THE PARTICIPANTS AND THE INFORMATION OBTAINED IN THIS STUDY?

Coloured photographs of the ulcer on your leg will be taken using a camera. You may be asked to move your leg in a few positions in order to get a good photograph. All medications and other treatment for your ulcer will be continued as usual. The information obtained in this study will be analyzed and the results will help us in the management of patients with leg ulcers in the future.

POTENTIAL BENEFITS OF THE STUDY

The results of this study may be able to help doctors to assess your ulcer condition more objectively. Your participation may contribute to the way doctors assess or examine leg ulcers in the future.

POTENTIAL RISKS OF THE STUDY

This study will involve taking photographs of your leg ulcer only. There are no expected risks, discomfort and radiation that could cause long term consequences associated with the study.

VOLUNTARY PARTICIPATION

Participation in this study is strictly voluntary. If you decide to participate in the study, you are expected to comply with the study requirements. You are allowed to withdraw from the study at any time without penalty or loss of benefits to which you are otherwise entitled. We will be interested to know if the reason for withdrawal is due to adverse events experienced.

CONFIDENTIALITY

All information given by you are confidential. Reports prepared on the study will not include your name or other identification. Information and records may be reviewed by the Institutional Review Board (IRB)/Ethics Committee (EC) and other regulatory authorities to determine the accuracy of the reported data and/or to protect your safety and welfare.

STUDY COSTS/COMPENSATION

This research does not require any payment from you and neither will you get paid or receive any rewards for your participation. The cost of your ulcer treatment will remain the same whether you participate in this research or not. This research does not provide compensation for any problems that may occur.

TREATMENT OF STUDY RELATED INJURY

In the event that you suffer an injury or side effects or complications that is a direct consequence of the study, the attending doctor will be notified and you will be managed appropriately in Hospital Kuala Lumpur.

ETHICAL REVIEW

This study has been reviewed and approved by the Medical Research & Ethics Committee, Ministry of Health Malaysia.

CONTACT NUMBERS

If you have any enquiries regarding the study or experience any side effects of the study, please contact

Dr. Felix Yap Boon Bin

Dermatology Clinic Hospital Kuala Lumpur

03-5555259 or 03-5556687

CONSENT FORM

Study Title: Digital Image Analysis of Chronic Ulcers Tissues

I have read the information on the research project stated above and have been given the explanation by a doctor about the purpose of this document. I understand that I retained the absolute right over the information given and I have the absolute right to withdraw from the study at any time.

I _____ IC Number: _____ have received a copy of the Patient Information Sheet on the above study and agreed to participate in the study.

Patient/Person giving consent

Name : _____
Signature : _____
Identity Card : _____
Date : _____
Tel : _____

Requesting Researcher

Name : _____
Signature : _____
Identity Card : _____
Date : _____
Tel : _____

Requesting Doctor

Name : _____
Signature : _____
Identity Card : _____
Date : _____
Tel : _____

PHOTOGRAPHY REQUEST FORM

Study Title: Digital Image Analysis of Chronic Ulcers Tissues

I have read the information on the research project stated above and have been given the explanation by a doctor about the purpose of this document. I understand that I retained the absolute right over the information given and I have the absolute right to withdraw from the study at any time.

I _____ IC Number: _____, give my consent for photographs to be taken, as indicated above, of the said patient and for the photographs to be used by the research and academic purposes only.

I understand that the research authorities will, to the best of their ability, protect my identity in the event that the photographs are reproduced in the teaching sessions, academic discussions/meeting and medical/scientific journals.

Patient/Person giving consent

Name : _____
Signature : _____
Identity Card : _____
Date : _____
Tel : _____

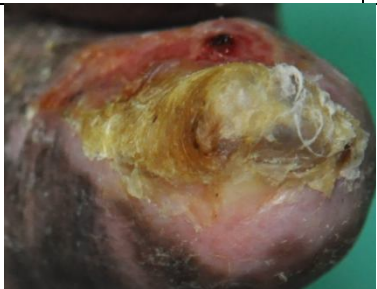
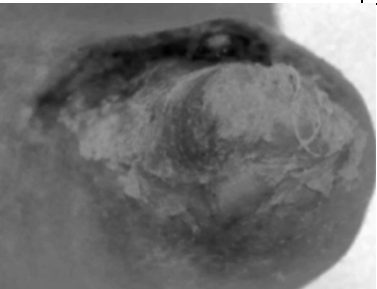

Requesting Researcher


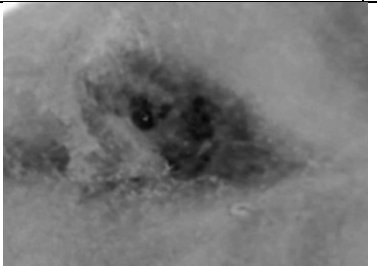

Name : _____
Signature : _____
Identity Card : _____
Date : _____
Tel : _____


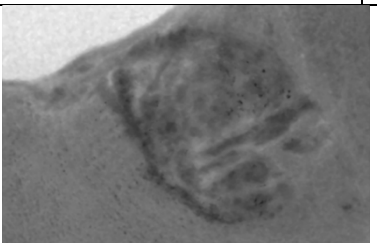
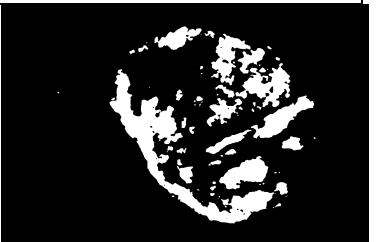
Requesting Doctor


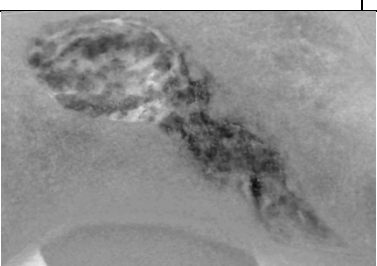

Name : _____
Signature : _____
Identity Card : _____
Date : _____
Tel : _____

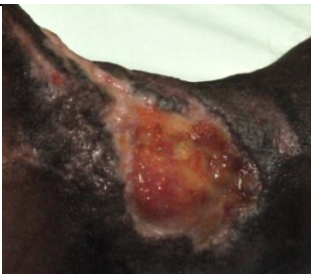
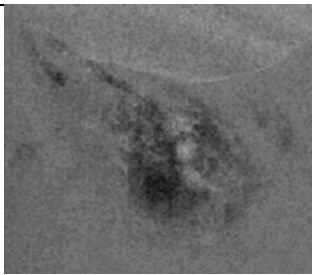
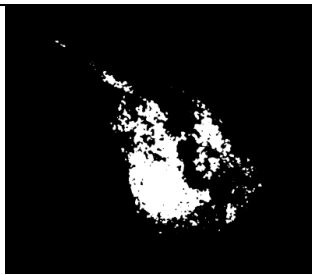
APPENDIX B
THE ORIGINAL COLOUR IMAGES, THE EXTRACTED HAEMOGLOBIN IMAGES,
AND THE DETECTED GRANULATION IMAGES


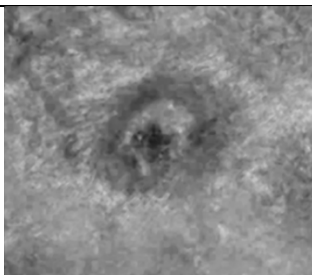
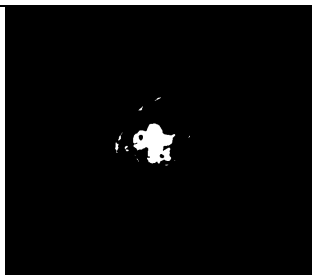
Ulcer No.: P1-1		Date Image was Taken : 19/03/2010 - Dermatology
Colour Ulcer Image	Haemoglobin Image	Granulation Segmentation
		

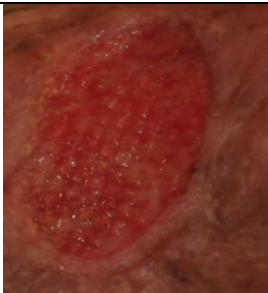
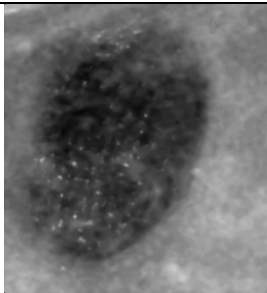
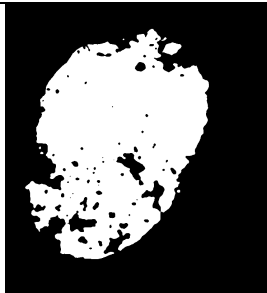
Ulcer No.: P1-2		Date Image was Taken: 19/03/2010 - Dermatology
Colour Ulcer Image	Haemoglobin Image	Granulation Segmentation
		


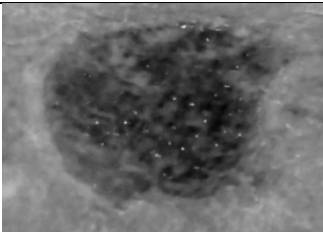
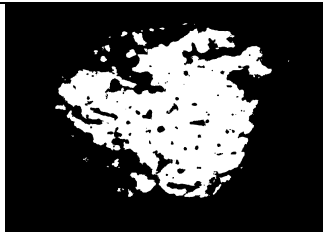
Ulcer No.: P2-1		Date Image was Taken: 19/03/2010 - Dermatology
Colour Ulcer Image	Haemoglobin Image	Granulation Segmentation
		

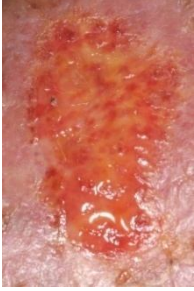
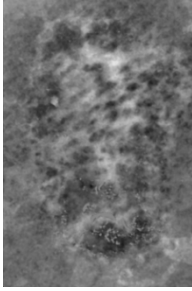

Ulcer No.: P2-3		Date Image was Taken: 19/03/2010 - Dermatology
Colour Ulcer Image	Haemoglobin Image	Granulation Segmentation
		




Ulcer No.: P2-4		Date Image was Taken: 07/01/2011 - Dermatology	
Colour Ulcer Image	Haemoglobin Image	Granulation Segmentation	
			

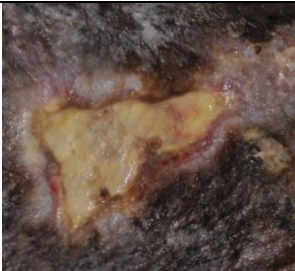


Ulcer No.: P3-1		Date Image was Taken: 23/04/2010 - Dermatology	
Colour Ulcer Image	Haemoglobin Image	Granulation Segmentation	
			


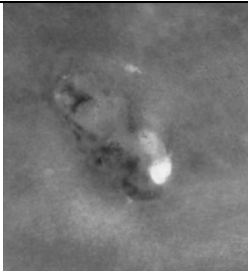

Ulcer No.: P3-2		Date Image was Taken: 18/01/2011 - Dermatology	
Colour Ulcer Image	Haemoglobin Image	Granulation Segmentation	
			


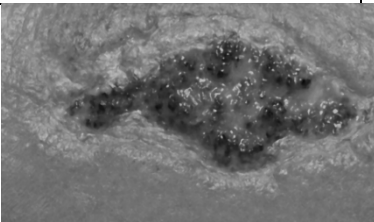
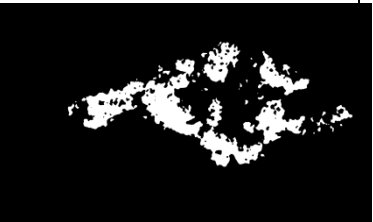
Ulcer No.: P3-3		Date Image was Taken: 18/01/2011 - Dermatology	
Colour Ulcer Image	Haemoglobin Image	Granulation Segmentation	
			


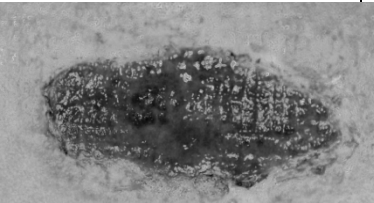

Ulcer No.: P5		Date Image was Taken: 30/04/2010 - Dermatology	
Colour Ulcer Image	Haemoglobin Image	Granulation Segmentation	
			

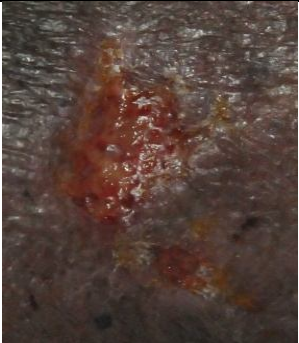
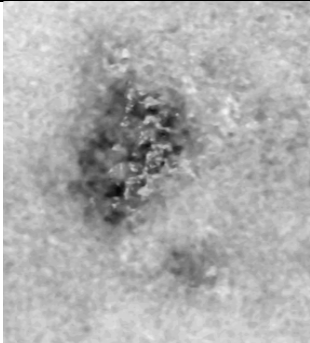

Ulcer No.: P6-1		Date Image was Taken: 23/04/2010 - Dermatology	
Colour Ulcer Image	Haemoglobin Image	Granulation Segmentation	
			


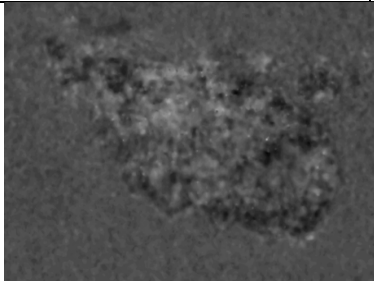
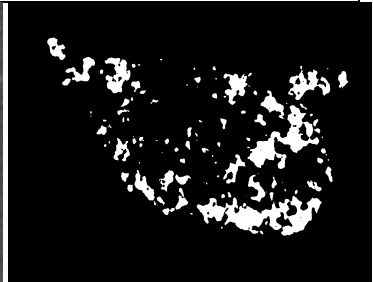
Ulcer No.: P6-1		Date Image was Taken: 23/04/2010 - Dermatology	
Colour Ulcer Image	Haemoglobin Image	Granulation Segmentation	
			

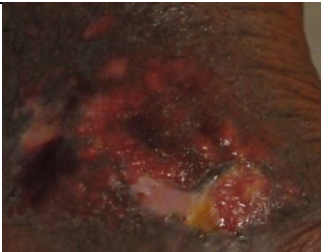
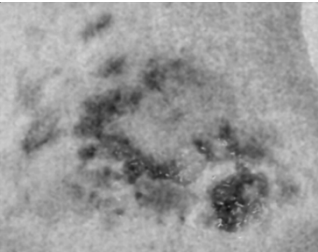
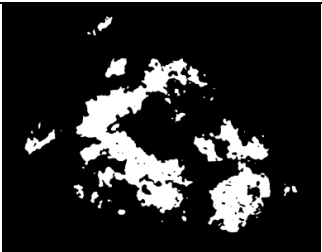
Ulcer No.: P10-1		Date Image was Taken: 14/05/2010 - Dermatology	
Colour Ulcer Image	Haemoglobin Image	Granulation Segmentation	
			

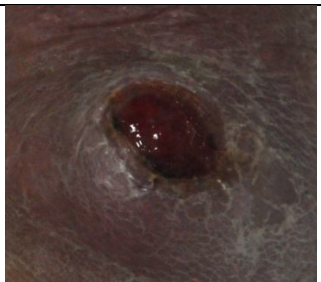
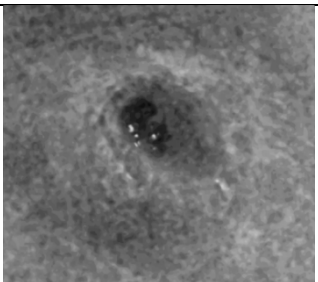
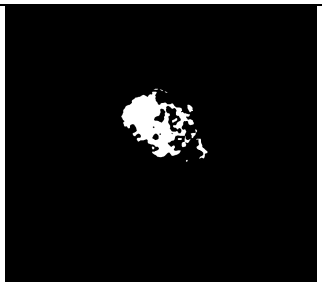
Ulcer No.: P12-1		Date Image was Taken: 21/05/2010 - Dermatology
Colour Ulcer Image	Haemoglobin Image	Granulation Segmentation
		


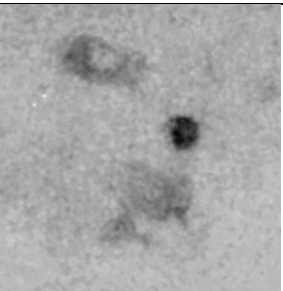
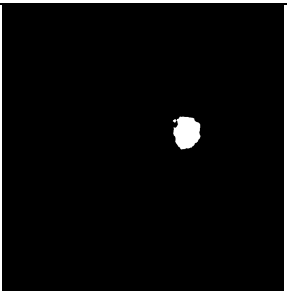
Ulcer No.: P12-3		Date Image was Taken: 21/05/2010 - Dermatology
Colour Ulcer Image	Haemoglobin Image	Granulation Segmentation
		




Ulcer No.: P13		Date Image was Taken: 17/12/2010 - Dermatology
Colour Ulcer Image	Haemoglobin Image	Granulation Segmentation
		


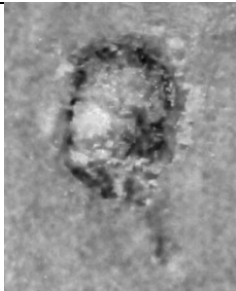

Ulcer No.: P14		Date Image was Taken: 07/01/2011 - Dermatology
Colour Ulcer Image	Haemoglobin Image	Granulation Segmentation
		


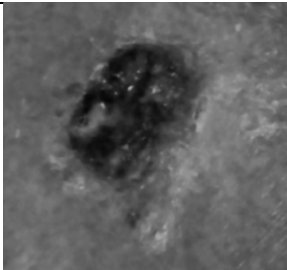

Ulcer No.: P16		Date Image was Taken: 17/12/2010 - Dermatology	
Colour Ulcer Image	Haemoglobin Image	Granulation Segmentation	
			


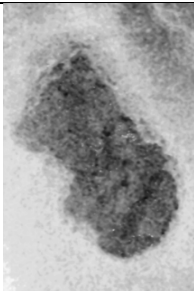

Ulcer No.: P17		Date Image was Taken: 07/01/2011 - Dermatology	
Colour Ulcer Image	Haemoglobin Image	Granulation Segmentation	
			

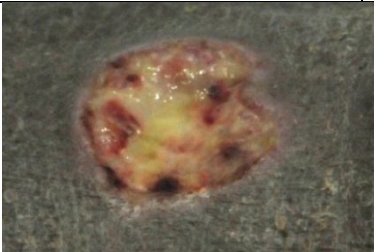
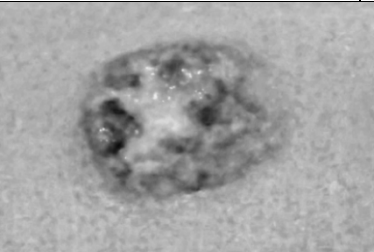
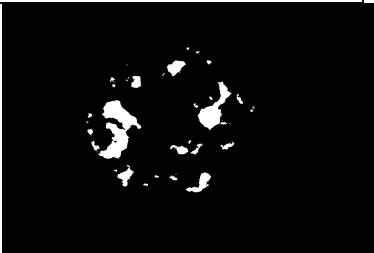
Ulcer No.: P18-1		Date Image was Taken: 07/01/2011 - Dermatology	
Colour Ulcer Image	Haemoglobin Image	Granulation Segmentation	
			

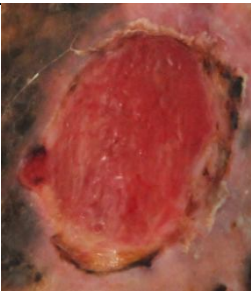
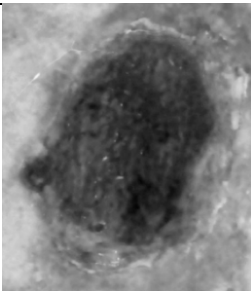
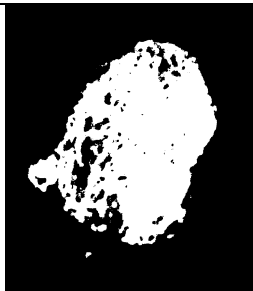
Ulcer No.: P18-2		Date Image was Taken: 07/01/2011 - Dermatology	
Colour Ulcer Image	Haemoglobin Image	Granulation Segmentation	
			

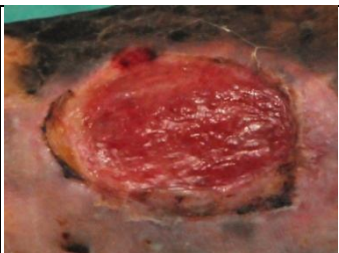
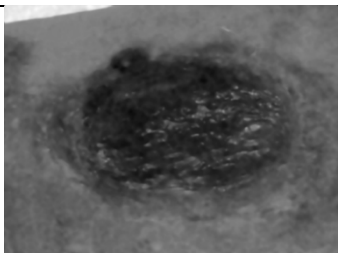

Ulcer No.: P19-1 Date Image was Taken: 07/01/2011 - Dermatology		
Colour Ulcer Image	Haemoglobin Image	Granulation Segmentation
		


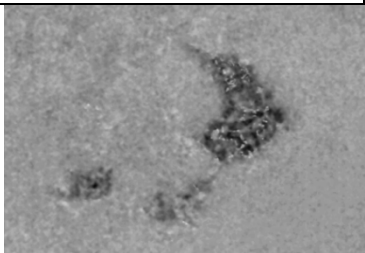

Ulcer No.: P19-2 Date Image was Taken: 14/01/2011 - Dermatology		
Colour Ulcer Image	Haemoglobin Image	Granulation Segmentation
		

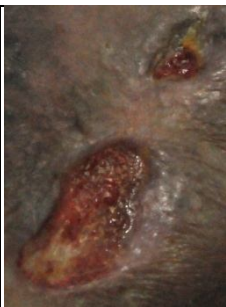
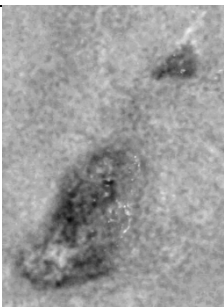

Ulcer No.: P20 Date Image was Taken: 07/01/2011 - Dermatology		
Colour Ulcer Image	Haemoglobin Image	Granulation Segmentation
		


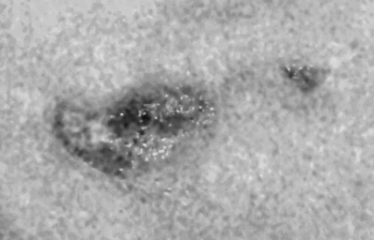

Ulcer No.: P21 Date Image was Taken: 11/02/2011 - Dermatology		
Colour Ulcer Image	Haemoglobin Image	Granulation Segmentation
		


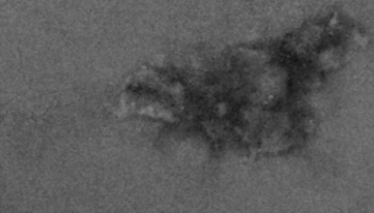

Ulcer No.: P23-1		Date Image was Taken: 11/02/2011 - Dermatology	
Colour Ulcer Image	Haemoglobin Image	Granulation Segmentation	
			


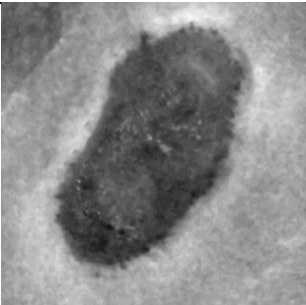

Ulcer No.: P23-2		Date Image was Taken: 11/02/2011 - Dermatology	
Colour Ulcer Image	Haemoglobin Image	Granulation Segmentation	
			

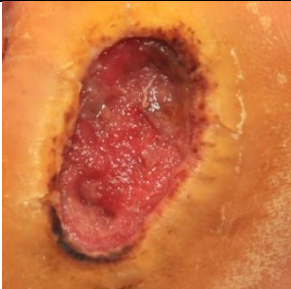
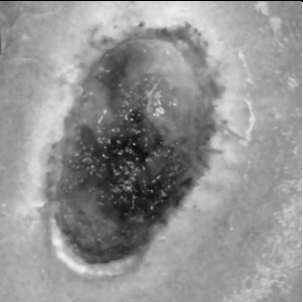

Ulcer No.: P24		Date Image was Taken: 11/02/2011 - Dermatology	
Colour Ulcer Image	Haemoglobin Image	Granulation Segmentation	
			


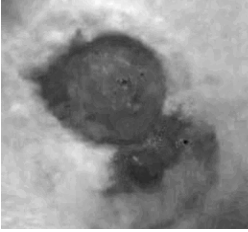

Ulcer No.: P25-1		Date Image was Taken: 11/02/2011 - Dermatology	
Colour Ulcer Image	Haemoglobin Image	Granulation Segmentation	
			

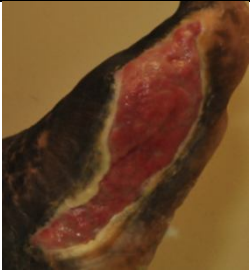
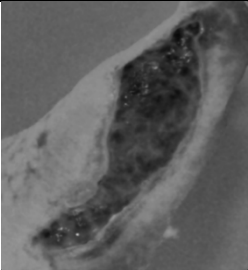

Ulcer No.: P25-2		Date Image was Taken: 11/02/2011 - Dermatology
Colour Ulcer Image	Haemoglobin Image	Granulation Segmentation
		


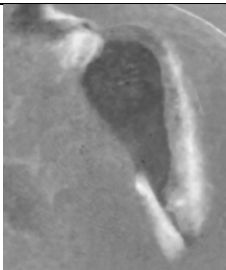
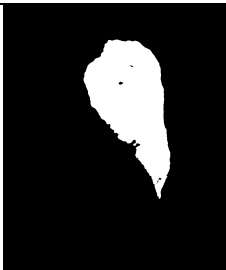
Ulcer No.: XX		Date Image was Taken: 11/02/2011 - Dermatology
Colour Ulcer Image	Haemoglobin Image	Granulation Segmentation
		


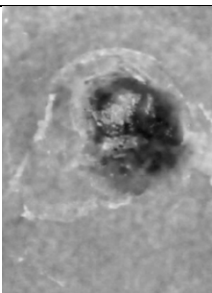
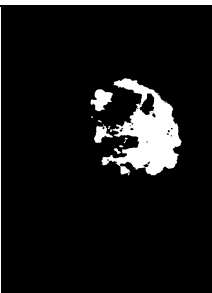
Ulcer No.: P2-1		Date Image was Taken: 12/01/2011 - OPD
Colour Ulcer Image	Haemoglobin Image	Granulation Segmentation
		


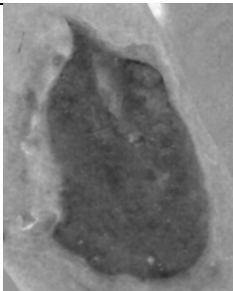

Ulcer No.: P2-2		Date Image was Taken: 23/02/2011 - OPD
Colour Ulcer Image	Haemoglobin Image	Granulation Segmentation
		


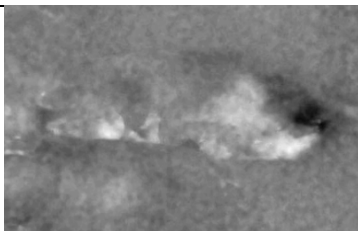

Ulcer No.: P2-3			Date Image was Taken: 12/01/2011 - OPD		
Colour Ulcer Image		Colour Ulcer Image		Colour Ulcer Image	
					


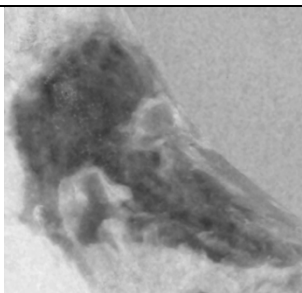
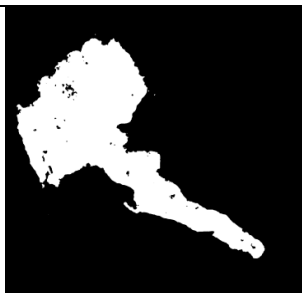
Ulcer No.: P3-1			Date Image was Taken: 12/01/2011 - OPD		
Colour Ulcer Image		Colour Ulcer Image		Colour Ulcer Image	
					

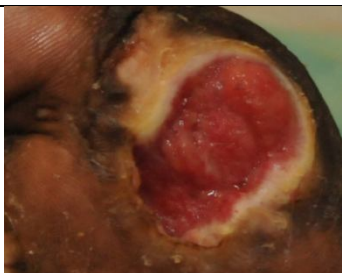
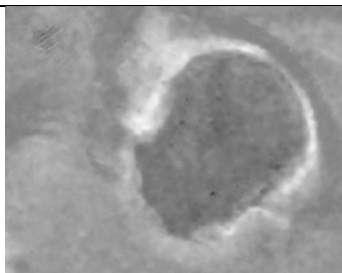

Ulcer No.: P3-3			Date Image was Taken: 23/02/2011 - OPD		
Colour Ulcer Image		Colour Ulcer Image		Colour Ulcer Image	
					

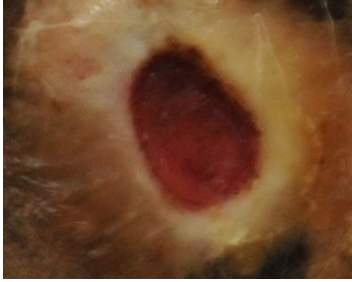
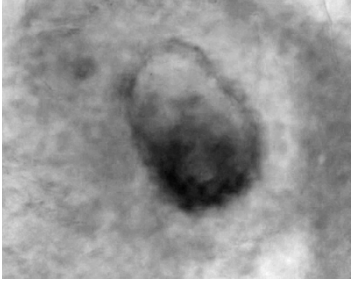
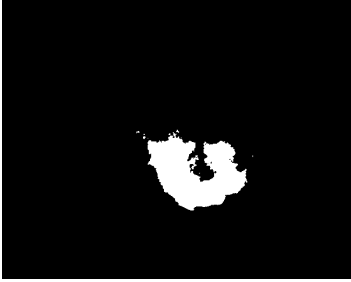
Ulcer No.: P7			Date Image was Taken: 11/02/2011 - OPD		
Colour Ulcer Image		Colour Ulcer Image		Colour Ulcer Image	
					


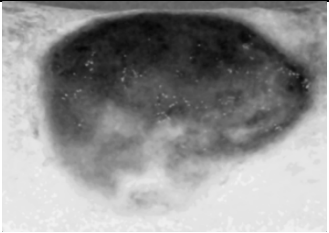

Ulcer No.: P9		Date Image was Taken: 18/01/2011 - OPD
Colour Ulcer Image	Colour Ulcer Image	Colour Ulcer Image
		

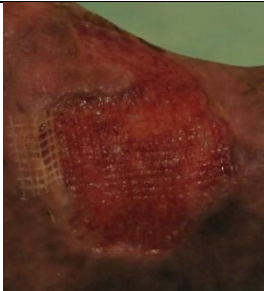
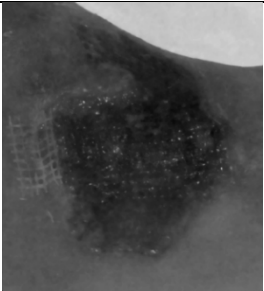

Ulcer No.: P11		Date Image was Taken: 18/01/2011 - OPD
Colour Ulcer Image	Colour Ulcer Image	Colour Ulcer Image
		

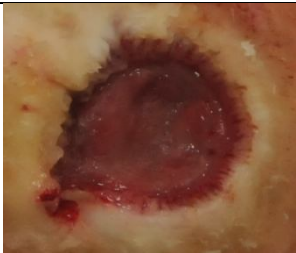
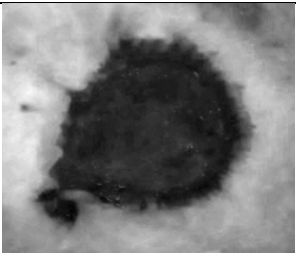

Ulcer No.: P11		Date Image was Taken: 18/01/2011 - OPD
Colour Ulcer Image	Colour Ulcer Image	Colour Ulcer Image
		

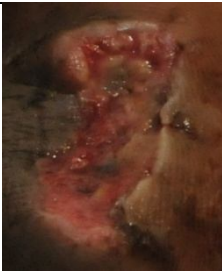

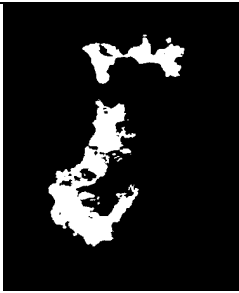
Ulcer No.: P14-1		Date Image was Taken: 18/01/2011 - OPD
Colour Ulcer Image	Colour Ulcer Image	Colour Ulcer Image
		

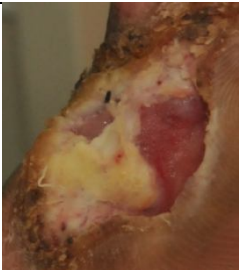
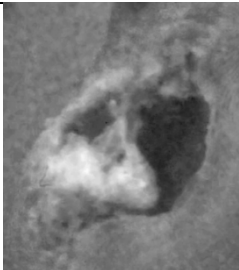

Ulcer No.: P14-5			Date Image was Taken: 18/01/2011 - OPD		
Colour Ulcer Image		Colour Ulcer Image		Colour Ulcer Image	
					


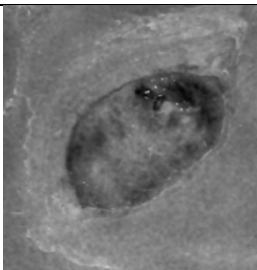

Ulcer No.: P15			Date Image was Taken: 18/01/2011 - OPD		
Colour Ulcer Image		Colour Ulcer Image		Colour Ulcer Image	
					

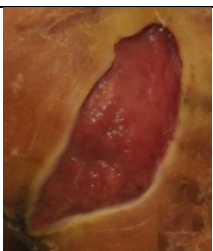
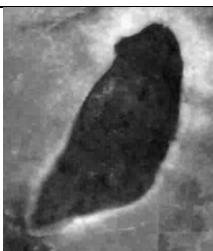

Ulcer No.: P16			Date Image was Taken: 18/01/2011 - OPD		
Colour Ulcer Image		Colour Ulcer Image		Colour Ulcer Image	
					

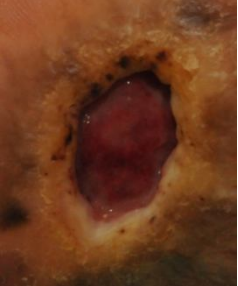
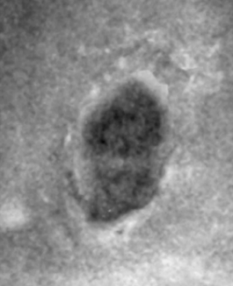
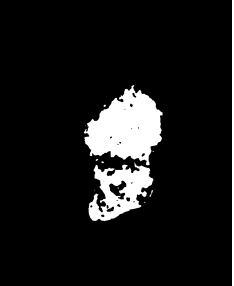
Ulcer No.: P17			Date Image was Taken: 18/01/2011 - OPD		
Colour Ulcer Image		Colour Ulcer Image		Colour Ulcer Image	
					


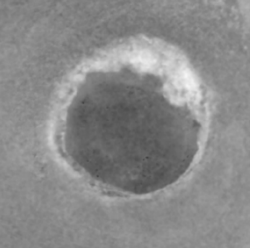

Ulcer No.: P18		Date Image was Taken: 18/01/2011 - OPD	
Colour Ulcer Image	Colour Ulcer Image	Colour Ulcer Image	
			


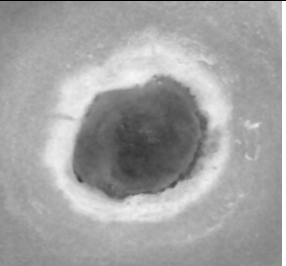

Ulcer No.: P21		Date Image was Taken: 19/01/2011 - OPD	
Colour Ulcer Image	Colour Ulcer Image	Colour Ulcer Image	
			

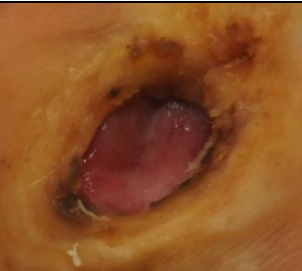
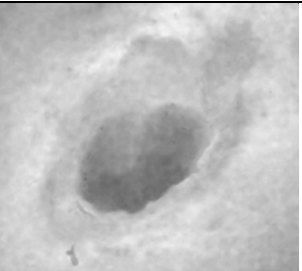
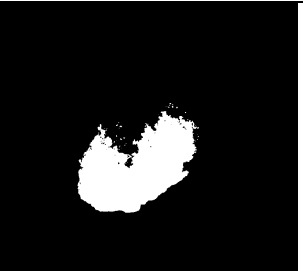
Ulcer No.: P22		Date Image was Taken: 19/01/2011 - OPD	
Colour Ulcer Image	Colour Ulcer Image	Colour Ulcer Image	
			

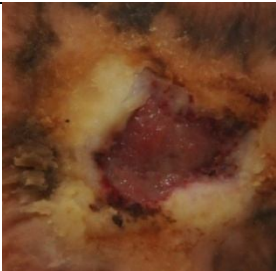
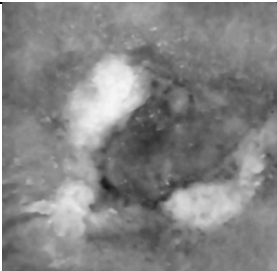
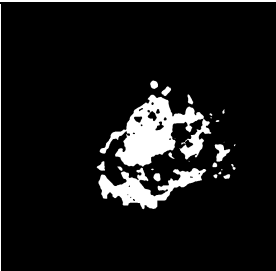
Ulcer No.: P23		Date Image was Taken: 19/01/2011 - OPD	
Colour Ulcer Image	Colour Ulcer Image	Colour Ulcer Image	
			


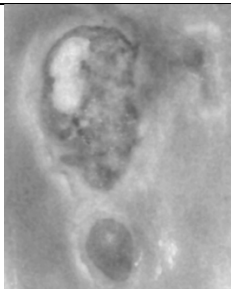
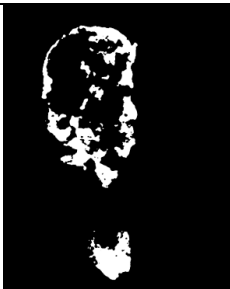
Ulcer No.: P24		Date Image was Taken: 27/01/2011 - OPD	
Colour Ulcer Image	Colour Ulcer Image	Colour Ulcer Image	
			


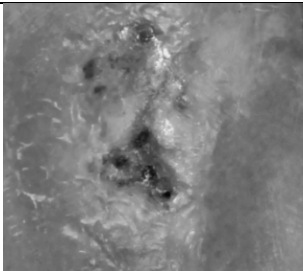
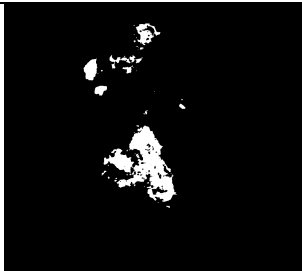
Ulcer No.: P25-1		Date Image was Taken: 27/01/2011 - OPD	
Colour Ulcer Image	Colour Ulcer Image	Colour Ulcer Image	
			


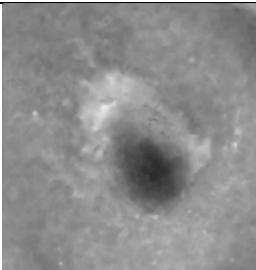
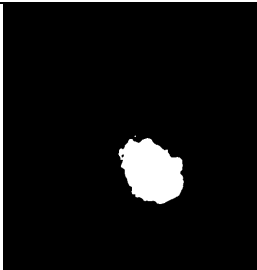
Ulcer No.: P25-2		Date Image was Taken: 24/02/2011 - OPD	
Colour Ulcer Image	Colour Ulcer Image	Colour Ulcer Image	
			


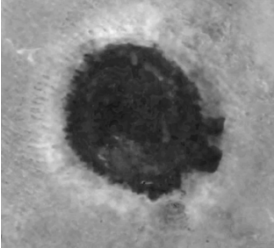
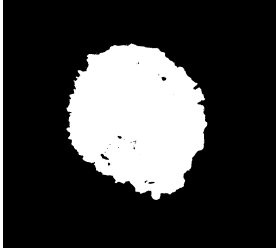
Ulcer No.: P26		Date Image was Taken: 27/01/2011 - OPD	
Colour Ulcer Image	Colour Ulcer Image	Colour Ulcer Image	
			

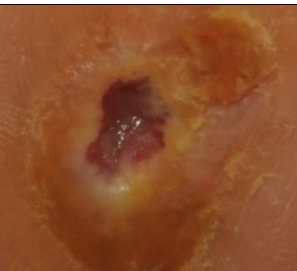
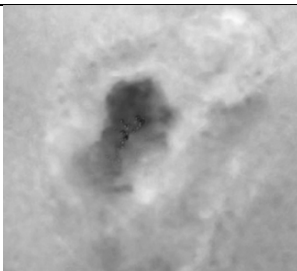

Ulcer No.: P27		Date Image was Taken: 27/01/2011 - OPD	
Colour Ulcer Image	Colour Ulcer Image	Colour Ulcer Image	
			

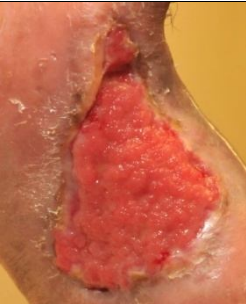
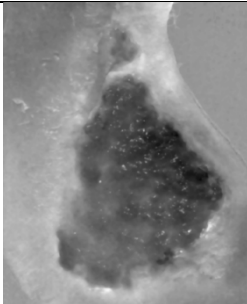

Ulcer No.: P28-1		Date Image was Taken: 27/01/2011 - OPD	
Colour Ulcer Image	Colour Ulcer Image	Colour Ulcer Image	
			

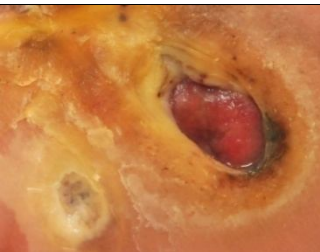
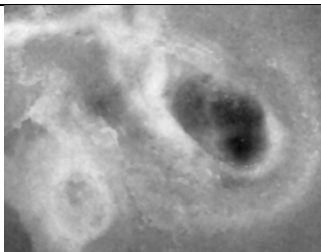

Ulcer No.: P28-2		Date Image was Taken: 24/02/2011 - OPD	
Colour Ulcer Image	Colour Ulcer Image	Colour Ulcer Image	
			


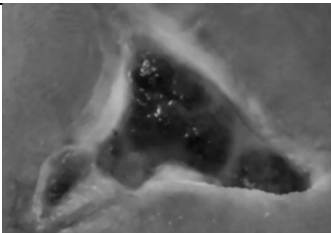

Ulcer No.: P28-3		Date Image was Taken: 27/01/2011 - OPD	
Colour Ulcer Image	Colour Ulcer Image	Colour Ulcer Image	
			

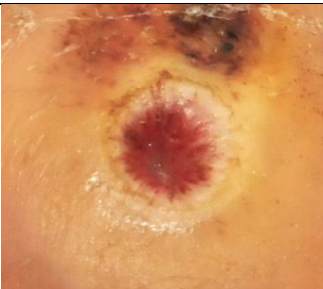
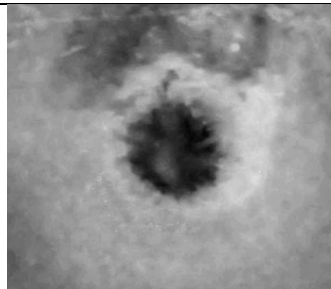
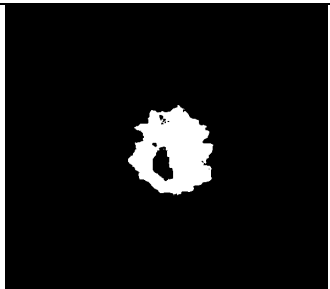
Ulcer No.: P28-4		Date Image was Taken: 24/02/2011 - OPD	
Colour Ulcer Image	Colour Ulcer Image	Colour Ulcer Image	
			

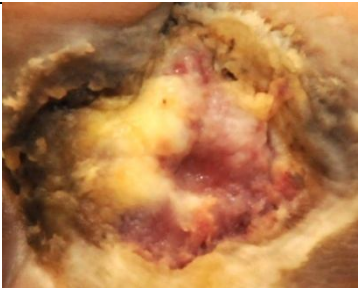
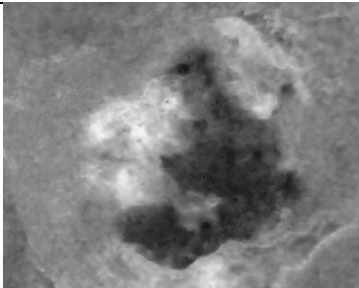

Ulcer No.: P29		Date Image was Taken: 27/01/2011 - OPD	
Colour Ulcer Image	Colour Ulcer Image	Colour Ulcer Image	
			

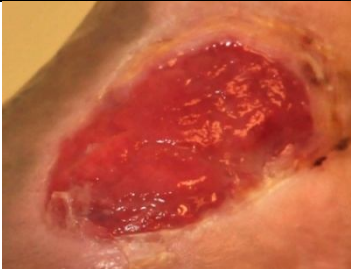
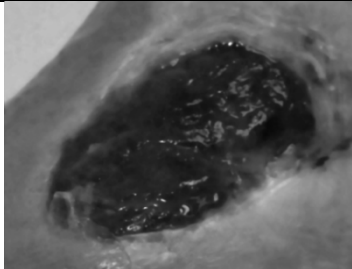

Ulcer No.: P30		Date Image was Taken: 11/02/2011 - OPD	
Colour Ulcer Image	Colour Ulcer Image	Colour Ulcer Image	
			


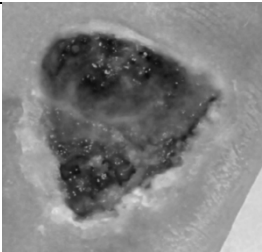
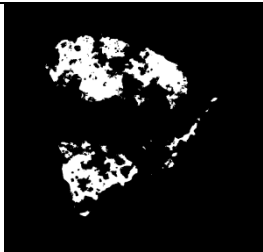
Ulcer No.: P31		Date Image was Taken: 11/02/2011 - OPD	
Colour Ulcer Image	Colour Ulcer Image	Colour Ulcer Image	
			

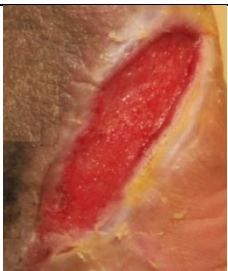
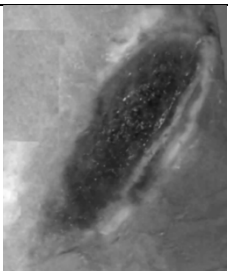

Ulcer No.: P32-1			Date Image was Taken: 11/02/2011 - OPD		
Colour Ulcer Image		Colour Ulcer Image		Colour Ulcer Image	
					

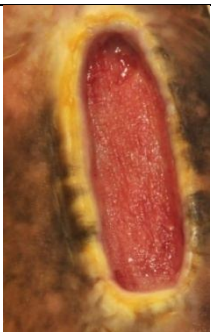
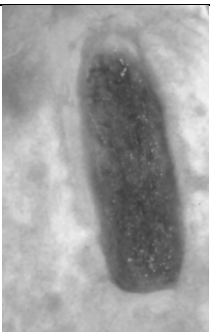

Ulcer No.: P32-2			Date Image was Taken: 11/02/2011 - OPD		
Colour Ulcer Image		Colour Ulcer Image		Colour Ulcer Image	
					

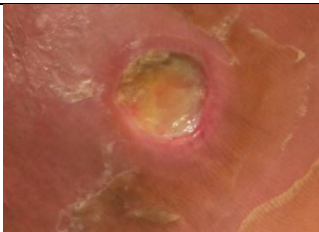
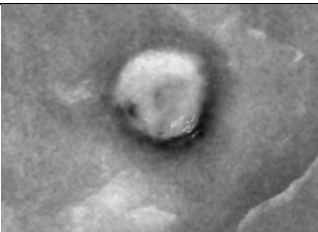
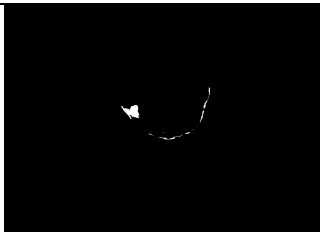
Ulcer No.: P33			Date Image was Taken: 11/02/2011 - OPD		
Colour Ulcer Image		Colour Ulcer Image		Colour Ulcer Image	
					


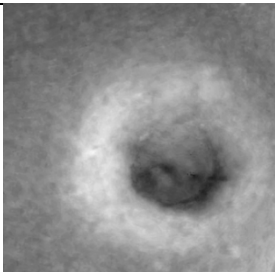
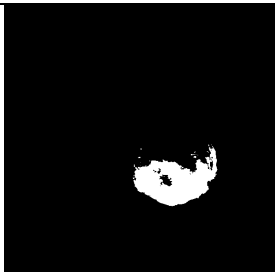
Ulcer No.: P35			Date Image was Taken: 22/02/2011 - OPD		
Colour Ulcer Image		Colour Ulcer Image		Colour Ulcer Image	
					

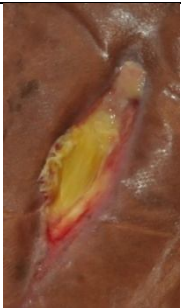
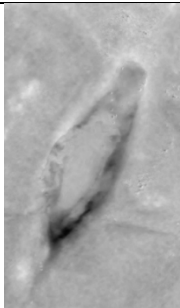

Ulcer No.: P36 Date Image was Taken: 22/02/2011 - OPD		
Colour Ulcer Image	Colour Ulcer Image	Colour Ulcer Image
		


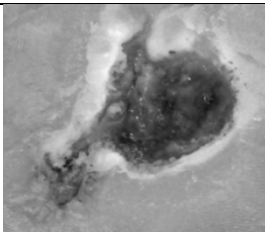

Ulcer No.: P38 Date Image was Taken: 23/02/2011 - OPD		
Colour Ulcer Image	Colour Ulcer Image	Colour Ulcer Image
		


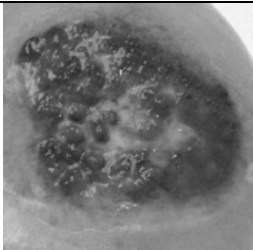
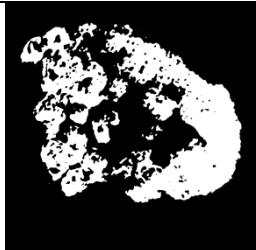
Ulcer No.: P39 Date Image was Taken: 23/02/2011 - OPD		
Colour Ulcer Image	Colour Ulcer Image	Colour Ulcer Image
		


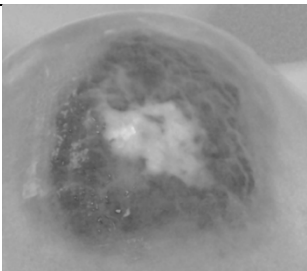
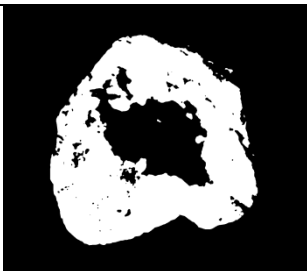
Ulcer No.: P40-1 Date Image was Taken: 23/02/2011 - OPD		
Colour Ulcer Image	Colour Ulcer Image	Colour Ulcer Image
		


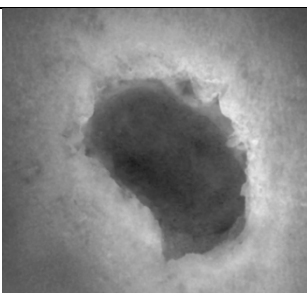

Ulcer No.: P40-2		Date Image was Taken: 23/02/2011 - OPD	
Colour Ulcer Image	Colour Ulcer Image	Colour Ulcer Image	
			


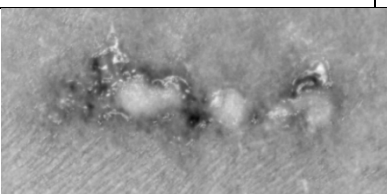

Ulcer No.: P41-2		Date Image was Taken: 24/02/2011 - OPD	
Colour Ulcer Image	Colour Ulcer Image	Colour Ulcer Image	
			


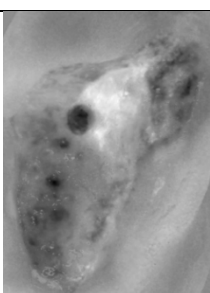

Ulcer No.: P42		Date Image was Taken: 24/02/2011 - OPD	
Colour Ulcer Image	Colour Ulcer Image	Colour Ulcer Image	
			


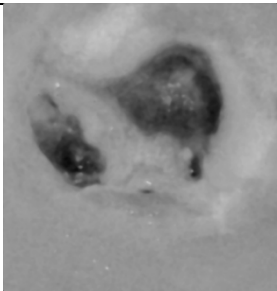

Ulcer No.: P43-1		Date Image was Taken: 03/05/2011 - OPD	
Colour Ulcer Image	Colour Ulcer Image	Colour Ulcer Image	
			

Ulcer No.: P43-2		Date Image was Taken: 03/05/2011 - OPD	
Colour Ulcer Image	Colour Ulcer Image	Colour Ulcer Image	
			

Ulcer No.: P44		Date Image was Taken: 03/05/2011 - OPD	
Colour Ulcer Image	Colour Ulcer Image	Colour Ulcer Image	
			

Ulcer No.: P45		Date Image was Taken: 03/05/2011 - OPD	
Colour Ulcer Image	Colour Ulcer Image	Colour Ulcer Image	
			

Ulcer No.: P47		Date Image was Taken: 04/05/2011 - OPD	
Colour Ulcer Image	Colour Ulcer Image	Colour Ulcer Image	
			

Ulcer No.: P48		Date Image was Taken: 04/05/2011 - OPD	
Colour Ulcer Image	Colour Ulcer Image	Colour Ulcer Image	
			

Ulcer No.: P50		Date Image was Taken: 04/05/2011 - OPD	
Colour Ulcer Image	Colour Ulcer Image	Colour Ulcer Image	
